THE INVESTIGATION OF FLUORINATED SOLVENTS FOR CARBON DIOXIDE ABSORPTION

ZIBUSISO LUBIMBI

[B.ENG, NUST, ZIMBABWE]

Submitted in fulfilment of the requirements for the degree Master of Science in Engineering (Chemical Engineering) in the College of Agriculture, Engineering and Science, University of KwaZulu-Natal, Durban.

Supervisors: Prof. Deresh Ramjugernath, Prof. Paramespri Naidoo and Dr. Wayne Nelson.

As the candidate's supervisor I agree to the submission of this thesis:

_____   _____
Prof. Deresh Ramjugernath   Prof. Paramespri Naidoo

_____
Dr. Wayne Nelson

DECLARATION

I, <u>Zibusiso Lubimbi</u>, student number: <u>215081031</u> declare that:

The research reported in this dissertation/thesis, except where otherwise indicated, is my original work.

(i) This dissertation/thesis has not been submitted for any degree or examination at any other university.

(ii) This dissertation/thesis does not contain other person's data, pictures, graphs or other information unless specifically acknowledged as being sourced from other persons.

(iii) This dissertation/thesis does not contain other person's writing unless specifically acknowledged as being sourced from other researchers. Where other written sources have been quoted, then:

   a) their words have been re-written, but the general information attributed to them has been referenced;

   b) Where their exact words have been used, their writing has been placed inside quotation marks and referenced.

(iv) Where I have reproduced a publication of which I am an author, co-author or editor, I have indicated in detail which part of the publication was written by myself alone and have fully referenced such publications.

Signed: _____   Date: _____

Acknowledgements

"Knowledge is in the end based on acknowledgement" **Ludwig Wittgenstein**.

This work was made possible through the encouragement, assistance and support of the following:

- ❖ My God, through whom all things are possible.

- ❖ My supervisors Dr. W. Nelson, Prof. P. Naidoo and Prof. D. Ramjugernath for their invaluable support and assistance throughout the duration of the project and for affording me the opportunity to call UKZN my alma mater.

- ❖ The Fluorochemical Expansion Initiative (FEI) and NRF for their financial assistance.

- ❖ The Thermodynamics Research Unit's laboratory staff and the Chemical Engineering Workshop technicians, with special mention given to Mr Ayanda Khanyile and Mr Sanjay Deeraj.

- ❖ My colleagues in the Chemical Engineering department, Mr E. Gande, Miss N. Moodley, Mr P. Bengesai, Mr P. Ndlovu, Mr F. Chikava and Mr S. Nkwanyana.

Last but not least, my Parents, Mr and Mrs Lubimbi, for the encouragement and unwavering support throughout all the years of my studies, of which I am eternally grateful.

Abstract

Research studies have shown that the solubility of carbon dioxide is higher in compounds that contain a fluorinated alkyl segment compared to their non-fluorinated counterparts. Despite this, published experimental data relating to the solubility of carbon dioxide in fluorinated compounds is still limited in literature, with the available data comprising of only fluorinated hydrocarbons (perfluorocarbons). Previous studies utilised the perfluorocarbons (PFCs) C_6F_{14}, C_6F_6, C_7F_8, C_7F_{14}, C_8F_{18}, $C_{10}F_{18}$ and heavier PFCs $C_{13}F_{22}$, $C_{14}F_{24}$ and $C_{17}F_{30}$. This study builds upon the investigation of fluorinated compounds as potential solvents for flue gas treatment. The research work involved generating a database of thermophysical properties of fluorinated chemicals and identifying the effects of chemical functional groups on the solubility of carbon dioxide in fluorinated chemicals. HPVLE measurements were performed at the temperatures (273.15, 293.15 and 313.15) K and pressures up to approximately 7.5 MPa. The binary systems of carbon dioxide with either perfluoroheptane, perfluorononane or 1,1,2,2-tetrafluoroethyl 2,2,3,3-tetrafluoropropyl ether were measured at three isotherms. The core measurements were conducted through the use of an apparatus which utilised the static analytic method and was fitted with an equilibrium cell with a volume of approximately18 cm^3. Sample withdrawal from within the cell was achieved via the Rapid Online Sampler Injector (ROLSI™). A second apparatus of the static synthetic type, with a variable volume cell, was used to affirm the data from the static analytic apparatus. The generated experimental data was regressed via the Peng-Robinson equation of state with the classical one-fluid mixing rule and/or the Peng–Robinson equation of state incorporating the Mathias-Copeman alpha function with the Wong-Sandler mixing rules and the Non-Random Two Liquid local composition model. The three novel binary systems were better correlated by the complex model, with relative deviations in both pressure and composition below 1.5%. The binary system consisting of the hydrofluoroether exhibited negative deviation from Raoult's law due to the combination of the ether group and the (C-F) bond, resulting in better carbon dioxide solubility relative to the perfluorocarbons used in this work.

Carbon dioxide solubility data for the hydrofluoroether system measured at 313.15 K was then compared to VLE data for the industrial solvent GENOSORB 1753 (mixture of polyethylene glycol dimethyl ethers), which was also measured at 313.15 K. The comparison indicated that the two solvents had near identical carbon dioxide dissolution capabilities in the (0 - 0.2) mole fraction

range, with the hydrofluoroether eventually outperforming the industrial solvent in the (0.2 – 1) range. Studies have shown that the GENOSORB 1753 solvent is on par with the reputable SELEXOL solvent with regard to carbon dioxide dissolution capabilities. Thus the exceptional proficiency of the hydrofluoroether in absorbing carbon dioxide was deemed competitive at an industrial level. However other factors such as the high vapour pressure of the fluorinated compounds still need to be rectified, possibly through the mixing of various homologs of the solvents. Furthermore, the selectivity of the hydrofluoroethers for other gases in a flue gas stream should also be studied in conjunction with a comprehensive process selection and design study to further assess their viability as absorption solvents.

Nomenclature

α	Cubic equation of state parameter
a_{ij}	Temperature dependence in the Aspen NTRL τ function/classical combining rule
A	Molar Helmholtz free energy (kJ.mol^{-1})
b	Equation of state co-volume parameter
b_{ij}	Temperature dependence in the Aspen NTRL τ function
$c_i (i = 1, 2, 3)$	Mathias-Copeman parameters
f	Fugacity (MPa)
g_{ij}	Adjustable parameter for the NRTL model (kJ.mol^{-1})
G	Molar Gibbs free energy (kJ.mol^{-1})
k	Coverage factor
k_{ij}	Binary interaction parameter
l_{ij}	Binary interaction parameter
n	Number of data point
P	Pressure (MPa)
R	Universal gas constant (J. mol^{-1}.k^{-1}
T	Temperature (K)
u_c	Combined standard uncertainty
U	Expanded uncertainty
v	Molar volume (m^3. mol^{-1})
x	liquid mole fraction
y	Vapour mole fraction
z	Liquid or vapour compositions

Greek Letters

α	Alpha function in the equation of state
α_{ij}	Non-randomness parameter in the NRTL model
φ	Fugacity coefficient
ε	Equation of state constant

γ	Activity coefficient
τ	NRTL energy parameter
σ	Standard deviation
ρ	Density (kg. m^3)
ω	Acentric factor

Table of Contents

List of Figures

List of Tables

Chapter 1

1 Introduction

The advent of fluorine chemistry and its progressive development ushered in a growing understanding of how the fluorine atom affects the reactivity, structure, and function of fluorine-containing molecules. This development, in turn, has sparked investigations into the properties and applications of perfluorocarbons (PFCs) and other fluorinated compounds (with various functional groups) in diverse fields such as engineering, biochemistry, biophysics, pharmacology and biotechnology. The term perfluorocarbon refers to chemicals which contain only carbon and fluorine atoms, as per the standard in fluorine chemistry (Banks et al., 1994).

As a direct result of the innovations in fluorine chemistry, the Fluorochemical Expansion Initiative (FEI), was launched in 2008 by the South African Government and seeks to establish fluorochemical industries locally. This project falls under the FEI initiative and the DST/NRF South African Research Chairs Initiative (SARChI) in Fluorine Process Engineering and separation technology, based in the Thermodynamics Research Unit (TRU) at the University of KwaZulu-Natal (UKZN). Thus, this work is also aligned with the ethos of generating a database for the thermophysical properties of fluorochemicals, which is useful in the design of separation processes and valuable for knowledge generation.

Various independent studies have demonstrated that compounds containing a fluorinated alkyl segment have a heightened affinity for the dissolution of light gases (Lazzaroni et al., 2005; Dias et al., 2006; Heintz et al., 2008). This is due to the high electronegativity of the fluorine atoms which results in the repulsion between the molecules of the liquid, causing formation of larger cavities within the intermolecular structure of the liquid (Gwinner et al., 2006). However, most data pertaining to the solubility of carbon dioxide in fluorinated compounds consists of binary mixtures of the gas with perfluorocarbons. The ability to dissolve large amounts of light gases is not only inherent to perfluorocarbons but also exists for partial or fully fluorinated chemical species, containing an electron donating functional group (Gui et al., 2011).

1.1 Dissolution of light gases

Experimental data asserting to the excellent solubility of light gases, particularly carbon dioxide and oxygen in perfluorocarbons has resulted in studies aimed at developing industrial, environmental and clinical applications. These applications include carbon dioxide capture from gaseous waste streams (Pennline et al., 2008), improvement of the solubility of hydrophilic substances in supercritical reaction or extraction media (Raveendran and Wallen, 2002) and the utilisation of PFCs in gas delivery therapeutics (Riess, 2001). The clinical applications, however, are mostly dependent on the inertness of the compounds, which results from the strong electrovalent liaisons formed through the complete substitution of all hydrogen atoms with fluorine. Thus perfluorocarbons are applicable.

1.1.1 Carbon dioxide capture through absorption

The Intergovernmental Panel on Climate Change (IPCC), in their fourth assessment, concluded that most of the increase in global temperatures since the mid -20th century was due to the increase in greenhouse gas emissions from the energy sector (Edenhofer and Sokona, 2011). Thus, there is a consensus on the need to develop reliable energy alternatives that can effectively replace fossil fuels (Dresselhaus and Thomas, 2001; Sims et al., 2003). However, studies indicate that the global energy market will continue to depend on fossil fuels for the next couple of decades (Shafiee and Topal, 2009). In order to mitigate the adverse effects of fossil fuels on the environment, various technologies aimed at reducing the amounts of anthropogenic greenhouse gas emissions are being developed. These technologies include fossil fuel switching, renewable energy, flue gas capture technologies, control of power consumption and nuclear power.

Technologies for flue gas capture are currently the most viable at an industrial scale. These technologies, however, consists of three main pathways which are post-combustion capture, pre-combustion capture, and oxy- combustion capture. Among the three, the post-combustion carbon capture pathway has the highest near-term potential, as it can be retrofitted to most existing power generation units (Figueroa et al., 2008). The separation technology that is most utilised in post-combustion applications at an industrial scale is absorption (Gwinner et al., 2006). Absorption can be employed via a physical or chemical route. Physical absorption is dependent on the solubility of the gaseous effluent within the extraction solvent. Thus its extraction mechanism is in line with

the work that was performed in this project. Consequentially, only processes utilising physical absorption are reviewed in this study.

The physical absorption processes currently most utilised at an industrial scale are the SELEXOL and RECTISOL processes, and these make use of the mixtures of Poly(ethylene glycol)dimethyl ether and refrigerated methanol, respectively (Kohl and Nielsen, 1997). These processes can only be effectively utilised in syngas treatment, where the gas stream is at high pressure, which varies between (4−5.5) MPa, depending on the type of gasifier used (Heintz et al., 2008). The RECTISOL technology can be classified as a cold gas clean-up technology since the entire syngas stream is cooled to temperatures in the range of (211 - 272) K prior to hydrogen sulphide and carbon dioxide removal (White et al., 2003). The cooling, however, results in a drastic reduction of thermal efficiency in the processes due to condensation of most of the water vapour present within the syngas, thus increasing the capital cost of the technology.

The major drawback of cold gas clean-up technologies has resulted in a pressing need for the development of what are termed warm gas clean-up technologies. Such technologies are being developed with the capability of operating at moderate temperatures of approximately 500 K, in order to produce a syngas stream that can be effectively utilised in downstream processes (e.g., Fisher−Tropsch) (Heintz et al., 2008). However, the work done herein pertaining to the solubility of carbon dioxide was conducted at mild temperatures which are in the working range of the SELEXOL process, which has a maximum working temperature of 448.15 K (Kohl and Nielsen, 1997).

1.2 Overview of the study

Aim

To analyse the solubility of carbon dioxide in three fluorinated chemicals, which are perfluoroheptane, perfluornonane and 1,1,2,2-tetrafluoroethyl-2,2,3,3-tetrafluoropropyl ether by way of high-pressure vapour-liquid equilibrium (HPVLE) measurements, for the purpose of proposing a potential solvent family for integrated gasification combined cycle (IGCC) waste gas treatment through the physical absorption route.

Objectives

- ❖ Measurement of two binary test systems comprising of carbon dioxide in conjunction with the liquids hexane and perfluorooctane at temperatures of 313.15 K and 293.15 K respectively. The purpose of the test system measurement was to allow the experimentalist to develop a sound technique before embarking on the core measurements.

- ❖ The measurement of three novel binary systems comprising of carbon dioxide in conjunction with the fluorinated liquids perfluoroheptane, perfluorononane and 1,1,2,2 – tetrafluoroethyl 2,2,3,3-tetrafluoropropyl ether, measured at the isotherms (273.15 K, 293.15 K and 313.15 K) for each binary pair.

- ❖ Modelling of all experimental data using Aspen Plus V8.4 through the use of suitable thermodynamic models.

- ❖ Benchmarking the carbon dioxide absorption capabilities of the fluorinated compounds against those of an industrial solvent.

In this dissertation, the introductory chapter is succeeded by a literature review of the physical absorption solvents which are used in industrial processes, including an analysis of the attributes which make the solvents ideal for gas cleaning applications. The mechanisms which facilitate the dissolution of carbon dioxide in the most prominent of these solvents are also discussed. The second chapter also includes an analysis of the physical properties of fluorinated compounds in conjunction with published HPVLE data of carbon dioxide in fluorinated compounds.

The third chapter focuses on a brief but concise review of HPVLE equipment based on the extensive reviews of most HPVLE equipment configurations developed over the years. The description of the static analytic and static synthetic apparatus which were used in this work is published in the fourth chapter, while the experimental procedures used are comprehensively outlined in the fifth chapter.

The sixth chapter deals with thermodynamic modelling, with emphasis on the explanation of the rationale behind the selection of each thermodynamic correlation/model. The procedure used to carry out the regression of VLE experimental data is also aptly outlined in this chapter.

The experimental results generated in this work (purity tests, calibration data, vapour pressure data and VLE data) are analysed and discussed in the seventh chapter, including the comparison of

carbon dioxide absorption capabilities of fluorinated compounds against those of an industrial solvent. The last chapter, which is the eighth chapter concludes the work in conjunction with the recommendations.

Chapter 2

2   Review of solvents for carbon dioxide physical absorption

2.1   Introduction

This chapter provides a review of solvents which are/may be used in the absorption of carbon dioxide through the physical absorption route. As was highlighted in the preceding chapter, some industrial applications have been developed which rely on the dissolution capabilities of carbon dioxide. However, the scope of the work carried out in this project focused primarily on reviewing the viability of three fluorinated compounds as potential solvents in carbon dioxide capture. Thus solvents used in the most prominent industrial physical absorption processes were also examined including the key characteristics necessary for the selection of an absorption solvent. Carbon capture processes were not discussed in this study, thus for concise information on the subject the reader is directed to the works of Bucklin and Schendel (1984), Olajire (2010) and Zaman and Lee (2013).

2.2   Characteristics of a suitable absorption solvent

The use of physical solvents in gas cleaning processes began to rise after the inception of the Fluor process in 1960. This technology utilised propylene carbonate as the absorption solvent in a relatively straightforward design scheme (Bucklin and Schendel, 1984). As a result, a number of processes have been developed, all using different solvents. However the search for superior solvents is still ongoing, but it is marred by the very nature of the screening process, which is expensive and time-consuming (Henni et al., 2005).

In order to validate the viability of a new solvent for carbon capture, the respective solvent should be benchmarked against already established solvents. Table 2-1 lists physical absorption processes, including the physical properties of the solvents used in each process. The RECTISOL process which uses methanol as the capture solvent was not included in the list by virtue of the liquids high vapour pressure at normal capture conditions, which makes its comparison with other processes difficult (Bucklin and Schendel, 1984). A number of studies have been conducted which focused on the comparison of various physical absorption processes, with the emphasis being on the entire process at large (Bucklin and Schendel, 1984; Doctor et al., 1993; Burr and Lyddon, 2008).

However, the study herein focused primarily on the characteristics of the solvents, particularly their carbon dioxide dissolution capability, thus the study of Zawacki et al. (1981) was used to stream-line the industrial solvents to be discussed, to avoid redundancy.

Table 2-1: Physical properties of industrial absorption solvents. Adapted from Bucklin and Schendel (1984).

PROPERTIES	PROCESS				
	SELEXOL	**Fluor**	**Purisol**	**Sepasolv**	**Estasolvan**
Solvent name	SELEXOL	Propylene carbonate	N-methyl -2-pyrrolidone	Sepalov	Tributyl phosphate
Licensor	Dow	Fluor	Lurgi	B.A.S.F	Uhde & IFP
Viscosity[c], Pa.s	0.006	0.003	0.002	-	0.002
Specific gravity	1030	1195	1027	-	973
Molecular weight	280	102	99	320	266
Vapour pressure[c] , mMPa	0.000097	0.0113	0.0533	0.000049	<0.001
Freezing point (K)	245.15	225.15	249.15	-	193.15
Boiling point, (K), 760 mm H$_g$	-	513.15	475.15	593.15	(453.15, 30 mm H$_g$)
Thermal conductivity (KW/mK)	0.0001	0.0002	0.0001	-	-
Maximum operating temperature (K)	448.15	338.15	-	448.15	-
Specific heat[c]	0.49	0.339	0.40	-	-
Water solubility[c]	∞	94 gm/l	∞	∞	65gm/l
Molar solubility of carbon dioxide (K) [a]	0.76[b]	1.56	1.24	-	-
Selectivity of $K_{C_2H_6}/K_{CO_2}$[a]	2[b]	3.34	2.55	-	-

[a] (Zawacki et al., 1981)

[b] Values for Dimethyl Ether of Tetraethylene glycol were used, which is a component of the SELEXOL solvent

[c] Temperature dependent parameters were determined at 298.15 K

For a solvent to be deemed an economically viable option for flue gas cleaning, it should meet a specific criterion which hinges on economic, performance and environmental factors. Brief descriptions of the criterion above and its efficacy on the design of separation processes are highlighted below:

Low viscosity – This property of the fluid should be low, (approximately 0.006 Pa.s) at the lower end of the operating temperature range in the capture process to be employed (Higman and van der Burgt, 2003). High viscosity would result in adverse effects on the equipment, particularly pumping systems through the reduction of flow rate, head pressure and brake horsepower, leading to an increase in operating costs.

Thermal stability- The solvent of choice should not thermally decompose at the specified capture conditions. This degradation would result in the formation of unrequired substances which could be hazardous when emitted into the atmosphere and most likely lead to an increase in operating costs due to the excessive loss of solvent.

Non-corrosive - This is a rule of thumb for any design process, such that the material of construction for all process equipment and piping should be compatible with the solvent to be used.

Vapour pressure –The vapour pressure of the solvent should be negligible at the flue gas capture conditions. This will then prevent the loss of large amounts of the solvent in the regeneration step.

Absorption Capability - For practicality, the solvent used in a carbon dioxide capture process should have an equilibrium capacity for acid gases which is substantially larger than that of water and a low capacity for the main constituents of the gas stream, which can be hydrocarbons. The high capacity for carbon dioxide by the solvent will allow the process to effectively use the least amount of solvent possible for circulation.

Global warming potential (GWP) - This is a measure which quantifies the ability of a molecule to affect the climate, and is evaluated through the use of the molecules lifetime in conjunction with its radiation absorption capabilities (Good et al., 1998). Thus absorption solvents should ideally have very low or negligible GWPs since some interaction of the solvent with the environment is bound to occur primarily during the regeneration step of the process.

The cost of solvent – This is also a rule of thumb for any design process since the operation of the process has to be economically feasible. The cost of the solvent thus should not be excessive, which is a principle that applies to the entire process at large.

2.3   Industrial solvent

The study conducted by Zawacki et al. (1981) was the most robust solvent screening study conducted thus far and resulted in the screening of more than a hundred solvents, which eventually led to the selection of N-formyl morphine (NFM) and dimethyl ether of tetraethylene glycol (DMETEG). Krupp Uhde GmbH later licensed the former in 1997, while the latter is one of the dimethyl ethers that constitute the SELEXOL solvent (Henni et al., 2005). Due to its unparalleled industrial success in gas cleaning applications involving physical absorption, particularly in sweetening flue gases from integrated gasification combined cycle (IGCC) processes, the SELEXOL solvent is aptly discussed in the section that follows.

SELEXOL solvent

Before the advent of the SELEXOL process, polyethylene glycol ethers were studied and noted to exhibit attributes which made the substances ideal candidates for gas sweetening applications (Kutsher and Smith, 1968). These substances, however, were noted to be affected by disadvantages such as high volatility which would inevitably result in high solvent loss during operation. Heavier homologues of the substance were also not viable substitutes regardless of their low volatility, due to the high viscosities which are inherent in the compounds (Ameen and Furbush, 1971).

The SELEXOL solvent was thus developed through the mixing of dimethyl ethers of polyethylene glycols $[CH_3(CH_2CH_2O)_nCH_3]$, where n is in the range $(3-9)$. The exact amounts of each homologue are proprietary information. However, the mixing was performed in such a manner that the vapour pressure and viscosity of the resulting mixture did not exceed 0.0013 mMPa and 0.0088 Pa.s respectively at temperatures up to 316.15 K (Ameen and Furbush, 1971). In order to further lower the viscosity of the mixture to a range between $(0.001-0.005)$ Pa.s, one weight percent of carbon dioxide is initially dissolved into the liquid before its use in the process.

The carbon dioxide solvation mechanism of the SELEXOL solvent makes use of the ether functional group. The presence of these groups throughout the molecular structure of the complex

liquid results in sites where Lewis acid−Lewis base reactions can occur, which enhance the solubility of the gas within the liquid (Hanson, 2001; Miller et al., 2010). Dimethyl ethers have also been noted to have near negligible GWPs (Good et al., 1998), signifying that the SELEXOL solvent does not negatively affect the global climate. The high solubility of carbon dioxide in the dimethyl ethers can also result in some adverse effects, as was shown in the work of Zawacki et al. (1981). The aforementioned study highlighted that as the molar solubility of carbon dioxide in the dimethyl ethers increased (which is shown by the low K_{CO2} values), the selectivity of removing the gas from hydrocarbons was reduced, as emphasised by the low values for the ratio of $(K_{C_2H_6}/K_{CO_2})$ in Table 2-2.

Table 2-2: Selectivity of dimethyl ethers. Adapted from Zawacki et al. (1981).

Solvents	K_{CO_2}	K_{H_2S}/K_{CO_2}	$K_{C_2H_6}/K_{CO_2}$	K_{CH_4}/K_{CO_2}	K_{CO}	K_{H_2}
Dimethyl ether of diethylene gycol	**0.87**	0.21	**1.41**	7.33	21.6	42
Dimethyl ether of ethylene gylcol	**0.92**	0.28	**1.14**	6.95	12.2	31.8
Dimethyl ether of tetraethylene glycol	**0.76**	0.18	**2**	8.65	25	50

The solvent also has high miscibility with water, which impedes the absorption of carbon dioxide in an IGCC capture process (Miller et al., 2010). For the sake of gas cleaning process efficiency, new physical solvents are constantly screened and studied such as fluorinated compounds and ionic liquids in a bid to develop better performing solvents (Pennline et al., 2008).

2.4   Fluorinated solvents

The once-unusual behaviour of fluorinated compounds has become seemingly easier to comprehend due to the advancement of experimental and theoretical organic fluorine chemistry in the past two decades (Banks et al., 1994). This, in turn, has sparked numerous commercial applications for the substances, some of which are currently being thoroughly investigated, such as their potential use in gas cleaning applications. The following sections analyse the compound's

gas dissolution capabilities, physical properties and published VLE binary data with carbon dioxide.

Solubility of carbon dioxide

The addition of fluorine atoms in the molecular structure of a compound has been shown to result in the reduction of its polarisability/solubility parameter value (Hoefling et al., 1992). This reduction enhances the solubility of carbon dioxide in fluorinated compounds since the gas also has a relatively low solubility parameter value, which is similar to the values of most fluorinated compounds. The correlation developed by Hansen (1967) highlighted the need for a small difference between the solubility parameters of the solute and solvent in order for the solute to be highly soluble in the solvent. This assessment was based on the fact that solubility parameters are a function of the cohesive energy density of the molecules of the compound, which in turn is a direct indication of the degree of van der Waals forces holding the molecules of the compound together (Burke, 1984). This then means that if two compounds have similar solubility parameter values/ cohesive energy densities, then the molecules of one compound will be able to separate molecules of the other and vice versa, thus allowing solubilisation of the solute to occur. The cohesive energy densities between the molecules in PFCs are approximately half those of their hydrocarbon counterparts (Barton, 1983). The aforementioned comparison is shown in Table 2-3.

The actual mechanism that occurs in the solubilisation of a solute was postulated by Gwinner et al. (2006). This study asserted that two thermodynamic steps characterise the absorption of a solute in a solvent. The initial step in the sequence involves the formation of cavities within the solvent through shearing of solvent-solvent interactions, which is energy dependent, thus rendering the step endothermic. This step, however, is made easier in fluorinated compounds due to the high ionisation potential and low polarisability of the fluorine atom, which results in relatively weak intermolecular forces within the compound (Ducheyne et al., 2015), thus resulting in lower solubility parameters, as stated above. The final step in the sequence involves the insertion of the solute molecule within the cavities of the solvent, which is an exothermic process that is dependent on the solute–solvent interactions that are created (Gwinner et al., 2006).

Physical properties

Besides the ability of imbuing compounds with greater gas solvation capabilities, fluorination also enhances physical properties of the respective compounds. Numerous studies attest to the effect of

fluorination on the physical properties of compounds, and this has mostly been achieved through the comparison of PFCs with their hydrocarbon counterparts (Maciejewski, 1990; Banks et al., 1994). Herein, only physical properties which affect the compounds ability to effectively function as an absorption solvent are discussed. Table 2-3 displays the physical properties of some fluorinated hydrocarbons. The list is non-exhaustive and serves to highlight the variation of physical properties when a hydrocarbon is fluorinated and the effect of chain length on the respective properties.

Table 2-3: Physical properties of some perfluorocarbons. Adapted from Banks et al. (1994).

Property	C_6H_{14} [b]	C_6F_{14}	C_7F_{14}	$C_{10}F_{18}$
Molecular weight (g/mol)	86.2	338	400	512
Density (kg/l)[a]	0.655	1.682	1.828	1.972
Boiling point (K) at 1 atm	342.15	330.15	375.15	433.15
Pour point (K)	-	183.15	203.15	203.15
Viscosity (dynamic) (Pa.s)[a]	0.0003	0.0007	0.002	0.006
Surface tension (mN m $^{-1}$)	17.9	11.1	16.6	18.5
Vapor pressure (MPa)[a]	0.0204[c]	0.0294	0.0048	0.0002
Specific heat (kJ kg $^{-1}$ K $^{-1}$)	-	1.09	0.903	1.09
Critical temperature (K)	234.45	177.9	241.5	313.4
Critical pressure (MPa)	3.020	1.834	1.881	1.660
Cohesive density (ΔH_{vap}) kJ cm^{-3}	0.22[d]	0.14[d]	-	-

[a] Temperature dependent parameters were determined at 298.15 K
[b] (Maciejewski, 1990)
[c] (Carruth and Kobayashi, 1973)
[d] (Robb, 2012)

The vapour pressure of fluorinated compounds is an important parameter as it governs the tendency of the compound to disseminate into the environment (Stock et al., 2004). The vapour pressures of PFCs are similar to those of their analogous hydrocarbons because both substances have no permanent molecular dipole moment. Thus the molecular attractive forces which contribute to the pressures are the Van der Waal forces. For both hydrocarbons and PFCs, the vapour pressures decreases with an increase in molecular weight, viz., carbon chain length, which

is an expected trend. However, the vapour pressures of PFCs displayed in Table 2-3 are substantially higher than those of industrial solvents such as the SELEXOL solvent, which has a vapour pressure of 0.00009 mMPa at 298.15 K. This then means that there is a higher chance of solvent loss during the regeneration step if pure fluorinated compounds are used in gas cleaning applications. This could have adverse effects on the environment if the fluorinated compounds in question are PFCs since these have been noted to have long life times and also absorb relatively larger amounts of longwave radiation (Zhang et al., 2011), which translates to large GWP values. However, hydrofluoroethers, on the other hand, have significantly lower GWP values due to the ether functional group, which has been observed to reduce the molecular lifetime of compounds (Lazarou and Papagiannakopoulos, 1999).

Fluorinated compounds, particularly the compounds which have undergone complete substitution have been noted to exhibit high thermal and chemical stability. These properties are a function of the carbon-fluorine single bond, which is the strongest bond ever observed in organic chemistry thus far (Stock et al., 2004). Another unique feature of fluorinated compounds which has been postulated to enhance its thermal and chemical stability is their peculiar molecular geometry. The structure of fluorinated compounds changes as the carbon chain increases from a zigzag structure to one which is partly zigzag and helical when the chain length exceeds ten carbon atoms (Wang and Ober, 1999). This shift in the structure is due to the fact that the fluorine atom is larger than the hydrogen atom, thus saturated fluorination results in a compound with a rigid structure (Stock et al., 2004). In order to avoid steric hindrance, the structure of the compounds thus changes with size.
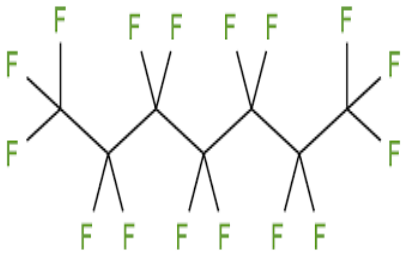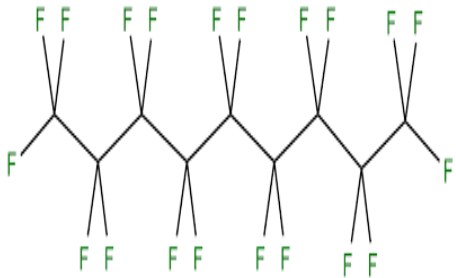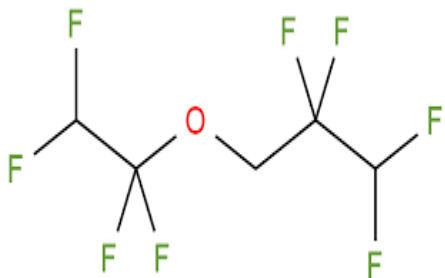
Solvents which are used in gas cleaning applications should ideally be insoluble in water, which in turn would allow the solvents to absorb large amounts of the desired waste gas constituents. Fully fluorinated compounds are inherently insoluble in most liquids including water, with the exception of low chain hydrocarbons (Simons, 2012). The viscosity of the solvent is also an important characteristic as has been mentioned in the preceding section. Since fluorination results in rigid molecular structures, it stands to reason that the viscosity of a fluorinated compound will be greater than that of its hydrocarbon counterpart. Though the viscosities of low chain fluorinated compounds, particularly PFCs are lower than those of industrial absorption solvents, higher chain

PFCs have been shown to have viscosities which are substantially higher than the SELEXOL solvent (Heintz et al., 2008).

2.5   Physical properties of the chemicals of interest

As was stated in the preceding chapter, the study focused on the use of three chemicals, two perfluorocarbons, and one partially fluorinated ether. The choice of chemicals was dependent mostly on their availability, but the focal point was in utilising fluorinated compounds with different functional groups since it has been postulated that the functional group can act to enhance or impede the solubilisation of carbon dioxide (Gui et al., 2011). The chemicals that were eventually studied were perfluoroheptane, perfluorononane, and 1,1,2,2-tetrafluoroethyl 2,2,3,3-tetrafluoropropyl ether. VLE data were measured at three isotherms for all the binary pairs at the temperatures (273.15, 293.15, 313.15) K, with maximum pressures of approximately 7.5 MPa. Table 2-4 highlights the physical properties of the chemicals of interest.

Table 2-4: Physical properties of the studied chemicals.

Molecular formula	C_7F_{16}	C_9F_{20}	$C_5H_4F_8O$
Main molecular species	Perfluoroheptane	Perfluorononane	1,1,2,2-Tetrafluoroethyl 2,2,3,3-tetrafluoropropyl ether
Structure			
Molecular weight (kg k mol^{-1})[b]	388.04	488.06	232.07
Density (kg m^{-3})[a]	1731.3	1799.9	1538
Boiling point (k) at 1 atm[b]	353.15 - 358.15	398.15 - 399.15	366.35
Viscosity (dynamic) (pa s)[b]	0.00093	0.0017	0.0011
Surface tension (n m^{-1})[b]	9.15	18.1	-
Vapour pressure (mMPa)[b]	10.4	2.596	5.643[a]
Heat capacity (j/kmol-k)[b]	418497.3	478653.7	292850.8
Critical temperature (k)[b]	474.85	523.97	510.07
Critical pressure (MPa)[b]	0.162	0.156	0.258
Thermal conductivity (wm^{-1} k^{-1})[b]	0.063	0.01	0.059
Refractive index[a]	1.261	1.274	1.290

[a] Exp data   [b] Nist data

Temperature dependent parameters were determined at 298.15 K, except the experimental data, which was measured at 293.15 K.

A preliminary comparison of the chemicals of interest against the SELEXOL solvent reveals that the vapour pressures of the former are substantially larger than those of the latter. This would imply a relatively large possibility of incurring solvent loss during the regeneration step if the fluorinated solvents in question were to be used in an absorption process. However, this disadvantage can be overcome through the formulation of mixtures using various homologues of the fluorinated compounds, which in turn would result in a mixture with lower vapour pressure (Heintz, 2012). The viscosities of the fluorinated compounds are ideal, all being substantially below that of the SELEXOL solvent as can be seen in the data tabulated in Tables 2-1 and 2-4. Other attributes of the chemicals of interest which make them potential flue gas absorption solvents were discussed in the preceding sections of this chapter. A concise explanation of the mechanisms at work is discussed in Chapter 7.

2.6   Published VLE data for carbon dioxide + fluorinated compounds

The data pertaining to carbon dioxide solubility in fluorinated compounds which are currently available in the open literature focus only on fully fluorinated hydrocarbons. Thus the mechanism of absorption utilised is similar throughout the different studies since the only difference between the studied PFCs is chain length and structural geometry. Figure 2-1 displays a P-x chart which features binary data for carbon dioxide with the following PFCs perfluoro-hexane (C_6F_{14}), perfluoro-benzene (C_6F_6), perfluoro-toluene (C_7F_8), perfluoro-methylcyclohexane (C_7F_{14}), perfluoro-octane (C_8F_{18}) and perfluorodecalin ($C_{10}F_{18}$). All the data in Figure 2-1 was measured using the synthetic technique at 313.15 K, thus a direct comparison could be undertaken.
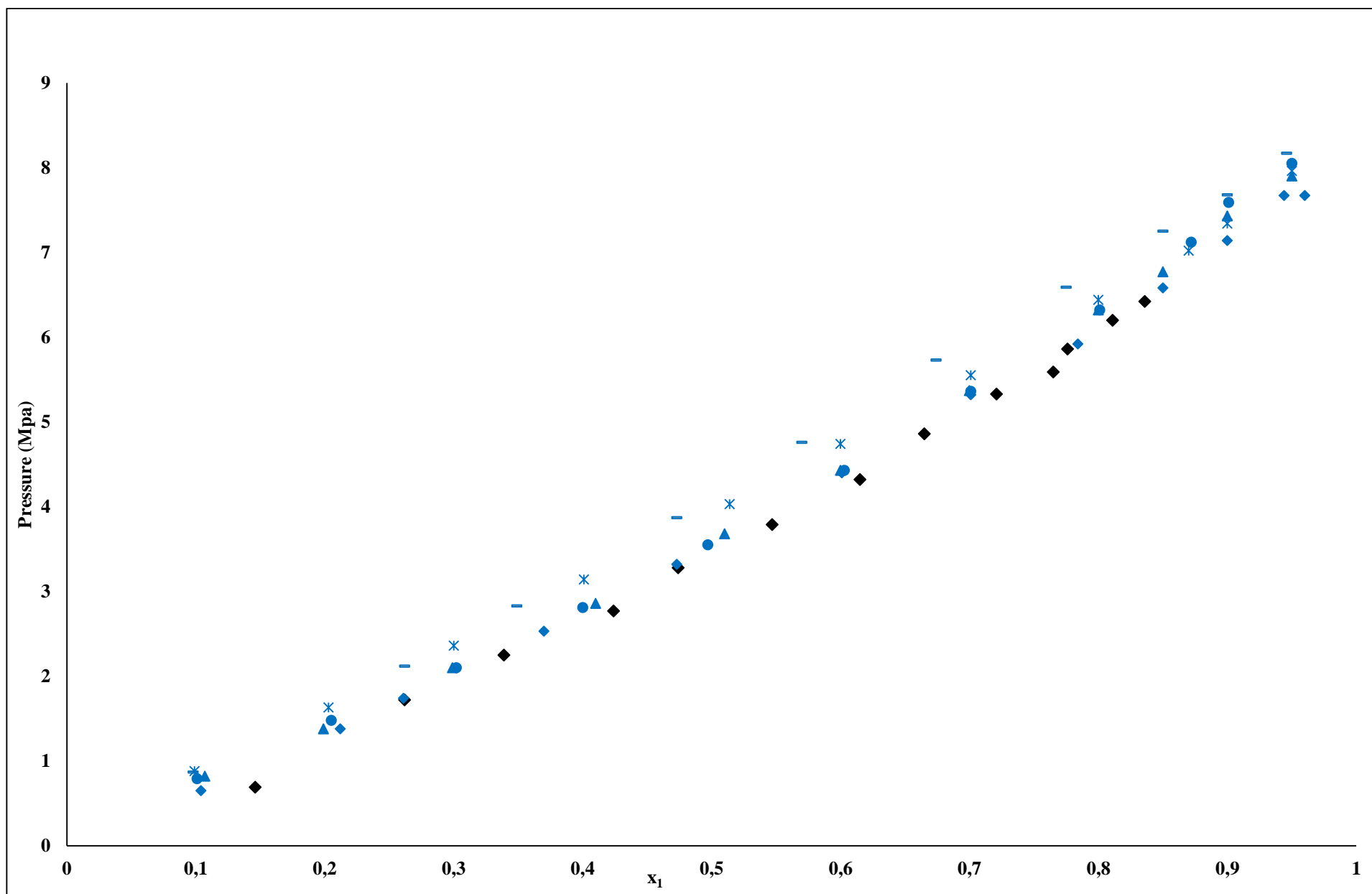
Figure 2-1: P-x plots for CO_2 (1) + fluoro-compound (2) systems at 313.15 K. **(a)** Lazzaroni et al. (2005):(◆) C_6F_{14}, **(b)** Dias et al. (2006): (◆) C_8F_{18}, (▲) C_6F_6, (●) C_7F_8, (∗) C_7F_{14} and (—) $C_{10}F_{18}$.

From the data displayed in Figure 2-1, it is evident that the structure of PFCs has an effect on their carbon dioxide solubilisation capabilities. Straight chain and aromatic PFCs are noted to absorb similar amounts of carbon dioxide at 313.15 K, while cyclic PFCs displayed the least capability for dissolving the gas. The interaction of carbon dioxide with the PFCs is noted to result in a slight positive deviation from Raoult's law, as highlighted by the near linear geometry of the various P-x plots in Figure 2-1. The carbon dioxide + perfluorohexane binary system which was measured by Lazzaroni et al. (2005) was modelled using the Patel–Teja equation of state in conjunction with Mathias–Klotz–Prausnitz mixing rules, whilst the data measured by Dias et al. (2006) was described using the soft statistical associating fluid theory equation of state.

Chapter 3

3   Equipment review

High-pressure vapour-liquid equilibrium (HPVLE) measurement is a highly developed field, dating back as far as the 19th century (Cagniard de La Tour, 1822). Since inception, the study has been marked by the development of numerous equipment configurations and experimental techniques. These have been further enhanced over the years, in a bid to make the inherently difficult process less cumbersome and more efficient. This development has, in turn, sparked an increase in publications relating to high-pressure phase equilibria, particularly in the last 30 years, for applications relating to carbon dioxide capture, hydrate formation, supercritical fluids, and polymer forming processes (Dohrn et al., 2012).

The two main classes of experimental techniques which are employed in HPVLE measurements can be categorised based on the manner in which the composition in each phase at equilibrium is determined and also the mechanism used to hasten the stasis. The latter can be achieved either through the internal agitation of the cell components (static) or the circulation of one of the phases (dynamic). However, the classification based on the agitation mechanism is not further explored as it has no clear reference to characteristic error sources (Dohrn et al., 2012). Therefore the composition of phases in equilibrium can be determined in one of two ways which are through the synthesis of a mixture of known compositions by either weighing the components prior to charging the cell or the loading of predetermined volumes of each component. The second pathway relies on the analyses of samples from each phase when equilibrium has been reached. This analyses can be achieved through the withdrawal of samples which can be thereafter analysed by gas chromatography (GC) or by use of gravimetric or spectroscopic methods. The variations in these two main pathways are depicted in Figure 3-1.
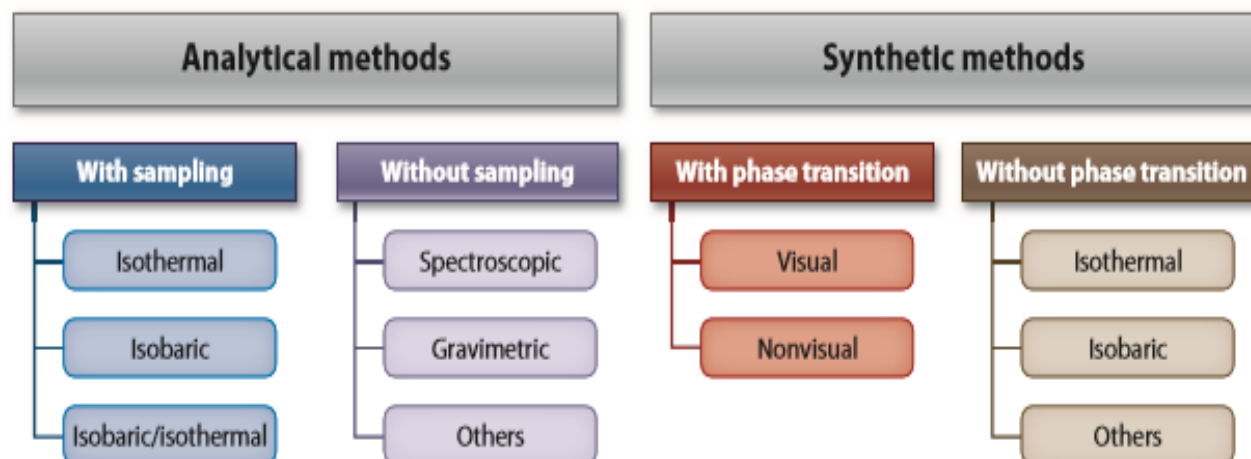
Figure 3-1: Classification of experimental techniques for high-pressure phase equilibrium measurements**.** Adapted from Dohrn et al. (2012)**.**

Extensive information has been published by various authors reviewing HPVLE experimental techniques, spanning over a hundred years. Some authors compiled information for a specific period, the earliest being Knapp (1982), who reviewed techniques from (1900-1980), followed by Fornari et al. (1990) who covered the (1978-1987) period. Dohrn and Brunner (1995) covered (1988-1993), whilst Christov and Dohrn (2002) pulled the curtain over the 20th century by reviewing the techniques used in the (1994-1999) period. The techniques used in the 21st century thus far have been examined for only the first eight years of the new millennium by Dohrn et al. (2012) from (2000-2004) and lastly Fonseca et al. (2011) for the (2005-2008) period. In light of the information which has been compiled over the years by various authors, including members of the Thermodynamics Research Unit, this chapter, therefore, reviews the operation of the isothermal analytical method which uses sampling and the synthetic visual method with phase transition as these were employed in this particular study. This was done in order to avoid any redundancy in the work. The reader is therefore directed to the works mentioned above for an aptly discussed analysis of most if not all VLE equipment configurations.

3.1 Analytic-Isothermal methods with sampling

As the name implies, this technique operates by utilising a sampling mechanism to withdraw samples from the phases present after equilibrium has been reached. Prior to sampling, the mixture is allowed to reach isothermal conditions while the other properties such as pressure and composition will naturally vary depending on the temperature. This technique can either be dynamic or static depending on the agitation mechanism employed as highlighted above. Equipment which uses this method of operation function based on three main stages, which are:

❖ Loading of the equilibrium cell

❖ Facilitation of the cell contents to equilibrate

❖ Sampling of each phase after equilibrium has been attained

The most crucial stage is the sampling. If this is not done appropriately, a pressure drop might occur within the cell, which will, in turn, alter the equilibrium conditions. In order to avoid this various sampling mechanisms have been developed, which ensure minimal disturbance to the cell contents during sampling, such as capillaries (Yu et al., 2006) and high precision sampling equipment such as the Rapid Online Sampler Injector (ROLSI $^{\text{TM}}$) (Guilbot et al., 2000). Prior to the advent of sampling equipment that could sample minute amounts, large equilibrium cells were mostly used to avoid any pressure drop. A static version of this technique, with a $18\,\text{cm}^3$ equilibrium cell was utilised in this study because of its ability to provide a complete characterisation of the phase behaviour of a vapour liquid system (Williams-Wynn, 2016), and also due to the smaller amounts of chemicals, the apparatus utilises. A non-exhaustive list of static analytical apparatus which have been reported in the open literature in the last decade is tabulated in Table 3-1. The list also includes a synopsis on the equipment description of these relatively modern apparatus. While the most recent novel design presented is dated 2011, to the best of the author's knowledge, equipment presented in the published literature since then have been variations or modifications of the experimental designs presented in the table.

Table 3-1: A summary of modern static analytic apparatus.

Author	Equipment description
(Naidoo et al., 2008)	The equipment of Naidoo et al. made use of a variable volume cell which had an internal volume of approximately 200 cm^3 and was fitted with a piston assembly. The attainment of equilibrium was facilitated by use of a composite impeller which contained a secondary impeller which could be independently activated. Sampling of the phases was achieved by using a 6-port 2-position GC sampling valve The equipment was designed to operate in the temperature range of (250 – 393) K and maximum pressures of 12 MPa.
(Houssin-Agbomson et al., 2010)	This apparatus was designed for the measurement of potentially explosive binary mixtures at cryogenic temperatures. The equipment was fitted with a 12 cm^3 Hastelloy equilibrium cell which could withstand pressures of up to 300 MPa. The cell was immersed in a cryostat which was partially filled with liquid nitrogen to maintain the low temperatures. Sample analyses was achieved via the use of a pneumatic ROLSI^{TM}.
(Tochigi et al., 2010)	This static analytical apparatus was employed in the measurement of HPVLE for the binary mixtures of carbon dioxide + n-octane, methanol, ethanol, and perfluorohexane. The equipment was designed to operate in the temperature range of (295 – 323) K and maximum pressures of 15 MPa. The equilibrium mixture was housed in a 500 cm^3 cell which was fitted with a Pyrex glass bulls – eye window. Sampling of the vapour and liquid phases was achieved via the use of a sample valve and an injector valve respectively.
(Narasigadu, 2011)	The design of this apparatus was instigated by the need to reduce the volume of chemicals HPVLE apparatus used in the generation of phase equilibria data. As a result an apparatus with an equilibrium cell volume of approximately 18 cm^3 was designed. The sampling mechanism which was employed made use of a rapid online sampler injector (ROLSI^{TM}) which was capable of sampling as minute as 1μl. Another novel feature in the apparatus was the volume compensation rod. This rod was connected via the bottom flange and thus acted to negate the displacement caused by the ROLSI^{TM} capillary by moving in the same direction as the capillary, within the binary mixture.

3.2 Synthetic-visual method with phase transition

The equipment used for this technique are usually relatively simple when compared to those which utilise the static analytical technique. This is primarily due to the lack of any sampling mechanisms in the apparatus. The use of this apparatus is not only restricted to VLE measurement but can be effectively utilised in multi phase equilibria (Calderone et al., 2007), solid-liquid equilibria (Dohrn et al., 2007), critical curves of mixtures (Martin et al., 2007), cloud point determination (Akutsu et al., 2007) and gas hydrate formation (Beltrán and Servio, 2008). The general operating procedure requires the loading of known amounts of the necessary components into an equilibrium cell, followed by pressurisation of the contents until the bubble pressure is reached. If the method is visual, then the cell will either be fabricated from a transparent material such as sapphire crystal, or from a metal with transparent viewing ports. The phase transition can then be determined through observing the equilibrium mixture until the disappearance of the last bubble within the mixture, signifying the transition to a single phase. The bubble point can also be determined through the analyses of the discontinuities in the isothermal pressure–volume relationship (Williams-Wynn, 2016). This method is typically used to measure P-x data, but P-xy data can also be measured, but this would require the use of thermodynamic correlations such as the Gibb – Duhem equation, in order to determine the phase compositions (Van Ness, 2015). The visual static synthetic method was used in this work as a means of validating the data from the static analytic apparatus and as such only a few P-x points were to be measured. Table 3-2 highlights a non-exhaustive list of relatively modern visual static synthetic apparatus with different designs, including a brief synopsis of the respective apparatus. For more information regarding the various visual static synthetic apparatus found in the open literature, the reader is directed to the works of Fonseca et al. (2011) and Dohrn et al. (2012).

.

Table 3-2: A summary of visual static synthetic apparatus.

Author	Equipment description
(Dias et al., 2006)	The experimental setup used by Dias et al. to measure HPVLE data for carbon dioxide and PFC mixtures used a 30 cm^3 variable volume cell in the form of a horizontal, hollow stainless steel cylinder which was fitted with a movable piston at one end and the other sealed with a sapphire window. The equipment was capable of operating in the temperature range of (273 - 507) K. A second sapphire window was installed on the wall of the steel cylinder to illuminate the cell contents. The contents of the cell were agitated by a magnetic stirrer and concurrently pressurised using the piston until the vapour phase completely disappeared. The bubble point pressure was measured when one small bubble was observed right before the disappearance of the vapour phase.
(Gil et al., 2008)	The rationale behind the work of Gil et al. was based on the need for phase equilibria data in the critical region, which was scarce in the open literature (Soo et al., 2010). This then led to the commissioning of an apparatus for the measurement of critical temperature and pressure of pure compounds and mixtures. The equipment utilised a flow apparatus. The maximum temperature and pressure constraints of the apparatus were 700 K and 20 MPa. The detection of the critical properties was achieved through critical opalescence. The equipment made use of a sapphire cell with an internal volume of 4 cm^3, which was housed between two titanium flanges. The cell was loaded via two thermostatic chromatography syringe pumps, which provided a flow of constant composition.
(Lay, 2009)	This equipment made use of a 130 cm^3 high pressure variable volume cell, which was fitted with viewing ports. The apparatus was designed to operate at a maximum pressure of 70 MPa and at temperatures not exceeding 473.15 K. The cell was pressured using a piston which was coupled with a displacement pump. The mixture in the cell was agitated by a magnetic mixer. The cell contents were pressurised until they completely liquefied, then the pressure was subsequently decreased until a bubble was observed, which signified the bubble pressure.
(Liu and Tomasko, 2007)	This work was focused on the study of the nature of carbon dioxide–polymer systems and utilised a visual static apparatus to measure the induced polymer swelling. The apparatus was designed to operate at a maximum pressure of 35 MPa and at temperatures not exceeding 523.15 K. The binary mixture was introduced into the cell in the form of a polymer melt drop which was saturated with carbon dioxide. The contents of the cell were then recorded through the use of two sapphire windows via a camera to determine the equilibrium interfacial tension.

The review carried out by Dohrn et al. (2012), attests to the decline in the use of the analytic method in favour of synthetic type apparatus. This is arguably due to the challenges posed by sample analyses and the intensive labour inherent in the use of the analytic apparatus. However since the measurement of accurate phase equilibria data is dependent on the experimentalist as much as the equipment, the Thermodynamics Research Unit still uses mostly static analytic apparatus, due to the high-level experience within the group.

Chapter 4

4 Experimental apparatus

4.1 Static analytic apparatus

This study utilised a static analytic apparatus that was designed by the TRU at UKZN and thereafter commissioned by Dr Caleb Narasigadu (Narasigadu, 2011) as part of his doctoral studies. The development of this apparatus was instigated as a means of reducing the high costs that were incurred in the use of large quantities of high purity and speciality chemicals, which are a necessity for some vapour liquid equilibrium measurements. In response to this drawback, the design featured a low volume sapphire equilibrium cell. Since its development in 2011, the apparatus has been used in the works of Tshibangu et al. (2014), Williams-Wynn et al. (2016) and Gande (2016).
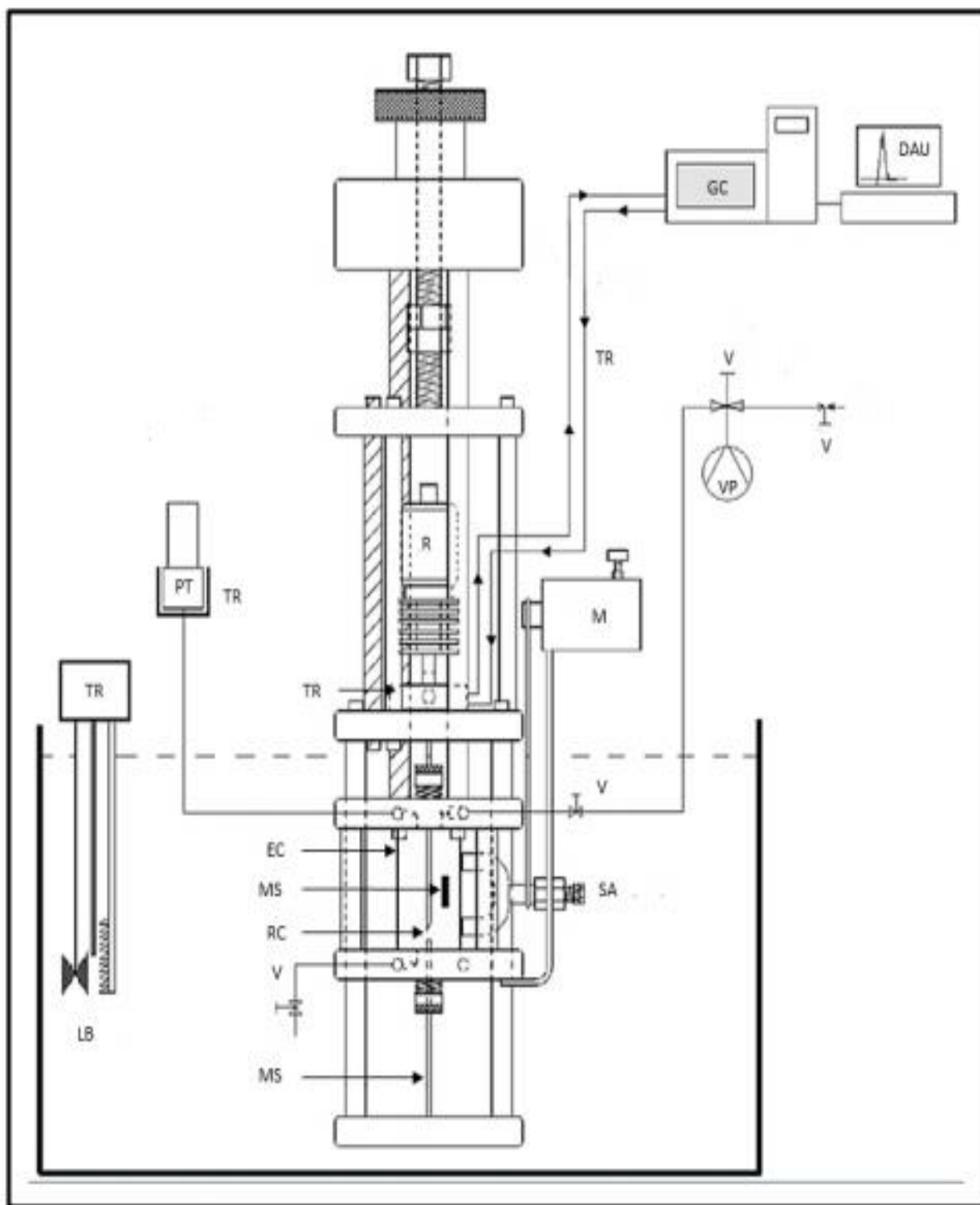
Figure 4-1: Schematic of the static analytic high-pressure VLE apparatus of Narasigadu. **DAU:** data acquisition unit, **EC:** equilibrium cell, **GC:** gas chromatograph, **LB:** Liquid bath, **M:** Motor, **MS:** magnetic stirrer, **PT:** pressure transducer, **R:** ROLSI™, **RC:** ROLSI™ capillary, **SA:** stirring assembly, **TR:** thermal regulator, **V:** valve, **VP:** Vacuum pump. Adapted from the work of Narasigadu (2011).

4.1.1 Equilibrium cell and housing

The unique feature of the high-pressure vapour liquid equilibrium apparatus that was commissioned by Narasigadu was the relatively low volume of the equilibrium cell. The new design introduced a low volume cell which was manufactured by (Rayotek Scientific Inc), fashioned from sapphire glass into a cylindrical tube with the following dimensions: (OD = 35.6 mm, ID = 17.8 mm and L = 70 mm) and an effective internal volume of approximately 18 cm^3 (excluding all dead and displaced volumes). The cell was constructed from sapphire crystal due to its desirable physical and chemical attributes such as high tensile strength, chemical resistivity and visual transparency, thus making it the most suitable material of construction for the equilibrium cell.

The housing of the equilibrium cell was fashioned from stainless steel (SS) 316 due to its high tensile and yield strength and the metals ability to retain said properties for long periods of time under extreme high or low temperatures (Sinnott, 2005). The sapphire cell was sealed between two stainless steel flanges, each having a thickness of 15 mm and a diameter of 110 mm.

The integrity of the housing structure was maintained by the use of three evenly distributed SS 316 spacer rods, which are 10 mm in diameter. Each flange contained a recess which was fitted with O-rings (ID = 18.72 mm), thus allowing the two flanges to act as a compression base for the cell, hence providing a tight seal. Another set of O-rings were installed around the outer diameter of the cell, these, however, did not facilitate any sealing, their sole purpose was to hold the cell in place within each recess. The type of O-ring used was dependent on the compatibility of the polymer with the chemicals in each system. Thus, O-rings manufactured from Viton, Nitrile, FFKM perfluoroelastomer (Kalrez) and polyurethane were used in this work. The latter was eventually noted to outperform the other materials as it withstood degradation from the chemicals used in the study.

The metal flanges also served as the only access points to the equilibrium cell, thus charging and discharging of the cell were performed via tubing and fittings connected to the flanges. Temperature and pressure measuring devices were also installed into the flanges via internal ports. The top flange had three wells drilled in its sides for the purposes of charging and venting the cell, pressure measurement through a line connected to a transducer and temperature measurement through the use of a thermocouple probe.

The connections necessary for the charging/venting line included a 1/8 inch NPT thread that was machined onto the 10.2 mm well on the flange which was then connected to a 1/8 inch SS 316 ball valve through a short SS 316 tubing with a corresponding outer diameter. The 10.2 mm well was machined in such a manner that its diameter abruptly decreased to 3 mm after a depth of 6.3 mm was reached, which is the standard length of the tapered threads.

The connection that facilitated the pressure measurement within the cell had a similar configuration to the charging line, with the exception of the ball valve and the outer diameter of the SS 316 tubing. This connection utilised a 1/16 inch tubing from the transducer and was soldered onto a 1/8 inch short pipe with a nut that was compatible with the NPT installed on the flange. The silver solder used was composed of tin (Sn) and silver (Ag), with the former component constituting over fifty percent in the alloy.

In the original design of the equipment, Narasigadu (2011) estimated the dead volume in the transducer connection to be 0.9 cm^3, thus Williams-Wynn (2016) reduced this volume through the use of a PTFE filler plug that was inserted into the gap of the 1/4 inch transducer nut. The third well on the side of the top flange was machined to house a temperature probe, which was one of two probes required to measure the temperature within the cell. This well also had a diameter of 6 mm, with a depth of 30 mm whilst maintaining a uniform internal diameter.

Another important function of the top flange was to provide support for the differential screw. This mechanism allowed movement of the ROLSI$^{\text{TM}}$ capillary within the cell, thus facilitating sample withdrawal in both the liquid and the vapour phases. The screw was manually actuated, and as the capillary moved within the cell, a solid SS 304 rod which was located in the bottom flange moved in the same direction as the capillary. This rod had a diameter that was equal to that of the capillary (3 mm), and thus negated any displacement within the cell that could have been caused by the capillary during its movement. The initial design of the equipment featured a 3.2 mm SS 316 rod, which was replaced in this work, with a (3 mm) SS 304 rod as the former failed to negate volume change within the cell effectively.

The lower flange had two wells machined on its sides, one for the discharge line and the other for housing the second temperature probe. The discharge line configuration and components perfectly mirror that of the charging line up-to-the ball valve. In the discharge line, the valve is preceded by

a 1/8 inch pipe that is open to the atmosphere for the purposes of discharging and consequently charging but only for the liquid components.

The points of entry of the capillary in the top flange and the displacement compensation rod in the bottom flange required a leak-tight sealing mechanism that could withstand the effects of friction for a prolonged period. Narasigadu's original mechanism utilised two O-rings placed at the top and bottom of a hollow, flat cylindrical plug of Techtron HVP polyphenylene sulphide, through which both the capillary and solid rod passed. The drawback of this mechanism was that both the Techtron plug and O-rings extruded outwards upon compression rather than inwards, and hence failed to maintain a leak-tight seal for a prolonged period. Furthermore, the attrition of the O-rings due to friction produced minute rubber particles which then accumulated within the cell, and on occasion blocked the ROLSI^{TM} capillary opening.

In order to address these weaknesses, the entire sealing mechanism was changed in this study. The new mechanism was adapted from the work of Nelson et al. (2016) and utilised a hollow PTFE cylindrical plug in conjunction with a hollow cylindrical brass plug (both with internal diameters of 3 mm). The latter functioned as the gland follower and was responsible for the compression of the PTFE plug, forcing it to compress in all possible directions. Extrusion of the PTFE upwards was inevitable thus the sealing nut had to be occasionally tightened in the presence of leaks and eventually the plug had to be replaced when the leaks persisted.

The contents of the cell were agitated by a Teflon coated magnetic bar which was placed within the cell. Actuation of the internal bar was achieved through the use of an external, circular shaped Neodymium magnet which was coupled to a D.C motor by way of a chain and sprocket mechanism. The intensity of the mixing was however not directly proportional to the speed of the motor, which was manipulated by altering its electrical power supply. This was due to the poor coupling of the magnet and motor, which resulted in de-coupling at higher motor speeds.

The initial design of the mixing mechanism displayed poor results, utilising a horseshoe magnet which had less magnetic effect relative to its Neodymium counterpart. However, replacement of the horseshoe magnet in this work did not yield the desired result as vortex formation within the binary mixture was not achieved, rendering the slight retrofit insignificant. Nelson et al. (2016), utilised a mixing mechanism that produced exceptional results in their work. This mixing system utilised an internal (PTFE) impeller, which enclosed a Neodymium ring magnet and rotated on the

axis of the volume compensation rod. The impeller was also actuated by a rotating Neodymium magnet, which was, in this case, coupled to an overhead stirring device. Retrofitting this mixing mechanism onto the equipment used in this work was not undertaken as it required the designing and machining of four new flanges for the cell housing, which was deemed a major time constraint.

In order to enhance the mixing of the cell contents, a low-temperature loading technique which was utilised in the work of Williams-Wynn (2016) was adopted for the volatile component, in a bid to increase the rate of absorption. This loading/charging technique was successful in enhancing the mixing, resulting in an acceptable equilibrium time of approximately 30 minutes depending on the nature of the liquid component.

4.1.2   Equilibrium cell temperature and pressure

In order to attain equilibrium within the cell, an isothermal environment was promoted through the use of a temperature regulated bath. The choice of fluid used was dependent on the overall temperature range across all isotherms in the study. Since all measurements were conducted at temperatures between (273.15 K–313.15 K), an ethylene-glycol water-mixture and an antifreeze-mixture (both with rust inhibitors) were selected as potential bath fluids. However, the antifreeze mixture alone, was eventually employed due to availability. The antifreeze mixture was contained in a 30 litre 304 stainless steel bath. The fabrication of the bath included a Fiberfrax internal lining, which served to dampen the temperature fluctuations within the bath.

The bath was fashioned with two glass viewing ports which were perfectly aligned, allowing for a clear line of sight of the cell contents. A light source was also placed behind the back viewing port in order to enhance the visibility of the cell contents. This was meant to allow the mixture within the cell to be monitored without the need to raise the cell housing from the bath, and thereby avoiding any distortions of the equilibrium conditions. This feature was however not used in this study since the bath fluid utilised was opaque. The bath was moved up in order to submerge the cell while the cell housing structure was maintained in a fixed position. This movement was achieved through the use of a manual scissor jack and an iron framework which guided the bath as it was lowered or raised.

The temperature of the fluid in the bath was regulated through the use of a Grant instruments Optima TX150 temperature controller with a stability of ± 0.01 K. When operating at temperatures below or near ambient temperature, a chiller unit was utilised to provide cooling. The temperature

within the equilibrium cell was measured using two Pt-100 (1/10 DIN) thermocouple probes. These were inserted into the top and bottom flanges through the wells which were specified in the previous section. This arrangement of the probes allowed the temperature gradient across the entire length of the cell to be measured. The probes, supplied by WIKA instruments were calibrated against a WIKA instruments Pt-100 standard probe using a WIKA type CTB 9100 oil bath.

The pressure within the cell was measured using a WIKA pressure transducer model type P-10 with a pressure operating range of $(0 - 25)$ MPa. The calibration of this transducer was done against a WIKA CPH 6000 standard pressure transducer. In order to avoid any error in the pressure measurement due to fluctuations in ambient conditions, the transducer was housed in an aluminium heating block, which was maintained at a constant temperature through the use of heating cartridges controlled by a Shinko ACS-13A series 1/16 DIN Digital Indicating Controller (Shinko DIC). For the measurements carried out in this work, the block temperature was held constant at 313.15 K. Signals from the temperature probes, as well as the pressure transducer, were relayed to an Agilent 34970A data acquisition unit which was responsible for their conversion into a digital format which could then be displayed on a desktop computer equipped with the Bench-Link data Logger software via an I/O port.

4.1.3   Sample analyses

The analyses of the cell contents were achieved through the use of gas chromatography (Shimadzu Gas Chromatograph (GC) 2010). Minute samples ranging from 0.01 mg to a few mg could be withdrawn from the cell through the ROLSI™ capillary. These micro-samples were ideal as they allowed no pressure distortions to occur within the cell. Thus the state of equilibrium within the mixture was never disturbed.

Sealing of the capillary output end was facilitated by a polyphenylene sulphide (PPS) seat inside the ROLSI™ (D = 3 mm, L = 3.5 mm), which was actuated by an electromagnet, acting on the spring located at the base of the sealing seat. The force applied on the capillary by the seat in order to facilitate the sealing was large enough to seal against cell pressures of up to 60 MPa due to the minute internal diameter of the capillary (Nelson, 2012).
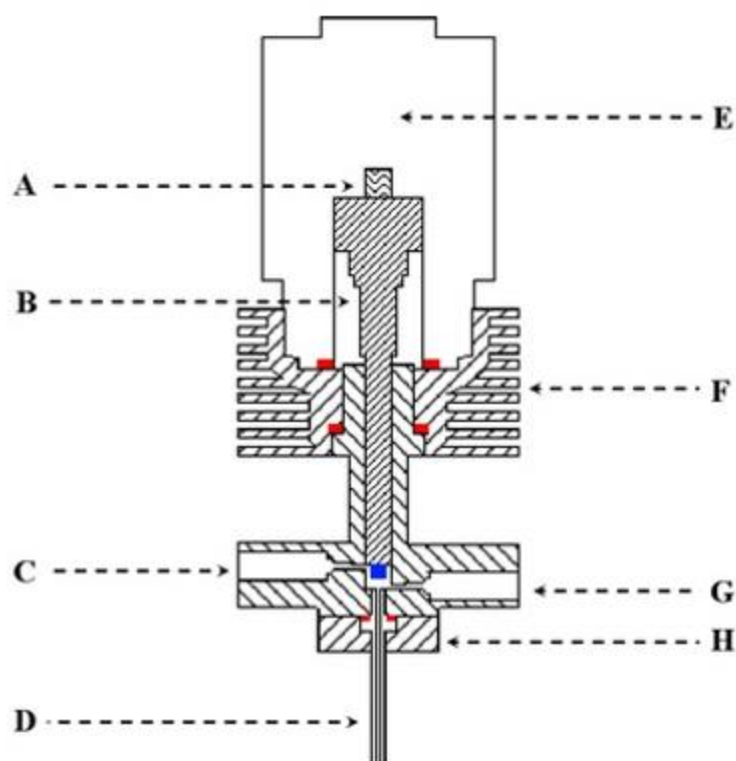
Figure 4-2: Cross-sectional drawing of the ROLSI™ (in open position): **A** – spring; **B** – vespel sealing seat; **C** – carrier gas inlet; **D** – capillary; **E** – electromagnet; **F** – cooling fins, **G** – carrier gas outlet; **H** – capillary sealing support, Blue marker – polymer seal; Red marker – O-rings (Nelson, 2012).

In order for a sample to be withdrawn, the seal within the ROLSI™ had to be broken, and this was achieved through the use of a Crouzet TOP948 electronic timer which was responsible for energising the ROLSI™ electromagnet for a specified time. Thereafter stopping the flow of current through the electromagnet resulted in the subsequent sealing of the capillary. Thus, the size of the sample was dependent on the time specified on the electronic timer and the internal diameter of the ROLSI™ capillary.

The sampled constituents of the cell where then vaporised in the base plate of the ROLSI™ which was thermo-regulated through the use of a heating cartridge. The heat was applied to this plate, primarily to vaporise the liquid samples, and to prevent any condensation of the vapour samples from taking place due to the Joule-Thompson cooling effects (Williams-Wynn, 2016).

The temperature which was specified for the heating cartridge was dependent on the components of the binary system and as such varied from (323.15 K – 423.15 K) when sampling in the liquid phase and was maintained at 433.15 K for the vapour phase. In order to attain a reasonable estimate of the heating cartridge temperature, a T-xy prediction for the binary pair was performed at the pressure of the carrier gas within the GC carrier gas lines through the use of Aspen Plus V8.4 software and the predictive Soave Redlich Kwong (PSRK) equation of state. The generated plot then allowed the estimation of the temperature required to vaporise the mixture, for a particular composition.

The ROLSI™ base plate was connected in a closed loop with the GC through the use of the carrier gas lines that were responsible for flushing the samples from the vaporisation chamber into the GC. These lines where thermoregulated by way of nichrome wire sheathed in glass fibre and thereafter insulated with Fiberfrax. The temperature of the carrier gas lines was maintained between (473.15 K - 493.15 K) by a Shinko DIC with feedback from a Pt-100 probe. The temperature of these lines was also dependent on the constituent chemicals in each of the binary systems measured.

The GC was equipped with a Porapak column (L = 3 m, ID = 2.1 m) which contained spherical porous polymer beads and was responsible for the separation of the analytes into their various constituents. The quantities of all the various constituents in the analyte were measured through the use of a thermal conductivity detector (TCD), which measured the conductivity of each constituent as it eluted from the column relative to the conductivity of the Helium carrier gas. The GC then interpreted the signals from the TCD in the form of peak areas in the chromatogram. These peak areas were then used in conjunction with the TCD calibration data to calculate the number of moles of each component in the sample. Photograph 4-1 depicts an overview of the entire apparatus including all the necessary auxiliary equipment.
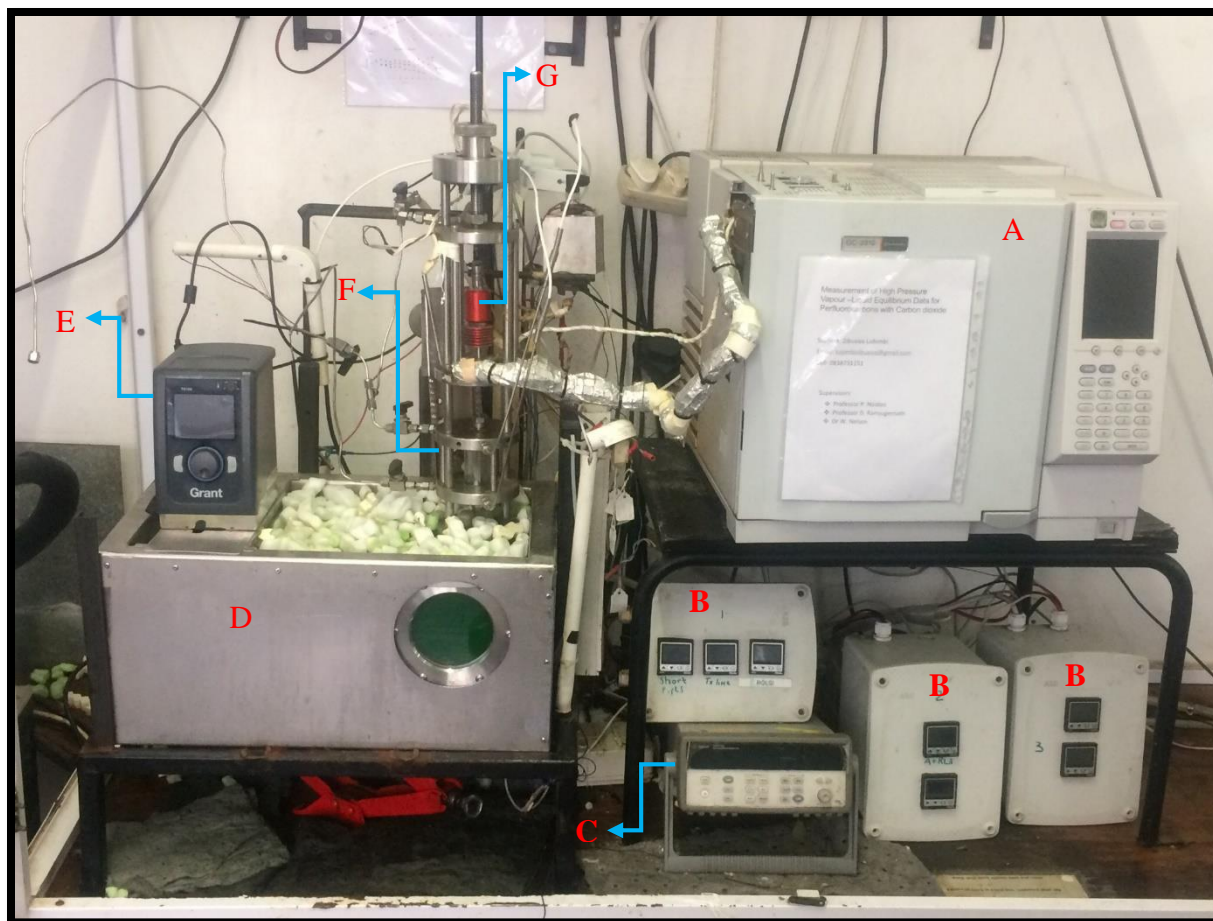
Photograph 4-1: Experimental set-up in the laboratory. **A:** Gas chromatograph, **B:** Digital temperature controllers (In casing boxes), **C:** Agilent data acquisition unit, **D:** Liquid bath, **E:** Grant temperature controller, **F:** Equilibrium cell and housing, **G:** ROLSI™.

4.2   Static synthetic apparatus

A secondary apparatus was used to affirm data which was generated using the static analytical apparatus. The apparatus constituted of a 10 cm^3 variable volume cell and was used to measure only T-P-x data. The design and commission of the apparatus were undertaken by the Thermodynamics Research Unit (TRU) at UKZN, for the purpose of measuring VLE, critical point, cloud point and P-V-T data.
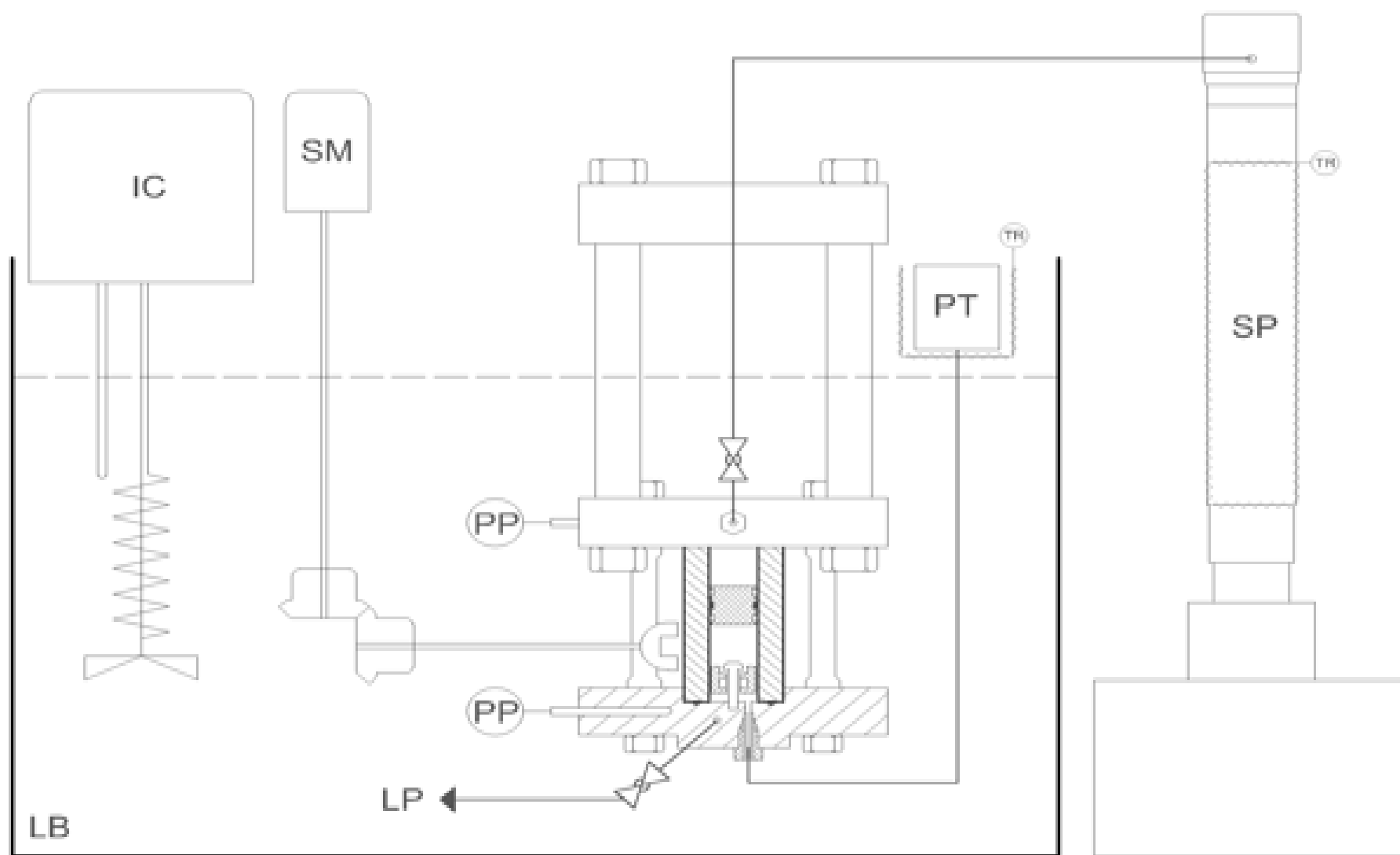
Figure 4-3: Schematic of the static synthetic apparatus with a variable volume cell. **IC:** immersion circulator, **LB:** Liquid bath, **PP:** Platinum resistance temperature probes, **SM:** Stirring mechanism, **LP:** Loading port, **SP:** Syringe pump, **PT:** Pressure transducer.(Nelson, 2017).

4.2.1 Variable volume cell and housing

The diagram displayed in Figure 4-3 shows the schematic of the static synthetic apparatus, including all the auxiliary equipment which is necessary for its appropriate function. The equilibrium cell used in this apparatus was also constructed from sapphire crystal into a tubular structure which was sealed between two SS 316 flanges with the assistance of O-rings. In this design, compression of the flanges onto the sapphire crystal was achieved through the use of three SS 316 bolts. The cell was fitted with an internal mixer and a SS 316 piston, resulting in the internal cavity of the cell having a capacity of approximately 10 cm^3. The purpose of the piston was to vary the volume within the cell, and this was achieved by utilising a high-pressure syringe pump (Teledyne ISCO, 100DM). Teflon guide rings further facilitated the movement of the piston within the cell. In order to prevent mixing of the pump fluid with the equilibrium mixture in the cell, an O-ring was fitted in the middle of the piston to seal the hydraulic fluid from the equilibrium mixture effectively.

The attainment of equilibrium was facilitated through the use of a stirring mechanism which utilised a nickel coated ring magnet which was placed within a PTFE mixer (OD =10 mm) and was fitted within the cell. This magnet was agitated via an external overhead stirring mechanism (Maxon A-max) which made use of a rotating Neodymium magnet (OD = 30 mm). The maintenance of isothermal conditions within the cell was achieved through the immersion of the cell housing into a temperature regulated liquid bath, which was fitted with two viewing windows and was fabricated from SS 316, with a capacity of 30 litres. A Grant, TX 150 immersion circulator was used to maintain the aforementioned isothermal conditions. In this work, water was used as the bath fluid due to the absence of any rust prone materials in the cell housing, its translucent nature and lastly the ease with which the fluid could be dried off the cell and its housing. The removal of all foreign matter from the cell housing was paramount since the structure had to be weighed to determine the quantities of each material in the binary mixture. The temperature within the cell was measured by two (Pt-100) temperature probes (WIKA, 1/10 DIN), while the pressure measurement was achieved via a single (WIKA, P-10) pressure transmitter. The conversion of the signals generated by the probes and the transmitter into standard units was carried out via an Agilent data acquisition unit, HP34970A, which was connected to a computer running Agilent proprietary software.

Chapter 5

5 Experimental procedures

5.1 Experimental procedure for the static analytical apparatus

The measurement of high-pressure vapour-liquid equilibrium data is inherently difficult as it requires the utmost accuracy in every data point measured. As such a meticulous, steadfast experimental procedure had to be developed by the experimentalist before embarking on the core measurements required. The general procedure used has been well documented by a number of authors namely, Tochigi et al. (2010), Soo (2011), Fonseca et al. (2011) and Nelson (2012), though the equipment used in the aforementioned studies might have differed slightly. Such procedures involve pressure and temperature calibration, GC detector calibration, vapour pressure measurement, equilibrium cell preparation and phase equilibrium measurements.

5.1.1 Temperature and pressure calibration

The calibration of the two Pt-100 probes was facilitated through the use of the CTH 6500 WIKA standard temperature probe in conjunction with a CTB 9100 WIKA thermo-regulated oil bath. The cell probes, together with the WIKA standard probe were submerged in the oil bath whilst their respective tips were aligned in perfect unison through fastening them all together to avoid any movement. This ensured that all three probes measured a relatively uniform temperature. The WIKA standard temperature probe was calibrated directly by WIKA and was stated to have an internal uncertainty of 0.02 K.

The Pt-100 probes were connected to an Agilent 34970A data acquisition unit which was also linked to a computer installed with Agilent proprietary software for recording and displaying the temperature values. The calibration process required the temperature of the oil bath to be increased and decreased monotonically up until the working range was covered. This allowed the experimenter to check for hysteresis within the probes. The measurements from each Pt-100 probe were logged and averaged over a period of 10 minutes after stabilisation had occurred. The temperature from the CTH standard probe was recorded manually from the display unit attached to the probe. The data from the three probes were then fitted into two separate first order polynomials, one for each Pt-100 probe against the standard reference probe.

Pressure

The equipment was fitted with a single P-10 pressure transducer which was calibrated against a (0 - 25) MPa CPH 6000 standard pressure transmitter which was supplied by WIKA with a stated accuracy of 0.025%. WIKA calibrated this instrument at ambient conditions. The atmospheric barometric pressure was provided by a Mensor CPC 3000 automated high-pressure calibrator, which was located in close proximity to the experimental equipment.

The equilibrium cell was loaded with nitrogen and the reference WIKA transducer connected to the discharge port of the equilibrium cell. The cell was then lowered into the bath, and the temperature maintained at 303.15 K, in order to avoid any temperature fluctuations during calibration. The pressure measured by the reference transducer was then zeroed before the commencement of the calibration as it showed a slight offset at atmospheric conditions. The hysteresis check was also performed for this instrument by monotonically increasing and decreasing the pressure over the selected working range for all measurements performed. The P-10 transducer was also connected to the Agilent 34970A data acquisition unit, and thus, the pressure measurements were logged and recorded on a desktop computer. At certain specified pressure intervals within the working range, the pressure in the cell was allowed to stabilise, and the data recorded by the Agilent was then collected and averaged. Pressure measured by the reference transducer was registered manually from the transducer display at intervals of 1-minute post stabilisation. The data obtained was then fitted to a 1st order polynomial.

5.1.2   Gas Chromatograph detector calibration

The compositional analyses of the respective phase samples in this study were performed using a Shimadzu Gas Chromatograph model GC 2010 which was fitted with a thermal conductivity detector (TCD), a three-metre Porapak column and utilised helium as the carrier gas. The response of the detector was calibrated prior to performing any measurements as the instrument lacked the ability to quantify any substance passing through the column without the aid of necessary correlations. The operating conditions of the GC per binary system are tabulated in Table 5-1.

Table 5-1: GC operating conditions for the Shimadzu gas chromatograph (GC-2010).

Binary systems	Injector Temp/ K	Oven Temp/ K	Detector Temp/ K	He flow ml/min	Detector current/ mA
$CO_2 - C_6H_{14}$	423.15	343.15	423.15	20	70
$CO_2 - C_8F_{18}$	523.15	498.15	523.15	20	70
$CO_2 - C_5H_4F_8O$	523.15	498.15	523.15	20	70
$CO_2 - C_7F_{16}$	523.15	473.15	523.15	20	60
$CO_2 - C_9F_{20}$	523.15	498.15	523.15	20	60

Calibration of pure components

The direct injection technique was employed in the calibration process, and as such, syringes were utilised to inject pure components of the particular chemicals used in the study. Hamilton syringes from Sigma-Aldrich of maximum volumes of 500 µl, 250 µl, and 50 µl were utilised for the gases while the liquid component was injected into the GC via SGE syringes with maximum volumes of 5 µl, 1 µl, and 0.5 µl. The accuracy of the experimentalist's technique in injecting consistent volumes was enhanced by the incorporation of Chaney adaptors (Hamilton syringes) into the gas syringes and repeatability adaptors for the liquid syringes, which allowed a specified volume to be set on the syringe before the loading of the syringe.

The injection of both the gas and liquid components was done at ambient conditions. The gas was sampled directly from the cylinder through a low-pressure regulator which was fitted with a septum on its output port. The temperature at the gas sampling point was measured via a thermometer while the atmospheric pressure was measured by the internal barometer of a Mensor CPC 3000 pneumatic high-speed pressure controller. This then allowed the moles of the gas injected to be calculated through the use of the ideal gas equation. This was a viable assumption since (compressibility (Z) ~ 1) for light gases and the injection was carried out at moderate temperature and low pressure (Williams-Wynn, 2016). The moles of the injected liquid were calculated from the molar density of the liquid, measured at the exact temperature of the liquid through a DSA 5000 density meter. All glass thermometers used had their temperature readings corrected relative to the CTH 6500 WIKA temperature probe.

Upon injection via the injector port of the GC, both the liquid and gas components would elicit a response from the TCD in the form of peaks in a chromatogram. The areas generated by the integration of these peaks were then used in conjunction with the actual number of moles of the injected components to construct first order polynomial curves. Only the gradient from the calibration equation was utilised in the calculation of the number of moles because the value of the intercept was distorted by the dead volume which was noted to be inherent in the syringes, particularly the gas syringes.

The linearity of the calibration was confirmed during the experimental work by altering the ROLSI™ sampling time, viz., increasing the size of the peak areas obtained for the same data set. The peak areas, however, had to remain within the calibration range for the test to be conclusive. If the mole fractions remained within the uncertainty, regardless of the different peak areas, the calibration data would be deemed linear.

Calibration of mixtures

During sampling of the equilibrium mixture especially at the low pressure, it is possible to obtain peak areas for the liquid and gas components which are below the generated calibration range. The increase of the ROLSI™ opening time to obtain larger samples might be an option in theory for combating this discrepancy. However, such an act usually results in the distortion of the equilibrium conditions within the mixture and is also prone to produce large GC peaks with tailing which would differ from the sharp GC peaks obtained during calibration, thus rendering the action moot. In this work, the calibration polynomials were extrapolated to peak areas which were well below the calibration range, particularly for the liquid components in the vapour phase. This action was validated by carrying out additional calibrations which utilised mixtures of the pure components with compatible substances, in a bid to drastically reduce the volume of the required substance upon injection into the GC. The available syringes (gas/liquid) were not capable of injecting the necessary minute volumes when pure components were used. Thus the preparation of mixtures was the only viable solution. This then allowed the experimenter to inject volumes of the required components which were below the working range of the syringes, thus facilitating the generation of calibration polynomials in the low peak area regions.

The polynomials generated from the direct injection of the pure components and the mixtures were then compared, and the discrepancies noted to be less than 5%, and thus extrapolation of the pure

component calibration was deemed acceptable. The uncertainty inherent in the mixture preparations was dependent on the Ohaus mass balance which was used to measure the masses of each component and the mole fractions of the aforementioned components. A concise description of the calculation procedure for all uncertainties is published in Appendix C.

For the calibration of mixtures to be carried out effectively, it required the following (a) identification of chemicals which were miscible with the pure components, (b) a resulting mixture with reasonable GC retention time and (c) a mixture which required acceptable GC conditions for separation. Separation of the peaks in the chromatogram was further facilitated by the disparity in the boiling temperatures of the mixture constituents. For the gaseous component, which was carbon dioxide, in this case, helium was the obvious choice for gas-mixture preparation, since it was the GC carrier gas and such produced no traces when it eluted the TCD.

The selection of a suitable liquid component for the fluoro-compound mixtures was not as straight forward. Thus it required the use of solubility parameters to determine which chemical species were miscible with the respective fluoro-compounds. The correlation developed by Hansen (1967) for the solubility of chemical species in solution asserted to the need for a small difference between the solubility parameter values of the two components in the mixture in order to obtain high solubility (x_1) of the solute within the mixture as highlighted in the following equation:

$$x_1 \propto \exp\left[\frac{-v_1\left(\delta_1' - \delta_2'\right)\phi_2^2}{RT}\right] \tag{5-1}$$

ϕ_2 – Volume fraction of the solvent
v_1 - Molar volume
δ - Solubility parameter

Thus chemical species with Hilderbrand solubility parameter values which were similar to those of the fluoro-compounds in question were selected. Table 5-2 lists the proposed components of each liquid mixture in conjunction with the respective Hilderbrand solubility parameter ranges for the chemical species.

Table 5-2: Constituents of the mixtures and Hilderbrand solubility parameter ranges for the respective chemical species.

Mixture	Fluorinated compound	Mixing compound
1	$C_5H_4F_8O$	m-xylene (C_8H_{10})
	[a]$(14.5 – 24.1)$ MPa$^{1/2}$	[b]$(16 – 16.8)$ MPa$^{1/2}$
2	C_7F_{16}	Pentane (C_5F_{12})
	[c]$(12.1- 12.9)$ MPa$^{1/2}$	[d]$(12.7 – 16.)$ MPa$^{1/2}$
3	C_9F_{20}	Hexane (C_6F_{14})
	[c]$(12.1- 12.9)$MPa$^{1/2}$	[d]$(12.7 – 16.)$ MPa$^{1/2}$

[a,b,c,d] Hilderbrand solubility parameter ranges for ethers, cyclic hydrocarbons, fluorinated hydrocarbons, and acyclic hydrocarbons respectively. Adapted from Gwinner et al. (2006).

The carbon dioxide + helium mixture was prepared in a one-litre cylinder which was fitted with an internal magnetic stirrer bar, and the mass of each constituent was determined through weighing the cylinder after loading each component. The resulting mixture was then agitated by an external horseshoe magnet which was coupled to a small D.C motor for mixture homogeneity. The gas mixture was also sampled directly from the cylinder through a low-pressure regulator which was fitted with a septum on its output port.

The liquid mixtures were prepared in small glass vials (8 ml), with the respective amounts of each component determined volumetrically. The number of moles of both the liquid and gas components was determined in the same manner as was previously explained for the pure components.

5.1.3   Equilibrium measurements

Preparation

Prior to performing any measurements on the equipment, its core, the equilibrium cell was tested for any leaks and was also properly cleaned. Due to the relatively small internal volume of the cell, any leak would result in distortions of the equilibrium conditions, resulting in erroneous measurements. The cleaning of the cell ensured that no contaminants polluted the chemicals used, as this could affect the vapour pressures of the components. In addition, all debris within the cell was effectively dislodged during cleaning, advertently preventing any clogging within the

ROLSI™ capillary. The cleaning was carried out before the measurement of every new system and hexane was the solution utilised. After the purging of the cleaning solution, the cell was then evacuated by way of a vacuum pump overnight to sub atmospheric pressures of approximately (-0.01 MPa) in order to remove all volatile impurities therewith.

The leak testing of the equilibrium cell was undertaken by pressuring the cell to approximately 9 MPa, which was 2 MPa higher than the predicted working pressure for all measurements. The gas used for this purpose was nitrogen, due to its low cost and availability.

The next phase, post pressurising the cell involved applying the Snoop® liquid leak detector onto all the compression fittings, valves, and seal joints. Foaming of the liquid was seen as an indicator of a leak, and these were quickly rectified by the action of tightening the respective fittings or replacing any ferrules if damaged. In the case of a leak in one of the two equilibrium cell seal joints, both O-rings were replaced. Due to the removal of O-rings from the ROLSI™ capillary and compensation rod sealing mechanism as mentioned in Chapter 4, the respective thumb screws could be tightened without the possibility of producing any debris that could contaminate the cell. Thus any leaks encountered at these two points were rectified by simply tightening, whilst avoiding over tightening, as this would restrict the movement of both the capillary and rod.

The cell and its housing were then submerged into the thermoregulated bath, which was maintained at 298.15 K. The temperature and pressure within the cell were then allowed to equilibrate and left overnight. The pressure measurements were recorded via the Agilent software thus any pressure drop in the system would be noted. If the readings suggested a leak in the system which could not be identified by application of Snoop® liquid leak detector, the next potential leak source to be examined was the ROLSI™ sealing polymer seat. This was carried out by disconnecting the carrier gas lines from the ROLSI™ base plate, blocking the inlet port and connecting a short 1/16 inch stainless steel pipe fitting onto the base plate outlet which was then immersed in a glass beaker filled with water. The cell was then pressurised once more while the ROLSI™ was off, and the beaker monitored for the presence of bubbles, which would indicate a leak. Another method for leak testing the ROLSI™ was to load the cell with a relatively cheap light gas, particularly nitrogen, then monitor the GC base line for any distortions whilst the sampler was off. In the presence of a leak, the ROLSI™ cooling fins were screwed further onto the base plate, as this brought the sealing seat closer to the capillary outlet. Failure of this action would result in the

removal of the ROLSI™ from the cell, examination of the polymer seat, followed by either the replacement of the seat or filing off the tip of the polymer to a length not less than 2.5 mm. The purpose of filing was to produce a flush surface adequate for sealing.

Another source of erroneous results that was meticulously tested for, prior to the commencement of measurements was the GC carrier gas loop. Leaks in this area would lead to a pressure drop and loss of portions of the sampled substance. An electronic gas leak detector with a high sensitivity for helium gas was used to test for leaks along the carrier gas lines from and to the GC, the connection ends of the packed column and at the injection port of the GC. The carrier gas lines were thermoregulated through the use of nichrome wire in order to maintain the lines at a temperature higher than the boiling point of the heaviest component in the binary mixture. This promoted complete vaporisation of all samples along the lines.

5.1.4 Vapour Pressure measurement

Saturated vapour pressure measurement for the pure components was conducted in order to affirm the validity of temperature and pressure calibrations as well as the purity of the chemicals. The presence of impurities in either the chemicals or the equilibrium cell would result in erroneous results. Thus measures were taken to ensure that the cell, along with all auxiliary loading/discharging lines were thoroughly purged of all foreign substances.

Volatile impurities in both the gaseous and liquid components were removed through the action of degassing. For the carbon dioxide, this was achieved by loading the cell while the temperature was maintained at a temperature of approximately 276.15 K. The low temperatures would in effect ensure that the carbon dioxide was charged in its liquid form. Thus, in order to purge the volatile impurities, the cell housing was raised from the bath, and heat was applied to the sapphire cell. To effectively heat the sapphire tube, the experimenter had to improvise, thus, a hand held blow dryer was used to blow hot air onto the cell's external surface, hence heating a larger surface area and in turn increasing the temperature of the cell contents at a rapid rate.

The purging of the volatile impurities commenced upon the development of convection currents within the liquid carbon dioxide. The charging/venting valve was rapidly opened and closed to ensure the removal of a moderate amount of gas. This sequence was finally stopped when approximately a quarter of the cell contents were evacuated. The less volatile liquid components were degassed through the use of the vacuum pump. The vapour pressures of the liquid

components were however measured using a different cell, one which was more suitable for the measurement of expensive liquid chemicals since it had a lower capacity. This cell was fabricated from stainless steel and had an internal volume of $10 \, cm^3$. The cell was fabricated into one complete cylindrical unit with only two access points. Thus no O-rings were necessary for sealing purposes, making the cell highly suitable for the measurement of liquid vapour pressures since it could easily seal under vacuum. The metal cell was clamped onto the cell housing of the sapphire cell for the purpose of effectively submerging it into the liquid bath. Vapour pressures of the liquid samples were measured via a P-10 pressure transducer, with a maximum pressure range of 0.5 MPa.

Following the degassing stage, the cell housing was submerged and the cell contents allowed to equilibrate. Values of both temperature and pressure over a five-minute time interval post equilibrium were recorded via the Agilent data acquisition unit in conjunction with the complimentary software. This data was then averaged and tabulated. Thereafter the temperature of the liquid bath was subsequently increased to attain the next data points. This process was continued until the desired range of vapour pressures was measured. Upon completion of measurements, the gas was vented off into the atmosphere, while the liquid was simply decanted from the stainless steel cell which was thereafter followed by VLE measurements using the sapphire cell.

5.1.5 HPVLE Measurements

Following the ethos of experimental work, the technique utilised in the measurement of each binary system was meticulously identical. Prior to undertaking any measurements, the equipment was prepared as highlighted above. The liquid component was always charged first into the cell, and this was achieved via the use of a two-stage Edward's vacuum pump which evacuated the equilibrium cell to sub-atmospheric pressures, thus producing the pressure difference that facilitated the charging of the liquid component. The equilibrium cell housing was always raised from the bath during evacuation in order to avoid any seepage of bath fluid into the cell which could occur if the ROLSI™ capillary thumb screw was not tightened adequately.

The mixing mechanism which was responsible for the agitation of the equilibrium cell contents was not efficient, as a result, the gaseous component (carbon dioxide) was always charged while the bath temperature was maintained at temperatures of approximately 276.15 K. The low

temperatures evoked a phase change in the component, changing it to a liquid. Since absorption of the gaseous component into the liquid is inversely proportional to temperature, loading at the low temperatures increased the rate of absorption and thus slightly negated the poor mixing effects. The degassing procedure for the gaseous component as previously mentioned also enhanced the mixing of the binary mixture. Equilibrium was normally achieved after approximately 30 minutes when the low-temperature charging technique was employed. Charging of liquid carbon dioxide could also be achieved while the bath liquid was maintained at high temperatures by applying an ice pack to the sapphire cell whilst the cell housing was raised from the bath.

The Grant TX 150 temperature regulator was used for altering the isothermal conditions in order to measure data at the various temperatures. The temperature regulation mechanism also relied on a chiller unit for maintaining temperatures below standard room conditions. When the temperature and pressure plot lines as recorded by the Agilent software stabilised for a maximum duration of approximately 15 minutes, chemical equilibrium was assumed to have been achieved, which highlighted that the mixture was ready for sampling.

However, before sampling of either phase, the temperature of the heating cartridge installed within the ROLSI™ base plate was altered in order to obtain satisfactory results. The temperatures utilised were approximated from the Predictive Soave Redlich Kwong (PSRK) plot of T-xy for the binary mixture. This plot was predicted at the pressure within the GC carrier gas lines. Hence, the plot would depict the temperatures at which complete vaporisation of the mixture would occur at particular compositions.

The vapour phase was always sampled first, by virtue of the need to perform multiple purges before satisfactory samples were obtained. The purging resulted in a pressure drop within the cell when sampling was conducted in the vapour phase whilst the liquid phase exhibited no such pressure fluctuations.

The need for purging was primarily due to the condensation of the liquid component on the tip of the ROLSI™ capillary which was usually dislodged through multiple purges (rapid sampling) and the increment of the base plate temperature (only for the vapour phase). The ROLSI™ capillary was moved from one phase to the other through the actuation of the differential screw, and the perfect position of the capillary tip in either phase was achieved by marking the screw support rods which then indicated the optimum capillary positions for sampling. The viewing windows could

not be used to observe the position of the capillary within the cell due to the opaque fluid used in the bath.

For each data point, it was required that there be at least five repeatable samples and these samples had to satisfy a repeatability criterion that required all calculated mole fractions to converge within a certain uncertainty for the liquid and vapour phase, which varied with each system. Failure to satisfy the criterion meant further purging was necessary. The phase envelope of the P-xy plot was completed through the actions of "stepping up" and "stepping down " the pressure in the cell by either venting off/ charging the volatile component, with the former being employed more often.

The chemicals utilised in this work were expensive. Thus a conservative measurement procedure was adopted in order to make use of the chemicals in a highly efficient manner. All the isotherms in each binary system were measured in a step-wise manner which entailed increasing the temperature to the next isotherm once the measurement of a single data set in the preceding isotherm was complete. When the top isotherm was finally reached and the measurements conducted, the pressure in the cell was then decreased to the next desired value in the top isotherm. Thereafter the same procedure was repeated by stepping down the temperature to a lower isotherm after measurement of a single data set until the initial isotherm was reached.

5.2   Experimental procedure for the static synthetic variable volume apparatus

Much like all static synthetic equipment used in phase equilibria measurement, the procedure used in this work entailed loading of known amounts of the required binary components through the action of weighing. However, slightly intricate steps were included to obtain the most accurate and precise results possible. Since sample analysis is not required when using the synthetic technique, calibrations were performed for only the temperature probes and the pressure transmitter, in the exact manner as was explained for the analytical equipment. The apparatus was thus operated as per the following steps:

   i.   The upper chamber within the equilibrium cell (which is located above the piston), was first charged with moderate amounts of fluid from the syringe pump. This fluid was used as a buffer so as to prevent the contact of the piston with the top flange when the cell was pressurised. The non-rotating needle valve (Parker, 10V series) which was installed on the

cell – syringe pump line was thereafter closed, only to be opened at the commencement of the actual measurements.

ii. The cell and its housing were then thoroughly dried of any and all fluid on the external surfaces through the use of compressed air. This action also resulted in the expulsion of all foreign material which would have adhered to the cell and housing structure. This was done to ascertain that no foreign material interfered with the weight of the structure.

iii. Thereafter the cell was then placed under vacuum by connecting a two stage vacuum pump (Edwards RV3) onto the loading line. This process was usually carried out overnight to ensure proper evacuation.

iv. Once the cell was sufficiently evacuated to pressures of approximately -0.01 MPa, the non-rotating needle valve (Parker, 10V series), which was also installed on the loading line was sufficiently closed. The cell housing and the connected pressure transmitter were then removed from the support frame for the purpose of weighing the structure.

v. Following the initial weighing, all possible traces of air within the cell were dispelled through the load-purge technique, which was carried out using the gaseous component. After sufficient load-purge cycles, the cell was filled with relatively large quantities of the gas. The pressure within the cell was then measured for the purpose of effectively reducing it to a slightly positive value of approximately 0.14 MPa, via the careful opening of the needle valve. The pressure was never allowed to reach atmospheric levels, as this would introduce air into the cell. After the pressure reduction, the cell and housing were again weighed.

vi. This was then followed by the loading of the liquid component. Prior to being charged into the cell, the liquid was degassed in a Büchner flask which was connected to the vacuum pump. The subsequent loading was carried out using a syringe, which was fitted with a nut and a rubber seal. Since only a slight positive pressure of the gas was present within the cell, loading via a syringe was possible. After the successful loading of the liquid component and the closure of the valve, the vacuum pump was again used to remove any residual liquid from the valve, as it would interfere with the mass during the weighing of the liquid infused cell and its housing.

vii. Further charging of the gaseous component was undertaken in order to increase the volume of the mixture, viz., increase the mass of both components, which in turn increased the

probability of obtaining the most accurate results. Before charging, the housing structure was inverted, in order to allow the depression of the piston upon entry of the gas, resulting in the loading of larger amounts of the lighter component. During the charging of the gas, the mixer was activated to enhance the absorption rate of the gas into the liquid. The housing structure was thereafter weighed and its mass recorded for the last time.

viii.   The housing structure was then returned onto its frame, the syringe pump connected and the structure was then submerged in the bath liquid. The pressure within the two chambers in the cell was allowed to equilibrate, and the stirring mechanism activated for approximately 10 minutes before the next step commenced.

ix.   The binary mixture which was being rigorously agitated was then compressed through the action of the syringe pump and the piston at a rate of (10 µl/min) to obtain the bubble point.

x.   Two complementary techniques were employed in attaining the bubble point; these were by visual observation and the pressure technique. For the former, as the name implies, the mixture was observed up until the transition to a single phase occurred, and this was characterised by the disappearance of the last bubble within the mixture.

xi.   The pressure technique entailed monitoring of the pressure within the cell, and thus the bubble point was characterised by a sudden spike in pressure, with the pressure reading just before the increase being the desired bubble point. Figure 5-1 depicts the aforementioned phenomenon.
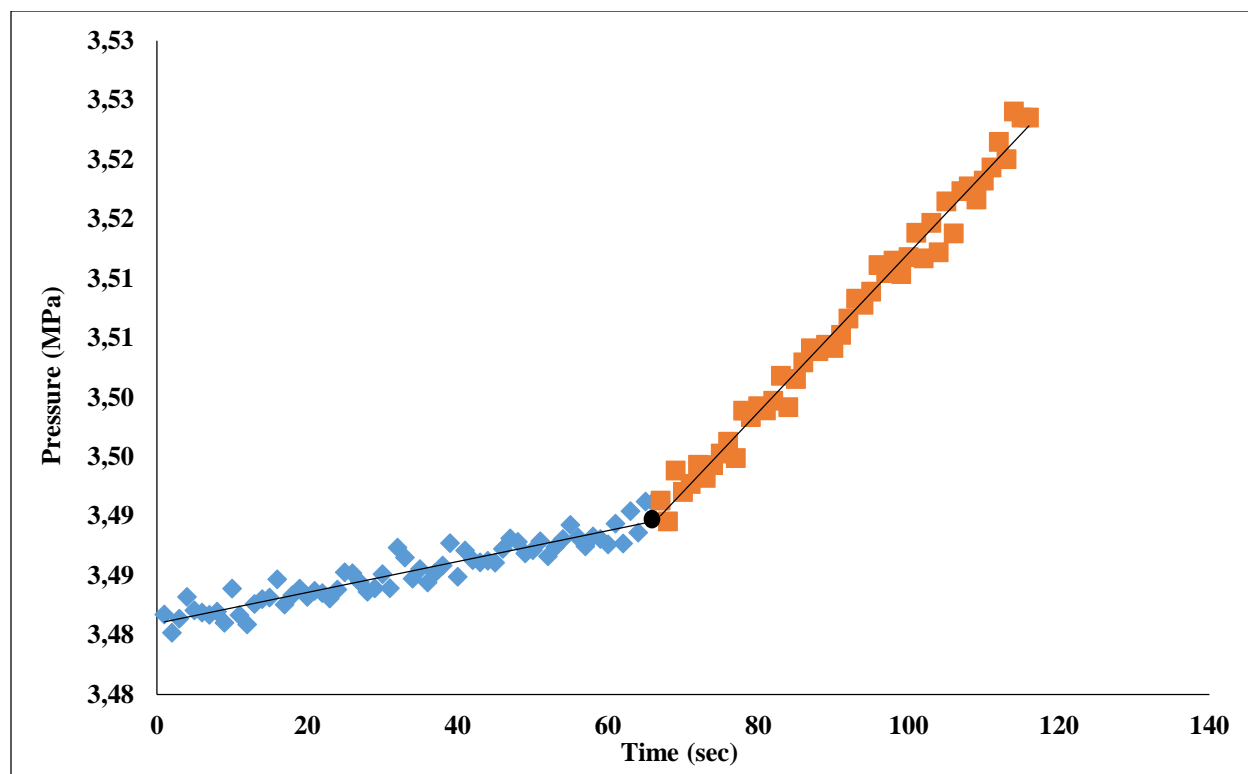
Figure 5-1: Pressure vs time chart for the carbon dioxide (1) + 1,1,2,2-tetrafluoroethyl 2,2,3,3-tetrafluoropropyl ether (2) system. (■) mixture exists as two phases, (■) mixture exists as a single phase, (●) bubble point.

Chapter 6

6 Theoretical analysis of phase equilibria data

The inception of advanced computing hardware, coupled with sophisticated software packages, has afforded researchers the ability to correlate phase equilibria data in a timely manner. The importance of the aforementioned data in the design of equipment and processes is still paramount, the only hindrance being the rigorous and costly nature of conducting the necessary experimental work. The next stage in phase equilibria studies is aimed at attaining the ability of accurately predicting HPVLE data without the need of any experimental input, which is currently an elusive endeavour (Raal and Mühlbauer, 1997; Gmehling and Kolbe, 2012). However, to achieve this goal, an array of experimentally measured phase equilibria data is still required, in a bid to perfect the theoretical and empirical derived formulae that are essential for the predictions. The capability to effectively predict phase behaviour data is crucial because engineers may not have all the necessary data needed, for all required mixtures at the conditions of interest for design purposes. Thus accurate extrapolation of data is imperative.

6.1 Analyses of HPVLE Data

The ability to describe/analyse phase equilibria data stems from the understanding of a basic criterion which becomes valid only when the phases are at equilibrium. This standard is represented by the following formulae for a vapour – liquid system:

$$\hat{f}_i^l(T,P,x_i) = \hat{f}_i^v(T,P,y_i) \tag{6-2}$$

Where $\hat{f}_i^l$ and $\hat{f}_i^v$ represent the fugacities of the liquid and vapour phases respectively. The correlation of the fugacities above was impractical when described based on first principles, as the resulting equation was very difficult to compute (Prausnitz et al., 1998). As a result the fugacities for the respective phases present at equilibrium were related to temperature, pressure and composition via the use of the activity coefficient (γ) and the fugacity coefficient (Φ), resulting in the development of analytical methods which were based on the two coefficients for the description of phase equilibria data. These methods are termed the combined ($\gamma - \Phi$), direct ($\Phi -$

Φ) and modern direct methods. The combined method uses both the activity and the fugacity coefficients to describe the non-idealities of the liquid and vapour phases respectively according to the following correlation:

$$\hat{f}_i^l = x_i \gamma_i f_i^o = \hat{f}_i^v = y_i \hat{\phi}_i^v P \tag{6-3}$$

Where f_i^o is the fugacity of pure component i at standard state and $\hat{\phi}_i^v$ is the fugacity coefficient of component i in the vapour phase. The fugacity coefficient and activity coefficient are generated from an equation of state and the excess Gibbs energy model respectively. The $(\gamma - \phi)$ method allows for accurate analysis of non-ideal mixtures virtue of the activity coefficient model's ability to generate large excess Gibbs free energies of mixing (Orbey and Sandler, 1998). However this method has substantial drawbacks which resulted in the development of the $(\phi - \phi)$ method. The disadvantages of the $(\gamma - \phi)$ method have been extensively reviewed by, Raal and Mühlbauer (1997), Orbey and Sandler (1998) and Naidoo (2004). The $(\phi - \phi)$ method, as the symbols suggest, uses the fugacity coefficient to describe the non-idealities in both the vapour and liquid phases as follows:

$$\hat{f}_i^l = x_i \hat{\phi}_i^l = \hat{f}_i^v = y_i \hat{\phi}_i^v \tag{6-3}$$

This method, however, fell short in its ability to describe data for complex systems, which then led to the development of what is termed the modern direct method. This method uses equation of state mixing rules (EoS) to incorporate activity coefficients (excess free energy models) into the fugacity coefficients of the liquid and vapour phases. The relationship between the EoS and the activity coefficient was formulated by Orbey and Sandler (1998) as follows:

$$\gamma_i = \left[\hat{\phi}_i(T, P, x_i) / \phi_i(T, P) \right] \tag{6-4}$$

Where $\hat{\phi}_i(T, P, x_i)$ is the fugacity coefficient of species i in the mixture, and $\phi_i(T, P)$ is the pure component fugacity coefficient. Both parameters are derived from the EoS at the temperature and pressure of the relevant mixture. The combination of equation (6-4) with the molar excess Gibbs free energy, which is given by the correlation (6-5) results in the mixture EoS models which are capable of describing high degrees of non-ideality.

$$\frac{G^E}{RT} = \sum x_i \ln \gamma_i \tag{6-5}$$

Thus the modern direct method was used in this study, as it has the highest probability of achieving good extrapolation of VLE data. For the derivation of all the equations above, and definitions of fugacity coefficient and activity coefficient, the reader is referred to the following texts Raal and Mühlbauer (1997), Orbey and Sandler (1998) and Kontogeorgis and Folas (2009).

6.2 Thermodynamic models used in the study

The VLE data generated in this work was regressed through the use of the modern direct method in conjunction with a configuration of models which included an equation of state EoS, mixing rule, alpha function and an activity coefficient model. The following section presents a discussion of the models and the rationale behind their selection.

6.2.1 Cubic equation of state: Peng-Robinson (Peng –Rob)

In phase equilibria, the foundation for the most extensive calculations is achieved through the use of equations of state. The Peng – Robinson EoS is a product of the Van der Waals EoS,:

$$P = \frac{RT}{(V-b)} - \frac{a}{v^2} \tag{6-6}$$

which was the very first to give a qualitative analysis of the vapour, liquid and phase transitions (Orbey and Sandler, 1998). This then resulted in a score of equations emanating from the Van der Waals, all seeking to improve upon the limitation of the original, but the Soave-Redlich-Kwong (SRK) and the Peng-Robinson where the most successful (Sadus, 2012). The latter was however developed to improve upon the former, which had difficulties representing the liquid phase densities and also showed poor accuracy near the critical region. Peng and Robinson (1976) thus introduced a different volume dependence and changed the temperature dependence of the α, which was first introduced by Wilson (1964), resulting in the following pressure explicit form:

$$P = \frac{RT}{(V-b)} - \frac{a_c \alpha}{v(v+b) + b(v-b)} \tag{6-7}$$

With values of the parameters a and b at the critical point being:

$$a(T_c) = 0.45724 \frac{R^2 T_c^2}{P_c} \tag{6-8}$$

$$b(T_c) = 0.07780 \frac{RT_c}{P_c} \qquad (6\text{-}9)$$

However the repulsive term $(v - b)$ in the Peng-Robinson EoS, which includes the parameter b has been proven to be incorrect through statistical mechanics. Thus the success of the equation of states from the Van der Waal family, regardless of the erroneous repulsive term, has been attributed to the improvement of the temperature dependent term. This improvement was however achieved at the expense of drastically increasing the complexity of the EoS and according to Sadus (2012), the improvement had no theoretical basis.

The alpha function which was used in equation (6-7) managed to result in the accurate vapour pressure predictions for hydrocarbons, particularly gasoline fractions, (Orbey and Sandler, 1998), and is represented by the formulae:

$$\alpha = [1 + (0.37464) + 1.54226\omega - 0.2699\omega^2 \times (1 - T_r^{0.5})]^2 \qquad (6\text{-}10)$$

where ω is the acentric factor.

The Peng-Robinson EoS is thus a widely used EoS in industry but it is hardly perfect. It fails at accurately predicting data for long chain molecules and also predicting saturation pressure for vapour liquid equilibrium data, only to highlight a few. A detailed review of the shortcomings of the most successful equations of state from the Van der Waal family was carried out by Abbott (1979). As a result, these models have been modified to improve upon their predictive capabilities in a number of ways which will be highlighted below.

6.2.2   Alpha function: Mathias Copeman.

Since the inception of the Van der Waals EoS, numerous alpha functions have been developed in a bid to improve the ability of the various EoS in representing all the thermodynamic properties of fluids at different pressure and temperature ranges. The original alpha function which was implemented into the Peng-Robinson EoS was developed by Soave (1972). The drawback of this function was its inability to predict vapour pressures at low temperatures, including temperatures above the critical point (Twu et al., 2002). This, therefore, is one of the major reasons that resulted in the development of numerous alpha functions, which seek to change the temperature dependent

function in the equations of state from the Van der Waal family, thus improving vapour pressure prediction, particularly for polar fluids (Privat and Jaubert, 2012).

In order to achieve an accurate representation of the vapour pressures, an alpha function should conform to a set of rules (Coquelet et al., 2004), which are:

1. The function must be positive and finite at all possible temperatures.
2. They must reduce to one at the critical point.
3. When the temperature tends to infinity, the functions should reduce to zero.
4. They must emulate their first and second derivatives and be continuous at temperatures above zero.

A list of some of the most utilised alpha functions, highlighting how they conform to the rules mentioned above is tabulated in Table 6-1:

Table 6-1: Characteristics of Alpha functions. Adapted from (Young et al., 2016).

Alpha function Main author(yr)	References	Coquelet's rules				Number of Adjustable parameters
		1	**2**	**3**	**4**	
Soave (1972)	Soave (1972)	yes	yes	yes	yes	1
Heyen (1980)	(Heyen, 1980)	yes	yes	yes	yes	2
Harmens-Knapp(1980)	(Harmens and Knapp, 1980)	yes	yes	yes	yes	2
Mathias (1983)	(Mathias, 1983)	yes	No	yes	yes	2
Mathias-Copeman(1983)	(Mathias and Copeman, 1983)	yes	No	yes	yes	3
Gibbons-Laughton(1984)	Gibbons and Laughton (1984)	No	No	yes	yes	3
Soave(1984)	(Soave, 1984)	NO	No	yes	yes	2
Stryjek-Vera(1986)	(Stryjek and Vera, 1986)	yes	No	yes	yes	2
Yu-Lu(1987)	(Yu and Lu, 1987)	yes	yes	yes	yes	1
Trebble-Bishnoi(1987)	(Trebble and Bishnoi, 1987)	yes	yes	yes	yes	3
Melhem (1989)	(Melhem et al., 1989)	yes	yes	yes	yes	1
Androulakis(1989)	(Androulakis et al., 1989)	No	No	yes	yes	2
Schwartzentruber-renon(1989)	(Schwartzentruber et al., 1990)	yes	No	yes	yes	3
Almeida-Aznar-Telles(1991)	(Almeida et al., 1991)	yes	yes	yes	yes	3
Twu(1991)	(Twu et al., 1991)	yes	yes	yes	yes	3
Soave(1993)	(Soave, 1993)	No	No	yes	yes	3
Gasem (2001)	(Gasem et al., 2001)	yes	yes	yes	yes	2
Coquelet (2004)	(Coquelet et al., 2004)	yes	yes	yes	yes	3
Haghtalab (2010)	(Haghtalab et al., 2010)	yes	yes	yes	yes	3
Saffari-Zahedi (2013)	(Saffari and Zahedi, 2013)	yes	yes	yes	yes	3

Alpha functions are mostly used for the representation of vapour pressures, which therefore means that these pressures will mostly be measured at subcritical temperatures, as was done in this work. Thus the failure to conform to the first two of Coquelet et al.'s rules will not affect the functions ability to represent sub critical vapour pressures, since the first two rules apply to an extensive temperature range. Therefore Coquelet et al.'s rules would not suffice in effectively streamlining the alpha functions, to select only one.

A recent study was carried out by Young et al. (2016) in order to investigate the performance of alpha functions, with the aim of simplifying the process of selecting a suitable function. The parameters of each function were evaluated for fifty-six (56) compounds which were grouped as (hydrocarbons), (water), (permanent gases), (alcohols), (organic acids) and (halogen compounds). The evaluation was done at the same conditions and utilised data from the Data compilation of pure compound properties (DIPPR) data base. The functions developed by Mathias and Copeman (1983), Androulakis et al. (1989), Schwartzentruber et al. (1990) and Almeida et al. (1991) obtained the best overall results, with the Mathias-Copeman showing the best results for permanent gases. The reason for the use of the Mathias-Copeman alpha function in this work is also related to its previously stated attribute since the present study was focused on the low boiling permanent gas carbon dioxide. The Mathias-Copeman alpha function is represented by the correlation:

$$\alpha_i(T) = \left[1 + C_{1,i}\left(1 - \sqrt{T_{R,i}}\right) + C_{2,i}(1 - \sqrt{T_{R,i}})^2 + C_{3,i}(1 - \sqrt{T_{R,i}})^3\right]^2 \qquad \text{(6-11)}$$

Where the function parameters are represented by $C_{1,i}$, $C_{2,i}$ and $C_{3,i}$, with $T_{R,i}$ signifying the reduced temperature of species i. These parameters are generated through the regression of vapour pressure data.

6.2.3 Mixing rules: Wong-Sandler

Models of the fluid state, particularly equations of state, were initially developed for pure substances, thus in order to cater for mixtures, these correlations were extended (Sadus, 2012). This was achieved through the use of the mixing and combining rules. These rules, therefore, correlate the properties of the pure component to those of the mixture. Before the array of mixing rules which are currently available was developed, the Van der Waals one-fluid mixing rules were the standard. These are represented by:

$$a = \sum\sum x_i x_j \, a_{ij} \tag{6-12}$$

$$b = \sum\sum x_i x_j \, b_{ij} \tag{6-13}$$

Where a_{ij} and b_{ij} are evaluated through the use of combining rules, which essentially optimise the agreement between theory and experimental data. The combining rules are correlated as follows:

$$a_{ij} = \sqrt{a_{ii}a_{jj}}\left(1 - k_{ij}\right) \tag{6-14}$$

$$b_{ij} = {}^1\!/_2 \left(b_{ii} + b_{jj}\right)\left(1 - l_{ij}\right) \tag{6-15}$$

With k_{ij} and l_{ij} representing the binary interaction parameters, with the former resulting from fitting EoS predictions to experimental VLE data, whilst the latter is usually omitted as it has been noted to have near negligible impact on the analysis of high pressure phase equilibria data (Sadus, 2012). The importance of the k_{ij} parameter is validated by various experimental observations (Sadus and Young, 1985; Sadus et al., 1988) which have highlighted the parameters ability to reflect the strength of unlike interactions within a mixture. The Peng –Robinson EoS in its original state utilises the Van der Waal one fluid mixing rules and the configuration of the EoS with the mixing rules has been noted to effectively describe phase equilibria data for mixtures of hydrocarbons and hydrocarbons with inorganic gases (Sandler, 1994). However these mixing rules are hindered by the fact that they are only useful in mixtures with moderate solution non-ideality whereas in most industries the chemical mixtures of interest have a relatively higher degree of non-ideality. In order to circumvent this drawback, mixing rules that combine EoS models with activity coefficient models were developed.

Huron and Vidal (1979) were the first to succeed in this endeavour. They achieved this through empirical means, by dictating that the EoS of the mixture at the density of the liquid should behave in the same manner as an activity coefficient model (Orbey and Sandler, 1998). The mixing rule was then developed through the combination of the excess Gibbs energy of mixing for an EoS and that of an activity coefficient model as follows:

$$G_\gamma^{ex}(T, P = \infty, x) = G_{EOS}^{ex}(T, P = \infty, x) \tag{6-16}$$

Equation (6-16) was correlated at infinite pressure in order to obtain the desired result of ensuring that a liquid root of the EoS was utilised. The resulting mixing rule was partially successful but had insurmountable flaws in its inability to describe mixtures that the one fluid Van der Waal mixing rules could effectively describe and also failed to satisfy the composition dependency, which is required for the second virial coefficient. Since the virial expansion is theoretically correct, a mixing rule with the same low-density compositional dependency as the expansion will effectively be justified. These failures led to the development of the modified Huron – Vidal second order model (Sandler, 1994), which also failed, like its predecessor, to result in a second virial coefficient which is quadratic in composition, thus rendering the mixing rule incompatible with statistic mechanics.

Wong and Sandler (1992) eventually managed to develop mixing rules which succeeded where the Huron-Vidal rules failed. This was achieved through the use of the excess Helmholtz free – energy (A^E) at an infinite pressure, which therefore meant that A^E was not as intricately dependent on pressure, and the assumption that $V^E = 0$, was rendered negligible. The mixing rule parameters are formulated based on the following condition:

$$A_{EOS}^{ex} = A_\gamma^{ex}(T, P = \infty, x_i) = A_\gamma^{ex}(T, low, P, x_i) = G_\gamma^{ex}(T, low, P, x_i) \tag{6-17}$$

Where the subscripts denoted by EoS and γ represent equation of state and activity coefficient model respectively. The resulting mixing rules are then correlated as follows:

$$a_m = RT(Z)\frac{W}{(1 - W)}$$

$$\tag{6-18}$$

$$b_m = \frac{Z}{(1 - W)}$$

Where,

$$Z = \sum\sum x_i x_j \left(b - \frac{a}{RT}\right)_{ij} \tag{6-20}$$

$$W = \sum x_i \frac{a_i}{b_i RT} + \frac{G^{ex}(x_i)}{\sigma RT} \tag{6-21}$$

The constant σ depends on the equation of state being used and for the Peng-Robinson EoS, this constant is correlated as:

$$\sigma = -\frac{1}{\sqrt{2}} \ln(1 + \sqrt{2}) \tag{6-22}$$

The mixing rule uses the following combining rules as restrictions for the EoS parameters a and b:

$$b_{ij} - \frac{a_{ij}}{RT} = \frac{1}{2}\left[\left(\frac{b_{ii} - a_{ij}}{RT}\right) + \left(b_{jj} + \frac{a_{jj}}{RT}\right)\right](1 - k_{ij}) \tag{6-23}$$

6.2.4   Activity coefficient model: NRTL

In order to effectively assess the properties of nonideal liquid mixtures an activity coefficient model is utilised, which relates the Gibbs excess function to the liquid composition. The local composition concept which was developed by Wilson (1964) was very instrumental in this regard, resulting in a straightforward equation that was capable of generalising multi-component mixtures without the aid of ternary parameters (Renon and Prausnitz, 1969). The concept above deals with areas within a mixture that have a different composition compared to the overall mixture, and these areas also account for the non-randomness of molecular orientation within the mixture (Nelson, 2012).

However, the inapplicability of the Wilson equation to liquid mixtures with partial miscibility resulted in the necessary platform for the development of the non–random two liquid equation (NRTL), which is correlated as follows:

$$\frac{G^E}{RT} = x_i x_j \left(\frac{\tau_{ji} G_{ji}}{x_i + x_j G_{ji}} + \frac{\tau_{ij} G_{ij}}{x_j + x_i G_{ij}}\right) \tag{6-24}$$

With the parameters τ_{ji} and τ_{ij} being adjustable and $(G_{ij} = exp(-\sigma\tau_{ij}))$. The activity coefficient of the model is represented by

$$\ln \gamma_i = x_2^2 \left[\tau_{ji} \left(\frac{G_{ji}}{x_i + G_{ji}x_2}\right)^2 + \frac{\tau_{ij} G_{ij}}{\left(x_2 + G_{ij}x_i\right)^2}\right] \tag{6-25}$$

While $\ln \gamma_j$ is obtained through interchanging the subscripts in equation (6-25) above. In the software package Aspen Plus V 8.4, which was employed in the regression of all experimental data in this work, the NRTL model is defined as follows:

$$\tau_{ij} = a_{ij} + {b_{ij}}/_T + e_{ij} \ln T + f_{ij}T \qquad (6\text{-}26)$$

Where τ_{ij} is the interaction binary parameter and a_{ij}, b_{ij}, e_{ij}, f_{ij} are obtained through the regression of the experimental data. The parameters e_{ij}, f_{ij} where not used in this work, and as such where assigned a value of zero. The non-randomness parameter is correlated by the following formulae:

$$\alpha_{ij} = c_{ij} + d_{ij}(T - 273.15) \qquad (6\text{-}27)$$

Where d_{ij} is set to zero, thus resulting in the reduction of the above correlation into an identity of the form ($\alpha_{ij} = c_{ij}$). The parameter c_{ij} is selected based on the chemical characteristics of the components which make up the mixture and should lie within the bounds of 0.2 and 0.5 for all fluids. The NRTL model is the simplest of all the local composition equations and also has arguably the most sound semi-theoretical basis (Renon and Prausnitz, 1968), thus it was used in this work, with the adjustable parameter fixed at 0.3, which is ideal for nonpolar liquids. The rationale behind the selection of the value for the parameter was based on the analysis carried out by Renon and Prausnitz (1968) on an array of binary mixtures.

6.3   Data regression

The regression of experimental data was conducted through the use of the propriety software from Aspen technology, Aspen Plus V 8.4, whilst utilising the following configuration of models: Peng –Robinson EoS, with the incorporation of the Mathias–Copeman alpha function, the Wong–Sandler mixing rules and the NRTL activity coefficient model. This particular configuration of models has been successfully used in the regression of binary systems consisting of fluorinated compounds, (Valtz et al., 2011; Nandi et al., 2013; Tshibangu et al., 2014; Bengesai, 2016), thus its use in this work was justified by its exceptional performance and the rationale explained above. Table 6-2 highlights the models used including the procedure for the regression as was carried out on the Aspen platform. The method described is only for the PR-MC-WS-NRTL model.

Table 6-2: Aspen VLE regression procedure.

Step	Item	Description
1	**Components**	The binary components are selected from the extensive NIST compound data banks, with the lighter component being preferentially selected first.
2	**Method**	The configuration of models used for the regression consists of the Peng-Robinson EoS, Mathias-Copeman alpha function, Wong-Sandler mixing rules and NRTL activity coefficient. Therefore this step deals with configuring the software to use the aforementioned models effectively.
	❖ Specification	The Aspen database contains numerous EoS-mixing rule configurations which are referred to as methods. In this case, the PRWS base method is selected.
	❖ Selected method	This section allows the user to specify both the activity coefficient model and the alpha function to be used. In this case **(GMRENON)** was chosen under the GAMMA property, for the NRTL model. The Mathias-Copeman alpha function was then selected through designating an **option code** of **2** to the **(ESPRWS)** model. Each alpha function which can be used with the PRWS in Aspen is categorised with an option code/s.
	❖ Parameter	In the regression procedure employed in this work, Mathias-Copeman parameters were regressed separately, then fitted as pure component parameters for each respective binary mixture component during the regression of the VLE data.
3	**Data**	The type of data to be utilised is specified at this stage, with regard to whether it is mixture or pure component data.
	❖ D-1 mixture	When mixture data type is selected, the available components are then specified, including the type of the data in question (i.e., P-xy) and the isothermal temperature. Lastly, the P-xy data is keyed in.
4	**Regression**	Prior to regressing the data, parameters for the PRWS, PRMCP, and NRTL models were specified.
	❖ R-1	The algorithm used for regression was the Britte–Luecke, which preceded the Deming algorithm which was used to generate the initial value. Both algorithms were used in order to promote the convergence of the Britte–Luecke (Britte, 1973). These algorithms were used in conjunction with the ordinary least squares objective function, which seeks to minimise the pressure and vapour composition in VLE data. This particular function defines the error as the difference between the experimental and calculated values, thus aims to minimise the quadratic error summation over the data set (López et al., 2006).
5	**Results**	Regression of the experimental data led to the generation of three model parameters (k_{ij}, τ_{ij} and τ_{ji}), the residual root mean square error (RRMSE), calculated pressure and vapour compositions and lastly the deviations between the calculated and experimental data.

Experimental VLE data should be both accurate and precise. The former is determined via thermodynamic consistency testing, though the test can be prone to false positive results, while false negatives are improbable (Bengesai, 2016). The method of carrying out these tests have been reviewed by Naidoo (2004). The precision of the data can be noted through observing smoothness of the generated phase envelope and the errors.

The deviation Bias and the absolute average relative deviation (AARD), which quantify the fit of the model to the experimental data, were observed to have been well below 2% in the studies of liquid fluoro-systems, which were conducted by Nandi et al. (2013), Tshibangu et al. (2014) and Bengesai et al. (2016). In the study of fluoro-systems, azeotropic behaviour was observed by Tshibangu (2015), for the hydrogen sulphide (1) + perfluorohexane (2) system. However, the PR-MC-WS-NRTL model was not used to describe the phase behaviour of this particular system, with the author opting to use the Soave-Redlich-Kwong EoS with the Mathias-Copeman alpha function and predictive Soave-Redlich-Kwong, modified Huron Vidal 1 or 2 mixing rules and utilising the NRTL activity coefficient. The aforementioned model configurations were abbreviated as SRK-MC-PSRK-NRTL, SRK-MC-MHV1-NRTL, and SRK-MC-MHV2-NRTL, with the SRK-MC-MHV1-NRTL producing an adequate representation.

Chapter 7

7 Results and discussion

7.1 Introduction

In chemical thermodynamics, the simultaneous use of both theory and experimental data is essential in explaining many various phenomena. Thus this chapter deals with the analysis of the experimental data measured in this study, in conjunction with the models used to describe the aforementioned data. A comparison of the HPVLE data for carbon dioxide + PFC systems found in the open literature, including the data measured in this work, was undertaken. The carbon dioxide dissolution capabilities of the most proficient solvent from the analysis were then compared to those of an industrial solvent. Accurate HPVLE experimental data is dependent on the proper preparation of the equipment, precise calibration of all relevant measuring devices and the use of high purity chemicals. Thus information relating to the purity checks of all utilised chemicals along with their TCD calibration polynomials is also published in this chapter.

7.2 Purity of chemicals

Presented in Table 7-1 is the list of chemicals that were utilised in the experimental work. The list includes the supplier of each chemical; the supplier stated purity and the GC area fractions for each chemical. The GC area fractions serve to verify the supplier stated purity for each chemical. The area fractions were obtained through the integration of GC peaks obtained upon the single injection of pure chemical and treating the peak corresponding to the chemical of interest as a fraction of the total integrated peaks areas.

Table 7-1: Supplier and purities of chemicals used in this study.

Chemical	Supplier	Stated Purity	GC peak area fraction
C_6H_{14}	Sigma-Aldrich	>0.99[a]	0.991
C_8F_{18}	Apollo scientific	>0.99[a]	0.998
$C_5H_4F_8O$	DLD Scientific	>0.99[a]	0.995
C_7F_{16}	Synquest Labs	>0.99[a]	0.999
C_9F_{20}	Synquest Labs	>0.99[a]	0.998
CO_2	Afrox	>0.999[b]	0.994

[a] Molar basis

[b] Volumetric basis

Due to the effects of purity on the quality of VLE data, an array of tests was performed to verify beyond any reasonable doubt the supplier stated purity. In this regard, the density and refractive indices of the liquid chemicals were measured and thereafter, the obtained data were compared to literature sources as shown in Table 7-2. The density was measured through the use of the DSA 5000M density and sound velocity meter with an uncertainty of 0.000005 g/ml, whilst the refractive indices of the fluorinated compounds, which are relatively lower were measured using the high accuracy Abbe 60/LR, with an accuracy of 0.00004 RI. The refractive index of the hydrocarbon hexane was measured using an ATAGO refractometer, model Rx - 7000α with an uncertainty of 0.0001 RI. There is however very limited experimental data for the refractive indices of fluorinated compounds in the open literature, and as such no published experimental data was found for the hydrofluoroether, and literatures sources used for perfluorooctane and perfluornonane where obtained from the chemical supplier company Sigma Aldrich, and these did not provide the reference articles, thus the experimental methods used to determine the indices are not known.

Table 7-2: Density and refractive indices for the chemicals used in this study.

	Density (g/ml) at 293.15 K		Refractive index at 293.15 K	
	Exp	Lit	Exp	Lit
C_6H_{14}	0.660	0.660[a]	1.375	1.375[f]
C_8F_{18}	1.766	1.766[b]	1.297	1.3[g]
$C_5H_4F_8O$	1.532	1.532[c]	1.290	-
C_7F_{16}	1.730	1.731[d]	1.261	1.261[d]
C_9F_{20}	1.799	1.799[e]	1.273	1.276[h]

[a] (Smyth and Engel, 1929)
[b] (Mustafaev et al., 1995)
[c] (Murata et al., 2002)
[d] (Oliver et al., 1951)

[e] (Posner and Ministers, 2013)
[f] (Kozma et al., 2005)
[g] (sigma aldrich, 2016b)
[h] (Sigma aldrich, 2016a)

7.3 Calibrations

Calibrations were performed for the temperature probes, pressure transducer, and the gas chromatograph-thermal detector as has already been discussed in Chapter 5. The mathematical formulae used in the correlation of the calibration data and the resulting charts for the temperature and pressure measuring devices are published in Appendix A. However, detail on the calibration of the GC thermal detector is published in this chapter, as the procedure used deviated slightly from the norm. The determination of the uncertainties for all the measured variables was achieved through the use of the method outlined by the National Institute of Standards and Technology (NIST) in conjunction with the instructions formulated by Soo (2011) and Nelson (2012), which were specific to VLE measurements.

Composition

The initial calibration polynomials for the thermal detector which were generated for each chemical species and achieved via direct injection were not capable of covering the mole fraction range of the sampled data. Thus mixtures of each component with a compatible solvent/gas were made, in a bid to inject smaller amounts of the required component into the GC, resulting in calibration polynomials which cover a wide mole fraction range. The generation of multiple calibration polynomials from injecting pure components as well as mixtures could be useful in one of two ways:

❖ Allow for the accurate calculation of the errors obtained when only one polynomial is extrapolated below or above its calibration range.

❖ Allow for the use of different polynomials in the calculation of mole fractions from the samples, depending on the range each polynomial covers.

In this study, the first option was utilised as it was noted to be the most efficient. Thus data from the calibration polynomial obtained through the direct injection of pure components were compared to those generated by injecting mixtures, and the deviation of the pure component calibration from the mixture calibration was noted. This error was then used appropriately in the calculation of compositional uncertainty for the data points which had GC peak areas that were below the pure component calibration range. The linear plots of the calibration polynomials, as well as the plots depicting the errors induced by the aforementioned polynomials, are displayed in the following section.

Carbon dioxide

GC calibrations for carbon dioxide were undertaken via the direct injection of the pure component as well as the injection of a carbon dioxide + helium mixture. The errors induced by the calibration polynomials on the number of moles did not exceed 1% for both scenarios.
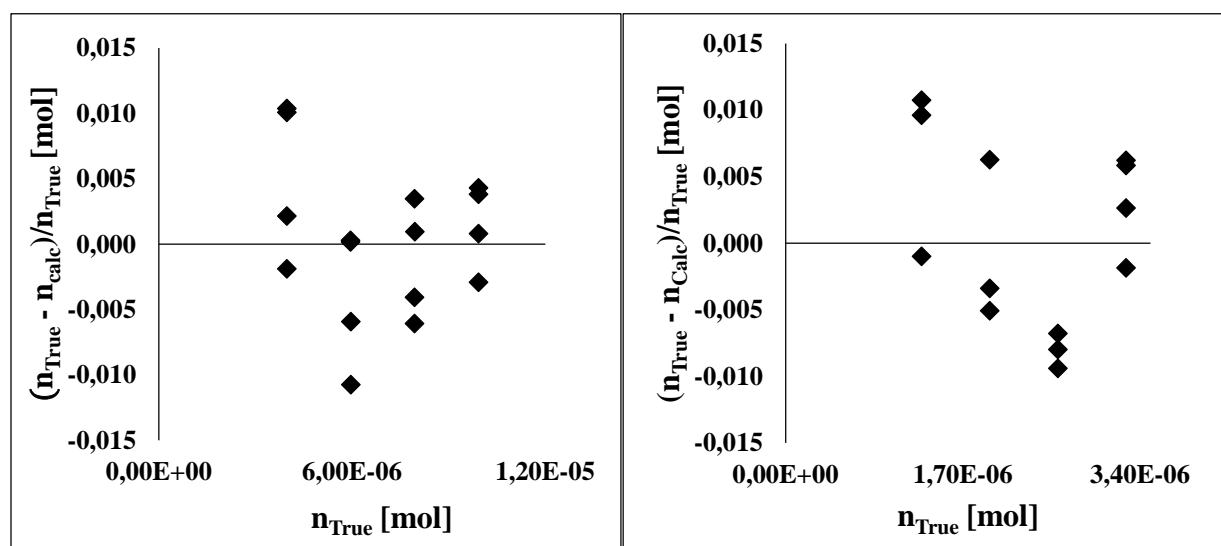
Figure 7-1: Deviation plots for true and calculated carbon dioxide number of moles, **(Left)** injection of pure carbon dioxide, **(Right)** injection of a carbon dioxide helium mixture.
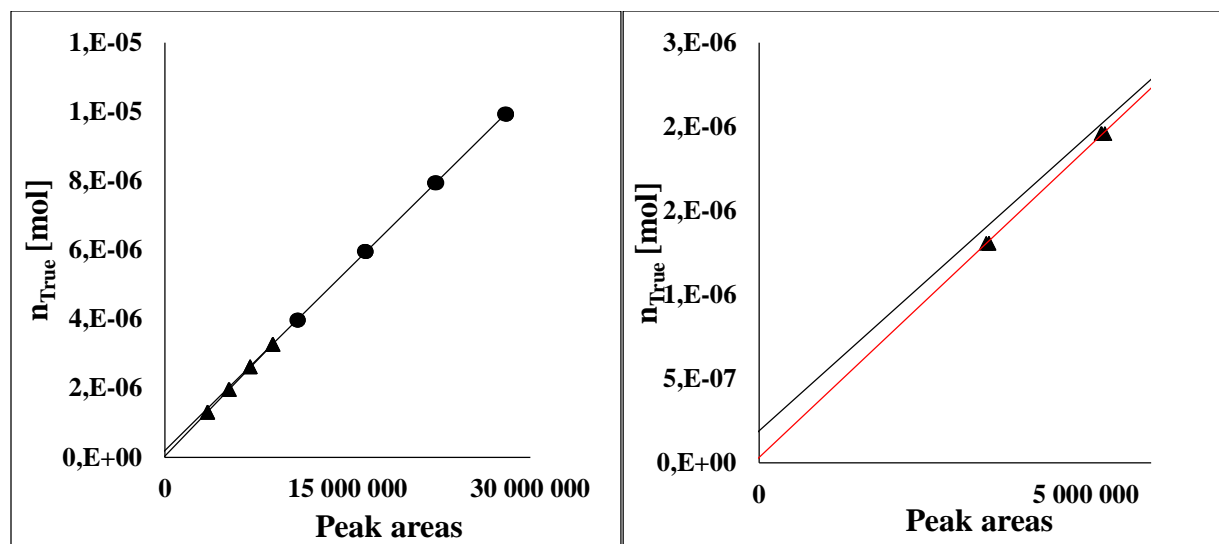
Figure 7-2: GC calibration plots for carbon dioxide via direct injection from a 250µL syringe, (●) pure carbon dioxide, (▲) carbon dioxide + helium mixture. **(Left)** The superimposed plot for the two calibrations, **(Right)** The expanded plot. (—) mixture calibration polynomial, (—) pure component calibration polynomial.

Figure 7-2 indicates the deviation obtained when the pure carbon dioxide calibration equation is used to extrapolate for moles in the low peak area range. Comparison of the two calibration equations indicated that the pure carbon dioxide calibration polynomial could be effectively extrapolated to the lower peak area regions at an error of approximately 4%. The value for this discrepancy was obtained by first multiplying the G.C peak areas of the pure component calibration with the gradients of both the pure component and mixture calibration equations, resulting in two sets of mole values. Thereafter the percentage error between the two sets of values was computed. The same procedure was used for all the other components were extrapolation of the calibration polynomial was necessary. A sample calculation for this procedure is published in Appendix B.

1,1,2,2-tetrafluoroethyl 2,2,3,3-tetrafluoropropyl ether.

Calibration for the hydrofluoroether was undertaken for only the pure compound without the employment of any mixtures because for this particular system; the pure component calibration was deemed sufficient, as the linear plot passed through the origin.
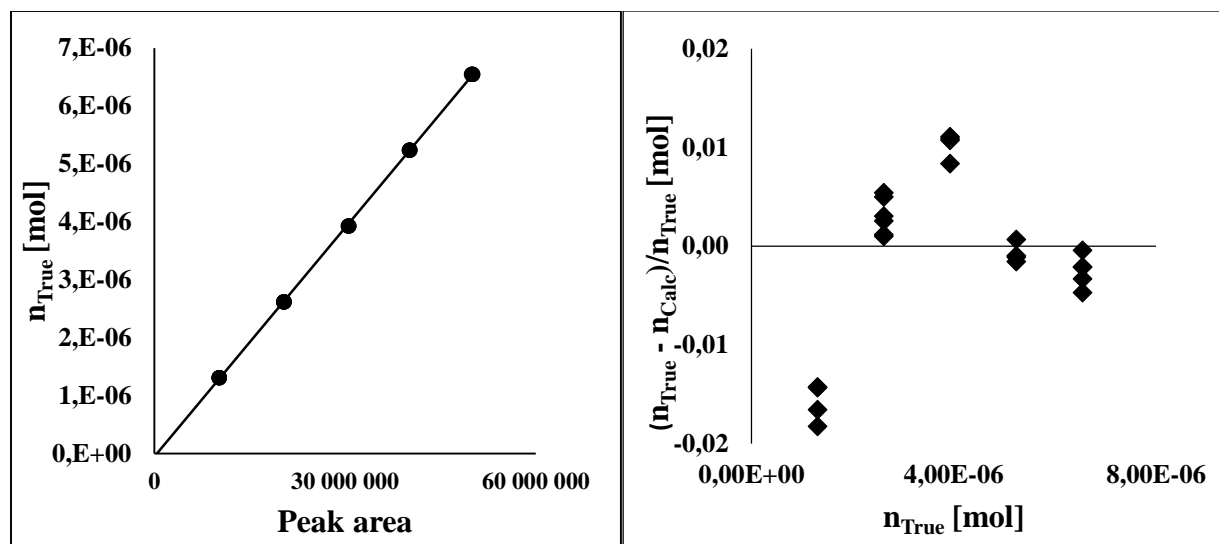
Figure 7-3: Calibration plots for 1,1,2,2-tetrafluoroethyl-2,2,3,3-tetrafluoropropyl ether. (**Left**), Linear calibration plot (**Right**) Deviation plot of true and calculated 1,1,2,2-Tetrafluoroethyl 2,2,3,3-tetrafluoropropyl ether number of moles.

The deviations in the calibration of the fluorinated ether did not exceed 2% and were thus deemed acceptable.

Perfluorocarbons

In order to effectively extrapolate data using the generated calibration polynomials for the perfluoroheptane and perfluorononane, mixtures of each PFC with pentane and hexane (respectively) were formulated, and these were utilised in the same manner as highlighted for carbon dioxide above. The rationale behind the selection of the two hydrocarbons was discussed in Chapter 5.
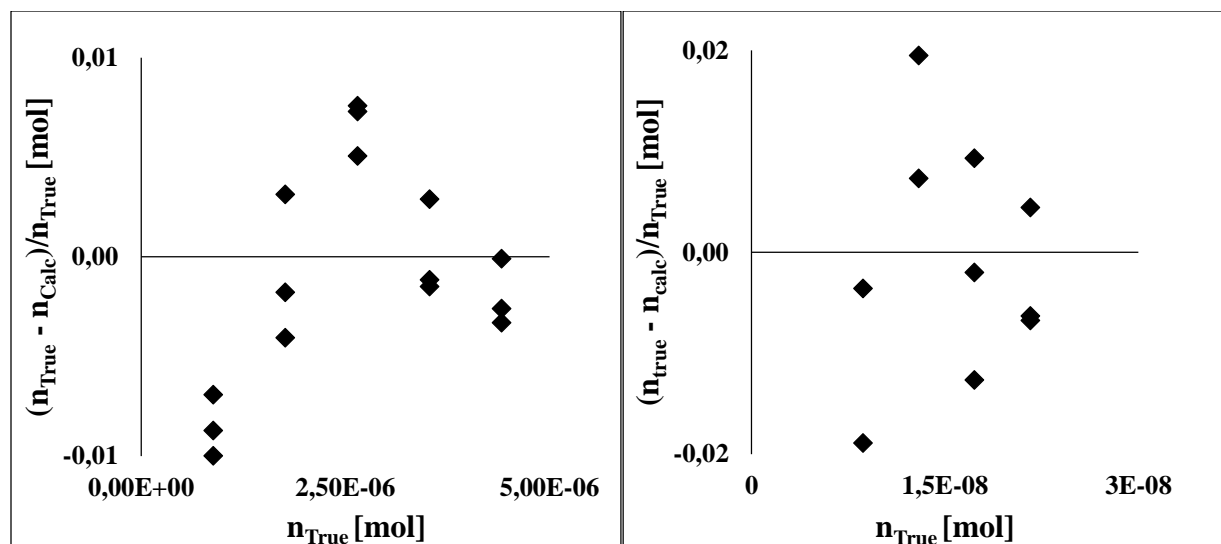
Figure 7-4: Deviation plots for true and calculated perfluoroheptane number of moles, **(Left)** injection of pure perfluroheptane, **(Right)** injection of a perfluoroheptane + pentane mixture.
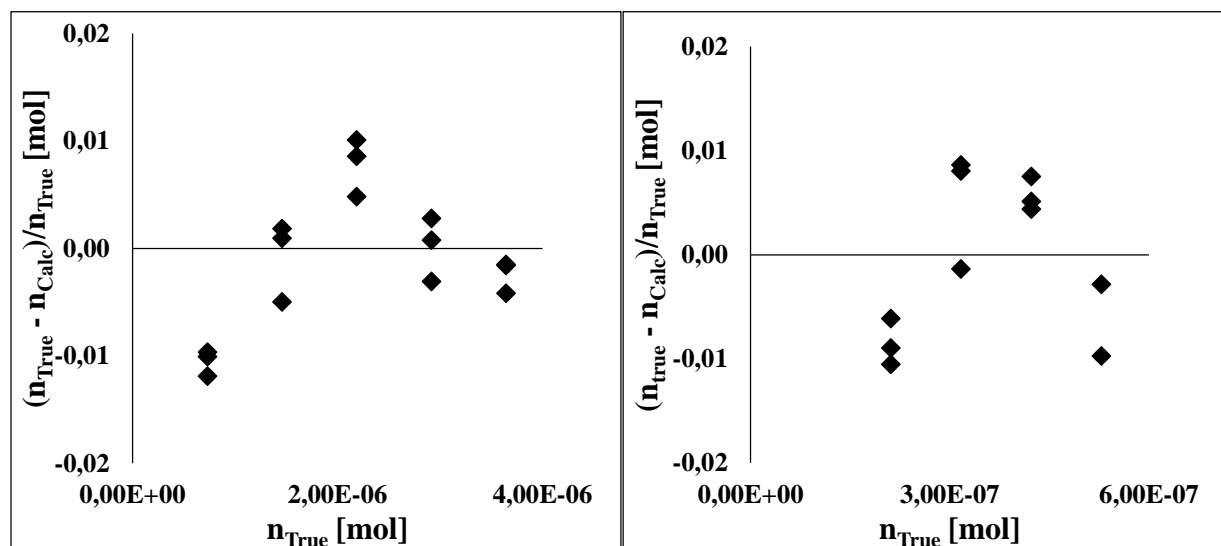
Figure 7-5: Deviation plots for true and calculated perfluorononane number of moles, **(Left)** injection of pure perfluoronnane, **(Right)** injection of a perfluorononane + hexane mixture.

The errors induced by the calibration polynomials for both PFCs were well below 2%. For both PFCs the pure component calibration polynomial was used for sample analyses, and the errors which were incurred during extrapolation for the perfluoroheptane and perfluorononane were 3% and 2% respectively.
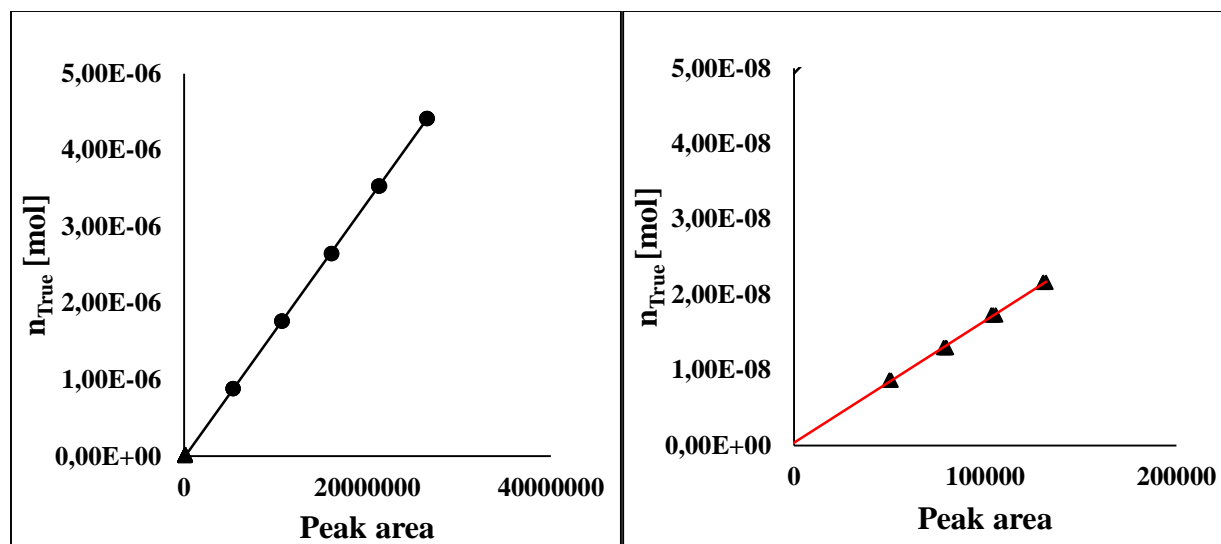
Figure 7-6: GC calibration plots for perfluoroheptane via direct injection from a 250µL syringe, (●) pure perfluoroheptane, (▲) perflurheptane + pentane mixture. **(Left)** The superimposed plot for the two calibrations. **(right)** The expanded plot, (—) mixture calibration polynomial, (—) pure component calibration polynomial.
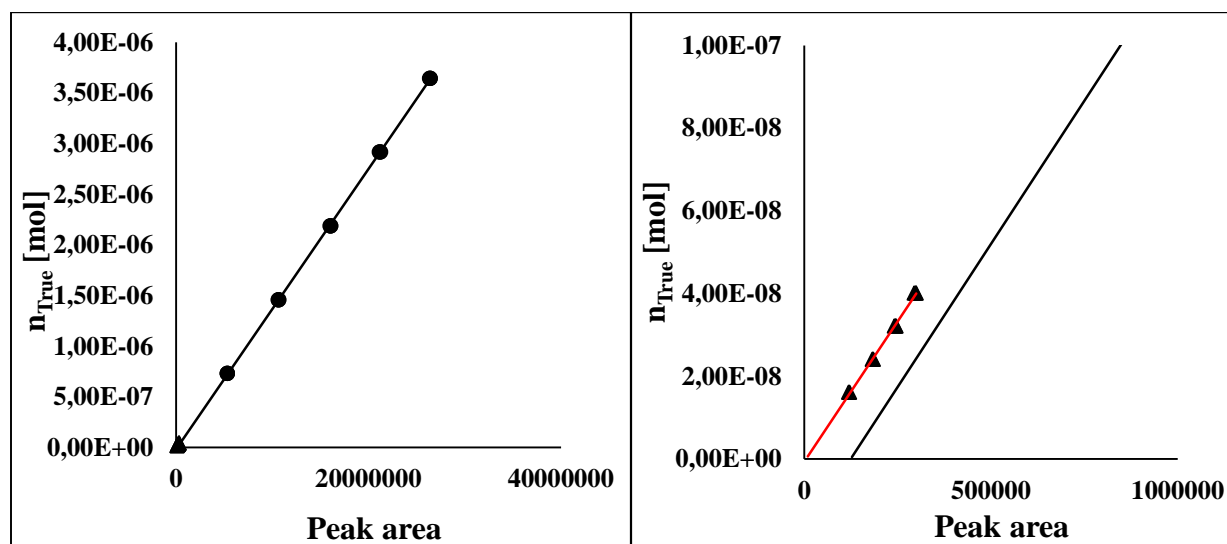
Figure 7-7: GC calibration plots for perfluorononane via direct injection from a 250µL syringe, (●) pure perfluorononane, (▲) perflurononane + hexane mixture. **(Left)** The superimposed plot for the two calibrations. **(Right)** The expanded plot, (—) mixture calibration polynomial, (—) pure component calibration polynomial.

The expanded plots displayed on Figures 7-6 and 7-7 highlight that the pure component and mixture calibration polynomials had near identical slopes, which further indicates that

extrapolation of the pure component calibration to the lower peak area ranges could be effectively performed.

7.4 Vapour pressures

As a means to further affirm the purity of the chemicals utilised as well as the temperature and pressure calibrations, pure component vapour pressures were measured. These measurements were performed for only carbon dioxide and 1,1,2,2-tetrafluoroethyl 2,2,3,3-tetrafluoropropyl ether. Perfluoroheptane and perfluorononane were exempt from these measurements due to the low quantities of chemical available to the research unit's disposal at the time. The NIST Thermo-Data Engine (TDE) which is a component of Aspen Plus V 8.4 was used as a reliable databank for peer-reviewed experimental data. The TDE is used as an evaluation and prediction tool and provides accurate thermophysical properties which are currently available for pure fluids and their mixtures (Nelson, 2012).

The experimental vapour pressure data were correlated using the Peng-Robinson equation of state incorporating the Mathias–Copeman alpha function (PR-MC). The Mathias–Copeman parameters were regressed for all components using the Peng –Robinson equation of state with Wong Sandler mixing rules.

In order to make a sufficient comparison between the experimental and modelled data, sound statistical correlations are imperative. In this regard, the average absolute deviation (AAD), average absolute relative deviation (AARD) and Bias are utilised. The AAD is defined as:

$$AAD_{\hat{U}} = \frac{1}{N} \sum_{i=1}^{N} \left| \hat{U}_{exp} - \hat{U}_{cal} \right| \tag{7-10}$$

Where $\hat{U}_{exp}$ and $\hat{U}_{cal}$ are the experimental and calculated /reference values and N is the total number of data points. The relative deviation is defined as:

$$RD_{\hat{U}} = \left| \frac{\hat{U}_{exp} - \hat{U}_{cal}}{\hat{U}_{exp}} \right| \tag{7-11}$$

The AARD and Bias are defined as follows:

$$AARD_{\hat{U}} \, (\%) = \frac{100}{N} \sum_{i=1}^{N} \left| \frac{\hat{U}_{exp} - \hat{U}_{cal}}{\hat{U}_{exp}} \right| \tag{7-12}$$

$$BIAS_{\hat{U}} \, (\%) = \frac{100}{N} \sum_{i=1}^{N} \frac{\hat{U}_{exp} - \hat{U}_{cal}}{\hat{U}_{exp}} \tag{7-13}$$

Experimental and modelled vapour pressure data for carbon dioxide and 1,1,2,2-tetrafluoroethyl 2,2,3,3-tetrafluoropropyl ether are tabulated in Tables 7-3 and 7-4 and the linear plots generated from the data are shown in Figure 7-8. The plots depict experimental data, data modelled through the use of the PR-MC-EoS and the reference data obtained from the NIST Thermo-data engine.

Table 7-3: Vapour pressure data for carbon dioxide.

Experimental		PR-MC	
P[MPa]	**T [K]**	**P[MPa]**	**$P_{exp} - P_{cal}$**
3.036	268.09	3.036	0.000
3.383	272.08	3.383	0.000
3.757	276.07	3.757	0.000
4.161	280.05	4.161	0.000
4.596	284.05	4.596	0.000
5.065	288.04	5.065	0.000
5.570	292.03	5.570	0.000
6.116	296.03	6.116	0.000
6.703	300.03	6.704	0.001

Expanded uncertainties (U) calculated with k = 2. $U_{(T)}$ = 0.04 K, $U_{(P)}$ = 0.007 MPa.

Table 7-4: Vapour pressure data for 1,1,2,2-tetrafluoroethyl 2,2,3,3-tetrafluoropropyl ether.

Experimental		PR-MC	
P[MPa]	T [K]	P[MPa]	$P_{exp} - P_{cal}$
0.001	273.15	0.001	0.000
0.004	293.12	0.004	0.000
0.006	298.14	0.006	0.000
0.007	303.18	0.007	0.000
0.012	313.14	0.012	0.000
0.020	323.14	0.020	0.000

Expanded uncertainties (U) calculated with k = 2. $\mathbf{U_{(T)}}$ = 0.04 K, $\mathbf{U_{(P)}}$ = 0.007 MPa.
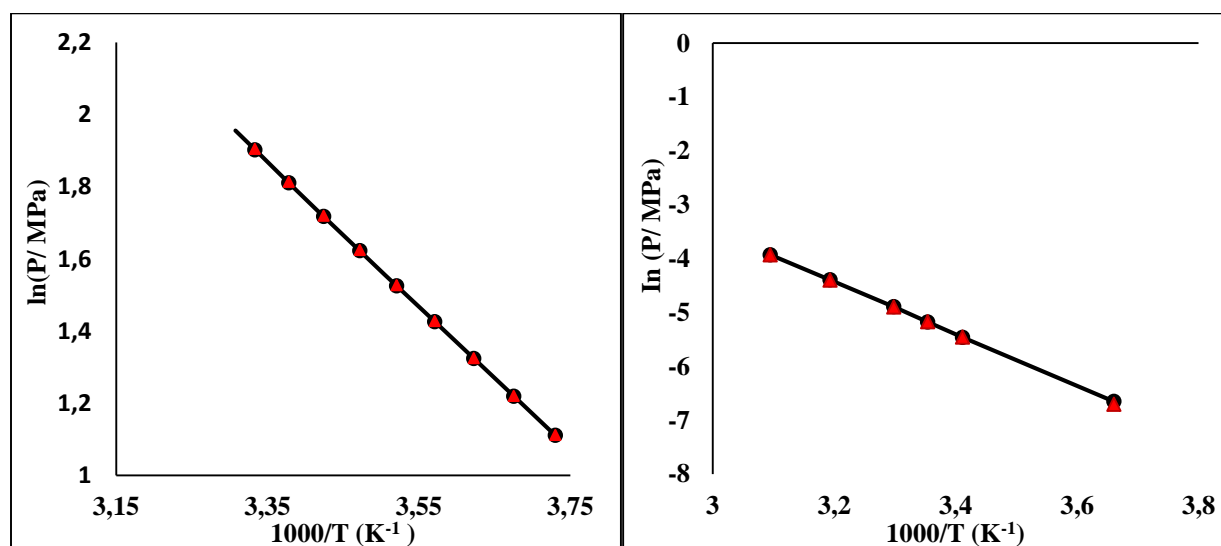
Figure 7-8: Vapour pressure Data for (**Left**) carbon dioxide, (**Right**) 1,1,2,2 tetrafluoroethyl 2,2,3,3-tetrafluoropropyl ether. (●) Exp data, (▲) NIST TDE, (—) PR-MC EoS.

The linear relationship between the natural logarithm of the vapour pressure and the reciprocal for temperature highlights the lack thereof of any decomposition or polymerisation of components during measurements. The AAD, AARD, and Bias for the vapour pressures are tabulated in Table 7-5. The AARD and the Bias for the regressed experimental data are both below 1%.

Table 7-5: Absolute average relative deviations (AARD), Average absolute deviation (AAD) and Bias for the vapour pressure data.

Component	AAD/MPa		AARD%		BIAS%	
	PR-MC	NIST	PR-MC	NIST	PR-MC	NIST
CO_2	0.0004	0.096	0.0009	0.194	-0.0001	-0.194
$C_5H_4F_8O$	0.000002	0.000476	0.0061	0.912	0.912	1.312

$AAD = 1/N \sum |P_{Exp} - P_{ref}|$, where P_{Exp} and P_{ref} represent the experimental and the regressed/ NIST vapour pressures respectively.

$AARD\% = 100/N \sum \left| {P_{Exp} - P_{ref}}/{P_{Exp}} \right|$, N is the total number of data points.

$BIAS\% = 100/N \sum {P_{Exp} - P_{ref}}/{P_{Exp}}$

The regression of the vapour pressures was done in order to generate the Mathias-Copeman parameters which were then fitted to the Peng-Robinson equation of state through the use of the least squares regression algorithm. These parameters are given in Table 7-6, which includes the temperature ranges at which the vapour pressures were measured.

Table 7-6: Mathias –Copeman parameters for the components used in the study.

Component	T [K]	C_1	C_2	C_3
CO_2[a]	273.15 – 303.15	0.725	-0.821	5.475
C_6H_{14}[b,1]	273.15 – 303.13	0.780	0.212	-0.238
C_8F_{18}[b,2]	288.13 -318.17	0.199	8.975	-20.553
$C_5H_4F_8O$[a]	273.15 – 323.15	0.733	3.440	-7.213
C_7F_{16}[b,3]	280 – 325.68	0.896	2.372	-5.545
C_9F_{20}[b,4]	288.18 – 323.15	0.998	1.726	-3.275

[a] Regressed from experimental data.
[b] Regressed from literature data.
[1] (Thomas and Young, 1895)
[2] (Dias et al., 2004)
[3] (Oliver and Grisard, 1951)
[4] (Dias et al., 2005)

7.5 Vapour-liquid equilibrium test system measurements and modelling.

The culmination of the work done in this project resulted in the measurement of five binary systems, which were further categorised as two test systems and three novel systems, namely:

Test systems: $[CO_2 \; (1) + C_6H_{14} \; (2)]$, $[CO_2 \; (1) + C_8F_{18} \; (2)]$,

New systems: $[CO_2 \; (1) + C_5H_4F_8O(2)]$, $[CO_2 \; (1) + C_7F_{16} \; (2)]$, $[CO_2 \; (1) + C_9F_{20} \; (2)]$

The numbers (1) and (2) after each component denotes the lighter and heavier component respectively.

The hexane and perfluorooctane test systems were measured at 313.15 K and 293.15 K respectively, while the novel measurements were conducted at three isotherms (273.15 K, 293.15 K and 313.15 K) for each binary pair. Test system measurements were performed to ascertain the performance of the equipment and also allow the experimenter to develop a sound technique which incorporated the ability to use the least amount of chemical possible, which is in itself a challenging task. The use of relatively small amounts (approx. 20 ml per binary system) of the fluorinated compounds in the experimental work was paramount due to the high cost of the chemicals. The results from each test system were compared to data from reputable literature sources.

All experimental VLE data in the study were correlated via the modern direct method using a combination of two thermodynamic models, namely the Peng-Robinson equation of state incorporating the Mathias-Copeman alpha function, with the Wong-Sandler mixing rules, in conjunction with the non-random two liquid activity coefficient model (NRTL) and the Peng–Robinson EoS with classical mixing rules. The software package Aspen Plus V 8.4 was utilised for the regression of all experimental data in this work. The selection criterion for these models was based on their prior performance in modelling systems comprising of fluorinated chemicals (Coquelet and Richon, 2009; Tshibangu et al., 2014; Bengesai et al., 2016) and the rationale which was explained in Chapter 6.

For the novel measurements, each constituent isotherm was first correlated individually for the purpose of thermodynamic consistency testing. Simultaneous correlation of all isotherms in each binary system was also undertaken in order to compare the generated model parameters from the two scenarios. The purpose of the comparison was to indicate whether temperature dependence could be effectively implemented into the NRTL activity coefficient model(Nelson, 2012).

7.5.1   Carbon dioxide (1) + hexane (2):1st test system

Table 7-7: Experimental and regressed VLE data for carbon dioxide (1) + hexane (2).

Experimental			PR-MC-WS-NRTL			Expanded Uncertainties	
P[MPa]	x_1	y_1	P[MPa]	y_1	$y_{calc} - y_{exp}$	$U_{(x_1)}$	$U_{(y_1)}$
T = 313.12 K							
7.046	0.8865	0.9817	7.161	0.9803	-0.00132	0.0045	0.0007
6.551	0.8102	0.9822	6.602	0.9808	-0.00135	0.0068	0.0007
6.037	0.7252	0.9831	6.041	0.9813	-0.00175	0.0089	0.0007
5.427	0.6270	0.9835	5.396	0.9818	-0.00178	0.0104	0.0007
4.837	0.5433	0.9832	4.814	0.9819	-0.00133	0.0110	0.0007
4.074	0.4466	0.9824	4.085	0.9815	-0.00083	0.0111	0.0007
3.732	0.3976	0.9826	3.690	0.9810	-0.00153	0.0107	0.0007
3.124	0.3275	0.9819	3.096	0.9797	-0.00217	0.0098	0.0007
2.148	0.2256	0.9760	2.182	0.9754	-0.00061	0.0078	0.0018
1.367	0.1414	0.9659	1.393	0.9659	0.00002	0.0054	0.0014
0.931	0.0953	0.9545	0.953	0.9534	0.04253	0.0038	0.0019
0.486	0.0447	0.9109	0.468	0.9803	-0.00132	0.0019	0.0036

Expanded uncertainties (U) calculated with k = 2. $U_{(T)}$ = 0.04 K, $U_{(P)}$ = 0.007 MPa, $U_{(x)}$ = 0.0111, $U_{(y)}$ = 0.0036.
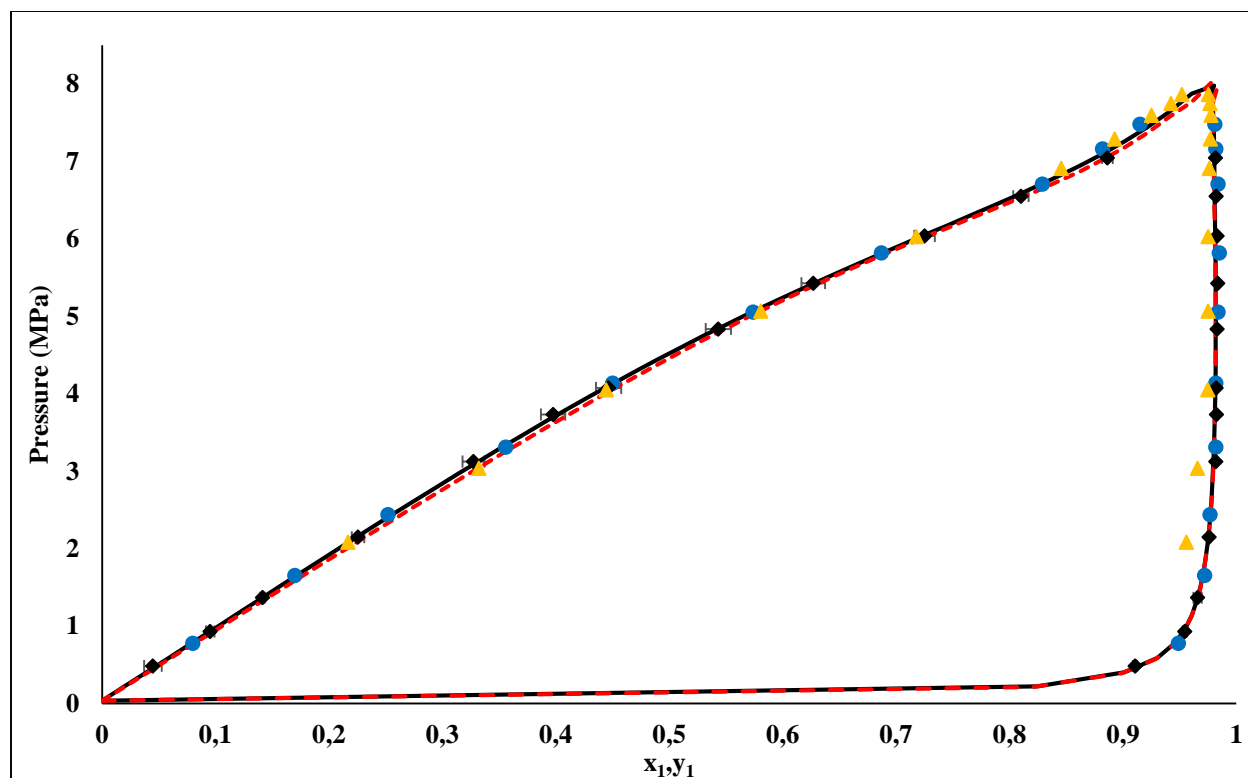
Figure 7-9: P-xy data for the carbon dioxide (1) + hexane (2) system at 313.12 K. (◆) Exp data, (●) Li et al. (1981), (▲) Wagner and Wichterle (1987), (—) PR-MC-WS-NRTL model, (-----) PSRK.

The experimental data presented above showed good agreement with the PR-MC-WS-NRTL model and also compared exceptionally well with the data measured by Li et al. (1981) and Wagner and Wichterle (1987), particularly in the liquid phase. In the vapour phase however, the data from Wagner and Wichterle (1987) displayed substantial deviation from the other three data sources, thus its use in further comparisons was not undertaken. The experimental data sets were obtained through the use of different measurement techniques. Li et al. (1981) utilised a static synthetic apparatus which had a variable volume cell at the core of its construction. The sampling technique which was employed in this reference study utilised a heated sample valve, which was developed by Yarborough and Vogel (1967), in conjunction with a gas chromatograph for analysis purposes. The P-xy trend for the data generated in this study produced a smooth profile when compared to the phase envelope of the reference data from Li et al., and the slight discrepancy was expected to be due to the different sampling techniques employed in the two studies. The purities for the carbon dioxide and hexane utilised in the measurement of the experimental and reference data were > 99 vol/mol %.
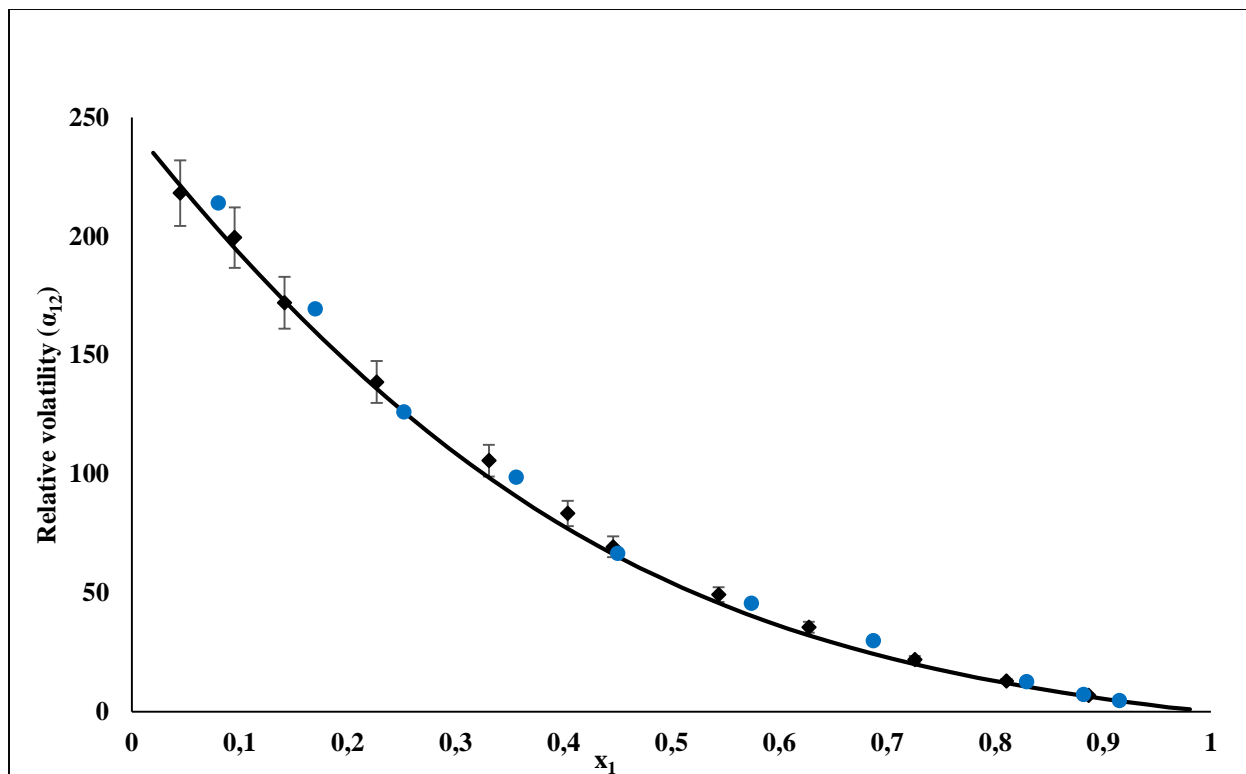
Figure 7-10: Plot of relative volatility (α_{12}) as a function of liquid composition (x_1) for the carbon dioxide (1) + hexane (2) system. (◆) Exp data, (●) Li et al. (1981), (—) PR-MC-WS-NRTL model.

Figure 7-10 highlights the relationship of composition with relative volatility. The experimental data present a good fit with the model. The reference data deviates slightly at low carbon dioxide mole fractions in a similar manner as was highlighted in Figure 7-9. Relative deviations and bias for the pressure and vapour composition for this system are shown in Table 7-8.

Table 7-8: Error analysis for the carbon dioxide (1) + hexane (2) system.

Summary statistic	Pressure	Vapour composition (y_1)
AARD (%)	0.487	0.542
AAD	0.022 MPa	0.0005
BIAS (%)	0.111	-0.117

The AARD and the Bias are both well below 1%, which signifies an excellent agreement between the experimental and modelled data. The parameters for the PR-MC-WS-NRTL model which were generated through the regression of the experimental data are shown in Table 7-9.

Table 7-9: Model parameters for the carbon dioxide (1) + hexane (2) system.

Isotherm [K]	$b_{ij}{}^a$[K]	$b_{ji}{}^a$[K]	$k_{ij}{}^b$
313.12	-303.321	8395.902	0.545

[a]Scalar NRTL model parameters, $\tau_{ij} = {b_{ij}}/{T}$, $\alpha_{ij} = 0.3$.

[b] Scalar WS mixing rule parameter (k_{ij}) incorporated into the Peng-Robinson EoS.

7.5.2   Carbon dioxide (1) + perfluorooctane (2): 2nd test system

Since the purpose of the study was focused on the interaction of carbon dioxide with fluorinated compounds, the binary combination of carbon dioxide and perfluorooctane was an ideal choice for test system measurement. Only one data set was available in the open literature for comparison purposes, and this was measured by Dias et al. (2006), through the use of a technique that was based on the synthetic method. The experimental data for this system was measured at 293.12 K. The reference data was measured via an apparatus that made use of a variable volume high-pressure cell, which consisted of a hollow, horizontal stainless steel cylinder, with a movable piston and sapphire window on either end. The binary mixture was prepared within the cell via loading known amounts of the liquid and gas components respectively. Sampling of either phase was not required, and as such, the fluid phase boundary between the liquid and vapour phase was obtained through the measurement of the pressure when the vapour phase disappeared. The phase disappearance was observed through the installed sapphire window. The equilibrium phase behaviour in the reference data was described using the soft-statistical associating fluid theory (soft-SAFT) EoS. Pressure and temperature uncertainties in the work of Dias et al. (2006) were reported to be 0.02 MPa and 0.01 K respectively. However, the uncertainty in the composition of the liquid phase was not reported. The purities of the chemicals used in the reference data were (>99.9 vol %) for carbon dioxide and (98 mol %) for the PFC. The carbon dioxide and perflurooctane used in this work had purities of (>99 vol %) and (99 mol %) respectively. The expanded uncertainties in composition for the experimental data measured through the use of the static analytic apparatus where $U(x_1) = 0.011$ mol fraction and $U(y_1) = 0.0004$ mol fraction, while the uncertainty in the liquid phase for the data measured via the static synthetic apparatus with a variable volume cell which was used in this work was $U(x_1) = 0.014$ mol fraction. The

experimental and regressed data for the system, including expanded uncertainties for each point are tabulated in Table 7-10.

Table 7-10: Experimental and regressed VLE data for carbon dioxide (1) + perfluorooctane (2).

Experimental			PR-MC-WS-NRTL			Expanded Uncertainties	
P[MPa]	x_1	y_1	P[MPa]	y_1	$y_{calc} - y_{exp}$	$U_{(x_1)}$	$U_{(y_1)}$
T = 293.12 K							
4.892	0.8951	0.9986	4.945	0.9983	-0.0002	0.0043	0.0001
4.163	0.7644	0.9982	4.113	0.9981	-0.0001	0.0084	0.0001
3.712	0.6899	0.9978	3.664	0.9980	0.0002	0.0097	0.0001
3.090	0.5851	0.9977	3.077	0.9979	0.0002	0.0110	0.0001
2.373	0.4536	0.9974	2.375	0.9977	0.0003	0.0113	0.0001
1.865	0.3621	0.9970	1.891	0.9975	0.0005	0.0105	0.0001
1.460	0.2821	0.9964	1.467	0.9971	0.0007	0.0092	0.0001
1.206	0.2359	0.9959	1.222	0.9967	0.0008	0.0082	0.0002
0.780	0.1503	0.9941	0.773	0.9954	0.0013	0.0058	0.0002
0.401	0.0774	0.9897	0.396	0.9919	0.0021	0.0032	0.0004

Expanded uncertainties (U) calculated with k = 2. $U_{(T)}$ = 0.04 K, $U_{(P)}$ = 0.007 MPa, $U_{(x)}$ = 0.0113, $U_{(y)}$ = 0.0004.
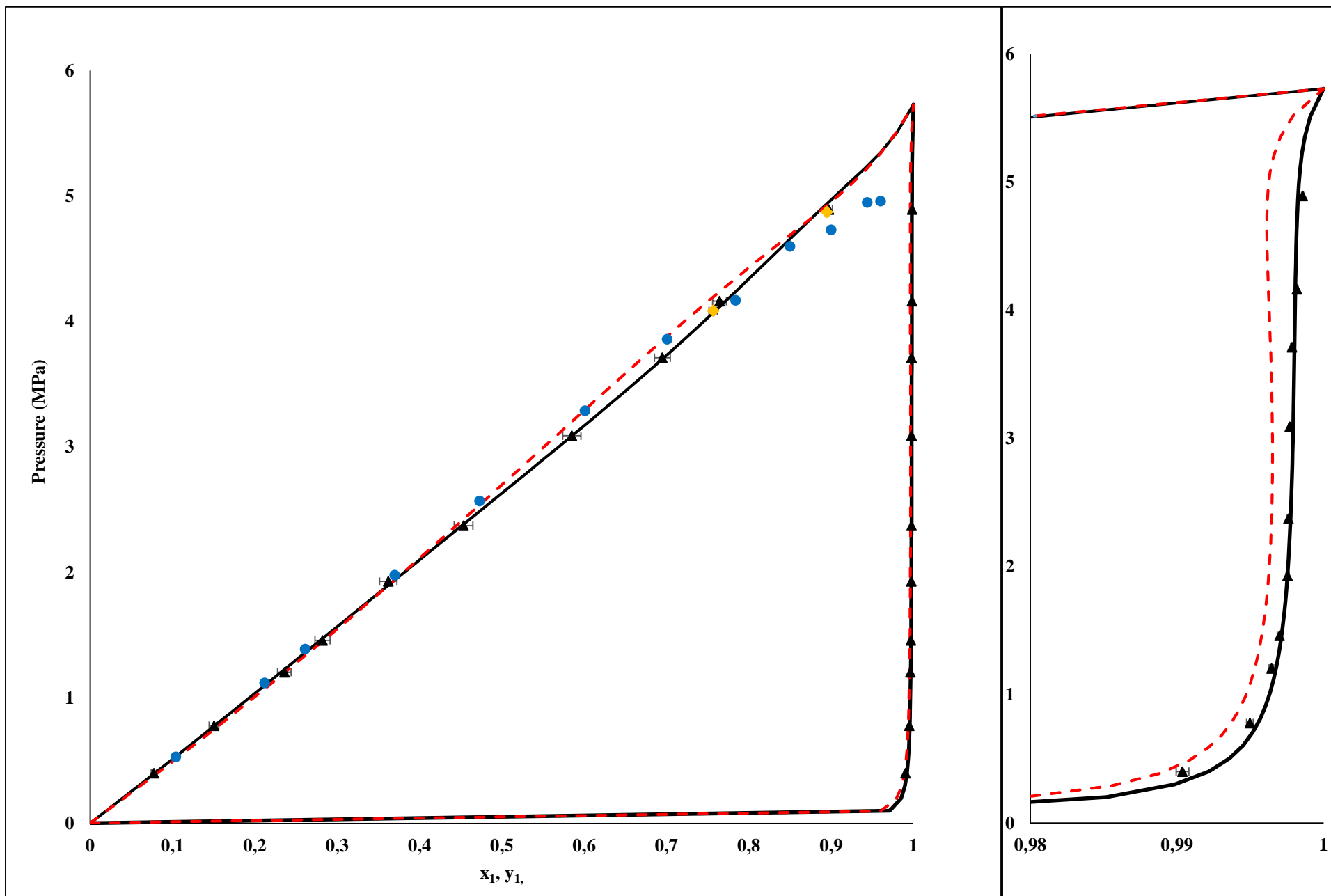
Figure 7-11: P-xy data for the carbon dioxide (1) + perfluorooctane (2) binary system measured at 293.12 K. (▲) Exp data, this work with a static analytic apparatus. (●) (Dias et al., 2006). (◆) Exp data, this work with a static synthetic apparatus with a variable volume cell. (—) PR–MC–WS-NRTL model, (-----) Peng-Robinson EoS model.

The phase equilibrium data from this system was modelled using the Peng-Robinson EoS with classical mixing rules as well as the PR-MC-WS-NRTL model, in a bid to note the model which best represents the data. Figure 7-11 shows the experimental and reference data in conjunction with the two models. The reference data deviates from the PR-MC-WS-NRTL model from (x_1 > 0.5) and begins to scatter as the mole composition of the lighter component increases. The cause of the scatter in the data could have been due to the presence of air within the cell prior to the loading of the lighter component as well as leaks from the equipment. The same technique employed by Dias et al. (2006) was used in this work to measure only two points, in order to clarify the discrepancy between the experimental and reference data. The primary difference between the two techniques was in the loading procedures. The charging procedure used for the reference data commenced with loading known amounts of the liquid component via vacuum extraction but did not seem to take into account the possible presence of air within the cell before loading the liquid. The loading procedure used in this work was discussed in Chapter 5, where careful attention is paid to ensure that no air is present within the cell prior to loading the liquid component. The two points measured with the variable volume cell in this work matched perfectly (within the uncertainty) with the data measured via the static analytic apparatus.

In Figure 7-11, it can be seen that the Peng-Robinson EoS model fails to represent the experimental data effectively and is seen to overestimate the bubble pressure curve, by a maximum magnitude of approximately 4.1% at a pressure of 3.7 MPa. The PR-MC-WS-NRTL model, on the other hand, correlates the experimental data (within uncertainty) in the liquid phase very well. The model also presents a relatively good fit in the vapour phase, with the exception of the slight deviations at pressures below 1 MPa. These deviations were possibly caused by the condensation of the heavy perfluorocarbon on the ROLSI™ capillary tip due to the low pressures. Both models converge at pressures above 5 MPa, forming a shape that closely resembles a bird's beak as both the bubble and dew curves become horizontal as discussed by (Rainwater, 2001).
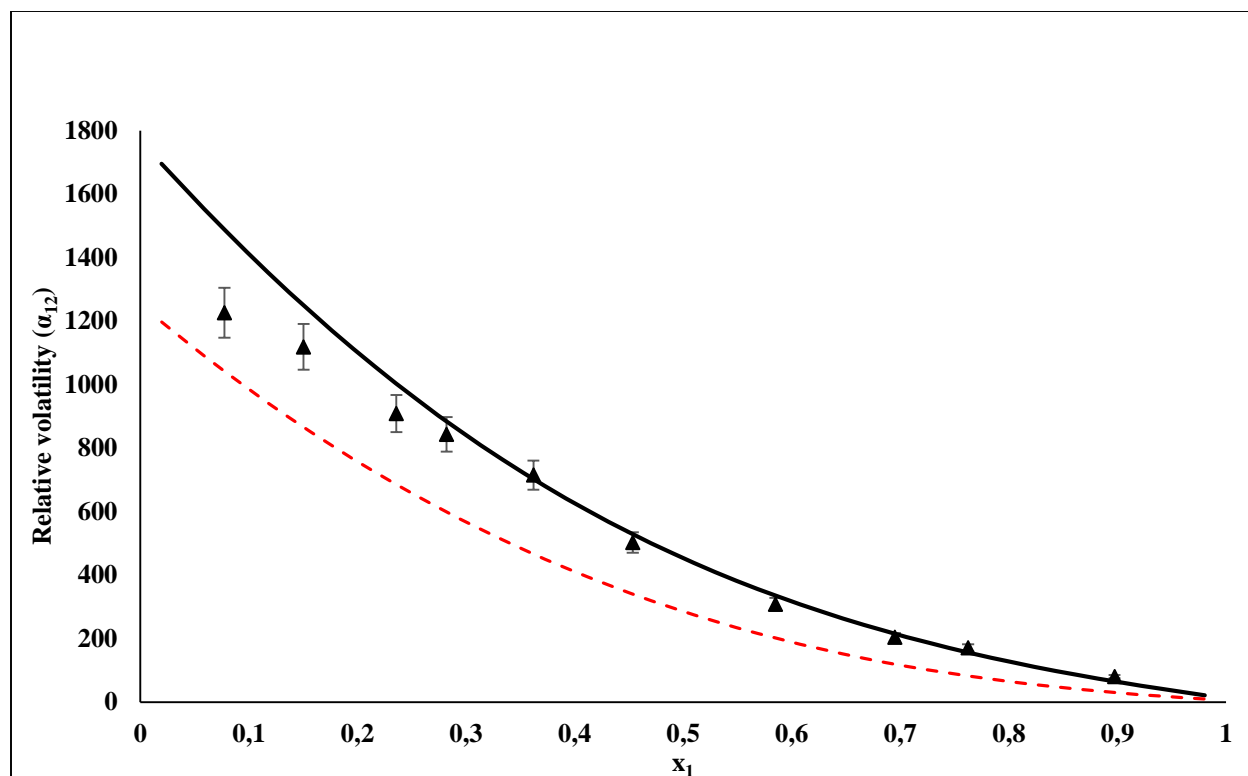
Figure 7-12: Relative volatility (α_{12}) as a function of the liquid composition (x_1), (▲) Exp data, (—) PR-MC-WS-NRTL model, (-----) Peng-Robinson EoS model.

Figure 7-12 shows that the relative volatilities for the experimental data become less consistent with the model data at ($x_1 < 0.3$), which is similar to what was observed in the P-xy plot. The deviations at low pressure were substantially above the uncertainty for all the three points in the region. The relative deviations AARD, AAD, and Bias for the pressure and vapour composition for both models are tabulated in Table 7-11:

Table 7-11: Error analysis for the carbon dioxide (1) + perfluorooctane (2) system

MODEL	$\mathbf{AARD_p}$ (%)	$\mathbf{BIAS_p}$(%)	$\mathbf{AAD_p}$(MPa)	$\mathbf{AARD_{y_1}}$(%)	$\mathbf{BIAS_{y_1}}$(%)	$\mathbf{AAD_{y_1}}$
PR-MC-WS-NRTL	0.952	-0.005	0.022	0.037	0.058	0.0003
PR-EoS	2.344	0.101	0.051	0.015	-0.150	0.001

The relative deviations for the PR-MC-WS-NRTL model were all substantially below 1%, while the Peng-Robinson EoS resulted in a relative deviation in pressure which was above 2%. The PR-MC-WS-NRTL model provided an excellent description of the bubble curve relative to the Peng-Robinson EoS. The generated parameters of the two models are displayed in Table 7-12.

Table 7-12: Model parameters for the carbon dioxide (1) + Perflurooctane (2) system.

Model	$b_{ij}{}^a$ [K]	$b_{ji}{}^a$ [K]	k_{ij}
PR-MC-WS-NRTL	999.832	429.713	0.713[b]
PR-EoS	-	-	0.071

[a]Scalar NRTL model parameters, $\tau_{ij} = {}^{b_{ij}}\!/_T$, $\alpha_{ij} = 0.3$.
[b] Scalar WS mixing rule parameter (k_{ij}) incorporated into the Peng-Robinson Eos.

The data for the two binary test systems exhibited good correlation with the PR-MC-WS-NRTL model, with the carbon dioxide (1) + hexane (2) system displaying excellent agreement with the reference data from Li et al. The experimental data for the carbon dioxide (1) + perflurooctane (2) system deviated from the reference source however the data was validated by the PR-MC-WS-NRTL model, which described the data well within the uncertainty reported for the liquid phase composition. A static synthetic technique, with a variable volume cell, was also used to further affirm the experimental data from the second test system.

7.6 Novel phase equilibrium measurements

Three novel binary systems were measured in this work, with each pair constituting of carbon dioxide and a fluorinated compound. These measurements formed the core experimental work for the study. The measurements were performed up to maximum pressures of approximately 7.5 MPa for a total of three isotherms per binary system. Measurements were conducted through the use of both the static analytical and static synthetic techniques. However the former was the primary technique, with the latter used in the measurement of a few data points near the equimolar region. The purpose of using two different apparatus which employed different techniques was to validate the experimental data, as discrepancies were noted in the correlation of the vapour phase by the models. Furthermore, HPVLE measurements are inherently difficult to undertake (Raal and

Mühlbauer, 1997; Fonseca et al., 2011), and the use of small amounts of chemicals also compounds the difficulties incurred. Thus a reputable means of affirming the measurements was deemed ideal. The generated experimental data were correlated using the software package Aspen Plus version 8.4.

The expanded uncertainties in composition for the three novel systems are highlighted in Table 7-13. The procedure utilised in the calculation of these uncertainties is discussed in Appendix C. The aforementioned uncertainties are predominantly due to the calibration polynomials, while other factors contribute approximately 1% to the final uncertainty. The uncertainties in the vapour phase for all the three binary systems is very low, which is due to the fact that the vapour phase compositions are highly concentrated with carbon dioxide, which is similar to what was reported by Nelson (2012), in his study of the CO_2/C_5H_{12} binary system. Thus a step by step calculation of the compositional uncertainty in the vapour phase for the CO_2/C_9F_{20} binary system is published in Appendix C, to justify the low values.

Table 7-13: Expanded compositional uncertainties.

	Static analytic		Static synthetic
Binary System	$U_{(x)}$	$U_{(y)}$	$U_{(x)}$
$CO_2/C_5H_4F_8O$	0.018	0.001	0.004
CO_2/C_7F_{16}	0.019	0.003	0.004
CO_2/C_9F_{20}	0.017	0.0003	0.056

7.6.1 Carbon dioxide (1) + 1,1,2,2-tetrafluoroethyl 2,2,3,3-tetrafluoropropyl ether (2)

The VLE data for the above mentioned binary system was measured at three isotherms (273.13 K, 293.16 K, and 313.16 K) using the static analytic apparatus. Measurements with the static synthetic apparatus were conducted at only two isotherms (293.16 K and 313.16 K). Two isotherms were measured below the critical temperature of the lighter component (carbon dioxide) and one isotherm above. The PR-MC-WS-NRTL model and the Peng-Robinson EoS model were both used to correlate the data, with the former providing a satisfactory description of the experimental data, particularly in the liquid phase. Figure 7-13 depicts the P-xy plot for the system, and it can be noted from the plot that the Peng-Robinson EoS model under-estimates the bubble curve, and this phenomenon is seen to escalate as the temperature increases. Both models provided near identical

phase envelopes for all three isotherms, with the sub-critical temperature isotherms forming a shape with a sharp angle at the intersection point of the bubble and dew curves, while the isotherm above the carbon dioxide critical temperature formed a closed loop. The interaction of the two components resulted in the negative deviation from Raoult's law, which is evident from the concave shape of the phase envelopes, as well as the negative values of the binary interaction parameters for the classical mixing rules in each isotherm, which are displayed in Table 7-15. The VLE data for the system, including the regressed data (PR-MC-WS-NRTL model) and the expanded uncertainties of each point are shown in Table 7-14.

Table 7-14: Experimental and regressed VLE data for carbon dioxide (1) + 1,1,2,2-tetrafluoroethyl 2,2,3,3-tetrafluoropropyl (2).

Experimental			PR-MC-WS-NRTL			Expanded Uncertainties	
P[MPa]	x_1	y_1	P[MPa]	y_1	$y_{calc} - y_{exp}$	$U_{(x_1)}$	$U_{(y_1)}$
T = 273.13 K							
3.084	0.931	0.99972	3.153	0.99969	-0.00003	0.005	0.00002
2.778	0.866	0.99954	2.798	0.99949	-0.00005	0.009	0.00003
2.458	0.793	0.99936	2.440	0.99932	-0.00004	0.012	0.00006
2.259	0.743	0.99919	2.222	0.99923	0.00003	0.014	0.00005
2.120	0.718	0.99918	2.115	0.99918	0.00001	0.015	0.00006
1.770	0.631	0.99900	1.779	0.99903	0.00003	0.017	0.00007
1.531	0.560	0.99887	1.525	0.99889	0.00002	0.018	0.00008
1.253	0.479	0.99864	1.252	0.99870	0.00006	0.018	0.00010
1.003	0.402	0.99841	1.011	0.99845	0.00004	0.018	0.00012
0.815	0.341	0.99818	0.830	0.99817	-0.00001	0.017	0.00013
0.485	0.211	0.99734	0.477	0.99703	-0.00031	0.012	0.00020
T = 293.16 K							
5.171	0.957	0.9993	5.268	0.9994	0.0002	0.003	0.0001
4.604	0.893	0.9990	4.679	0.9990	0.0000	0.007	0.0001
4.091	0.824	0.9989	4.097	0.9988	0.0002	0.011	0.0001
3.507	0.748	0.9985	3.491	0.9985	-0.0006	0.014	0.0001
3.210	0.704	0.9983	3.173	0.9983	-0.0009	0.015	0.0001
2.913	0.669	0.9982	2.933	0.9982	-0.0001	0.016	0.0001
2.558	0.615	0.9979	2.591	0.9980	-0.0002	0.017	0.0002
2.115	0.528	0.9976	2.087	0.9975	0.0001	0.018	0.0002
1.920	0.488	0.9975	1.882	0.9973	0.0001	0.018	0.0002
1.557	0.424	0.9970	1.575	0.9968	-0.0001	0.018	0.0002
1.077	0.311	0.9962	1.098	0.9956	0.0001	0.016	0.0003
0.673	0.193	0.9939	0.669	0.9930	-0.0001	0.011	0.0004
T = 313.16 K							
7.106	0.910	0.9961	7.127	0.9952	-0.001	0.006	0.0003
6.847	0.892	0.9962	6.863	0.9953	-0.001	0.007	0.0003
6.605	0.877	0.9961	6.661	0.9953	-0.001	0.008	0.0003
5.863	0.817	0.9962	5.858	0.9954	-0.001	0.011	0.0003
4.836	0.733	0.9959	4.884	0.9952	-0.001	0.014	0.0003
4.059	0.649	0.9959	4.037	0.9948	-0.001	0.017	0.0003
3.349	0.579	0.9954	3.417	0.9944	-0.001	0.018	0.0003
2.773	0.489	0.9943	2.721	0.9935	-0.001	0.018	0.0004
1.943	0.374	0.9929	1.954	0.9918	-0.001	0.017	0.0005
1.132	0.228	0.9889	1.112	0.9871	-0.002	0.013	0.0008
0.605	0.128	0.9816	0.609	0.9780	-0.004	0.008	0.0013

Expanded uncertainties (U) calculated with k = 2. $U_{(T)}$ = 0.04 K, $U_{(P)}$ = 0.007 MPa, $U_{(x)}$ = 0.018, $U_{(y)}$ = 0.0010.
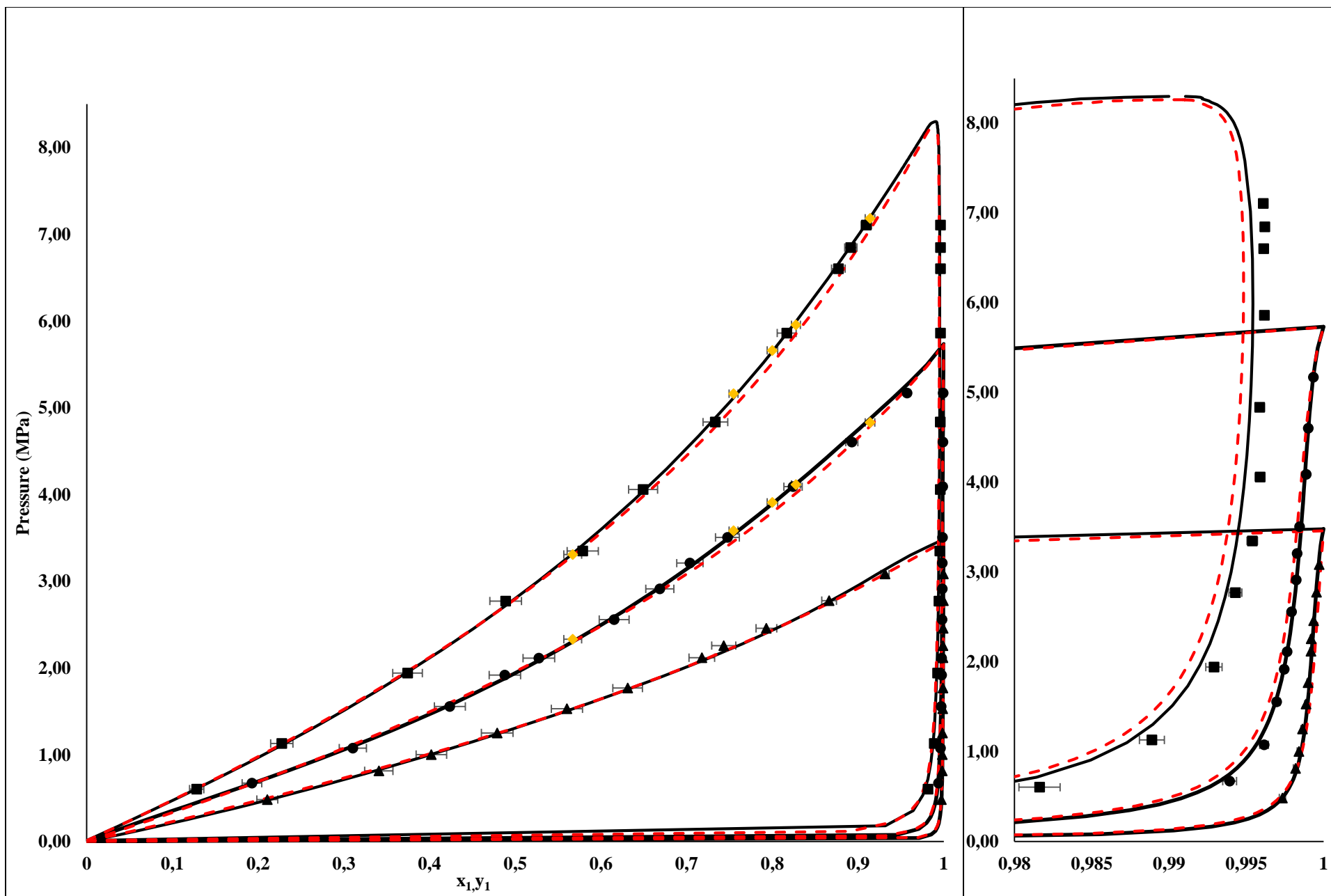
Figure 7-13: P-xy data for the carbon dioxide (1) + 1,1,2,2-tetrafluoroethyl 2,2,3,3-tetrafluoropropyl ether (2) binary system for three isotherms via the static analytic apparatus. (▲) 273.13 K, (●) 293.16 K, (■) 313.16 K. For two isotherms via the static synthetic apparatus: (◆) 293.16 K. (◆) 313.16 K. (——) PR-MC-WS-NRTL, (----) Peng - Robinson EoS.

The dipole moments in a carbon dioxide molecule cancel out due to the symmetry of the molecule, resulting in a net dipole moment of zero. Consequentially, the intermolecular forces in carbon dioxide are very weak. Thus the interaction of carbon dioxide and 1,1,2,2-tetrafluoroethyl 2,2,3,3-tetrafluoropropyl ether is dependent partly on the disparity of free electrons between the two chemical species, which then results in carbon dioxide acting as a Lewis acid (electron acceptor), while the fluorinated ether acts as the Lewis base (electron donor). The ether functional group is considered a hard Lewis base, due to the firmly bound electron outer shell (Hanson, 2001). Thus it has a strong affinity for binding with a hard Lewis acid such as carbon dioxide, forming ionic complexes. The interaction of the two chemical species is further enhanced by the presence of fluorine atoms within the hydrofluoroether. The high electronegativity of the fluorine atoms results in a decrease of internal cohesion within the fluorinated ether molecules, thus allowing easy access to the carbon dioxide molecules into the molecular cavities within the fluorinated ether. The negative deviation from Raoult's law then occurs because the intermolecular forces between the carbon dioxide and the fluorinated ether molecules are stronger than those between (CO_2 - CO_2) pairs, resulting in the prediction of a lower vapour pressure for the carbon dioxide when using Raoult's law (Annamalai et al., 2010).

Table 7-15: Error analysis for the carbon dioxide (1) +1,1,2,2-tetrafluoroethyl 2,2,3,3-tetrafluoropropyl ether (2) binary system for the case with individual regressed parameters.

Model	$AARD_p$ (%)	$BIAS_p$ (%)	AAD_p MPa	$AARD_{y1}$ (%)	$BIAS_{y1}$ (%)	AAD_{y1}	k_{ij}
				T[K] = 273.13			
PR-MC-WS-NRTL	0.985	0.125	0.018	0.05	-0.002	0.0001	0.331
Peng-Robinson	1.646	-0.224	0.025	0.019	0.0001	0.0002	-0.025
				T[K] = 293.16			
PR-MC-WS-NRTL	1.188	0.237	0.033	0.017	-0.004	0.0001	0.525
Peng-Robinson	1.728	-0.349	0.045	0.040	-0.038	0.0003	-0.032
				T[K] = 313.16			
PR-MC-WS-NRTL	0.891	0.122	0.029	0.124	-0.124	0.001	0.523
Peng-Robinson	1.564	-0.856	0.069	0.185	-0.185	0.002	-0.031

Table 7-15 displays the error analysis of the two models including values for the interaction parameter k_{ij} for each isotherm. The values were obtained through the individual regression of each isotherm. The deviations in the vapour phase for both models were good, with relative deviation values below 1%. The $AARD_p$ exceeded 1% for the Peng-Robinson model in all isotherms, while the $Bias_y$ for both models was below 0.5% for all isotherms. The isotherm measured at 293.16 K displayed the highest relative deviations in pressure for both models, but the deviation for the PR-MC-WS-NRTL model was slightly above 1%, and thus was deemed acceptable. The interaction parameters (k_{ij}) for the classical mixing rules were negative for every isotherm, which has been postulated to signify strong interactions between the constituents of the mixture (Rizvi, 2010).

Figure 7-14 shows the change of the relative volatility compared to the composition of the binary mixture. The experimental data is compared with the data calculated from the two models, with the PR-MC-WS-NRTL model exhibiting a significantly better fit relative to the Peng-Robinson EoS model.
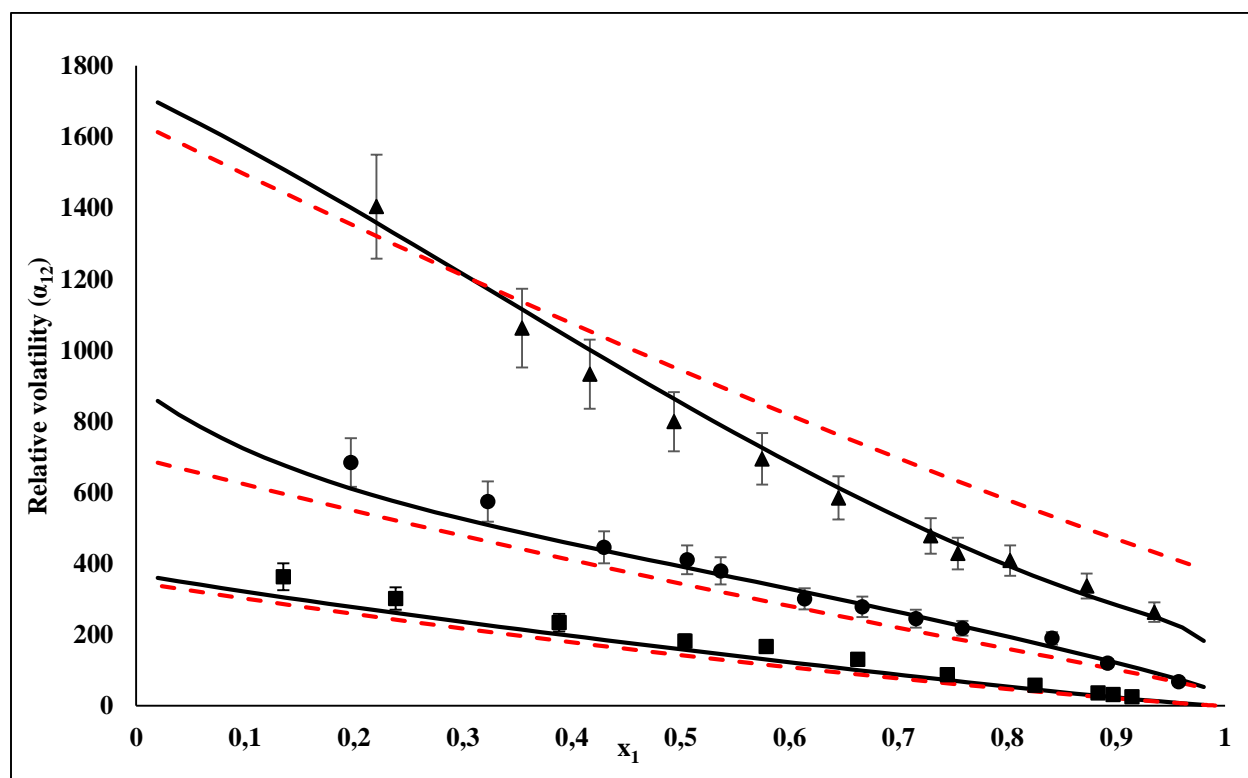
Figure 7-14: Relative volatility (α_{12}) as a function of composition for the carbon dioxide (1) + 1,1,2,2-Tetrafluoroethyl 2,2,3,3-tetrafluoropropyl ether (2) binary system. (▲) 273.13 K, (●) 293.16 K, (◆) 313.16 K. (—) PR-MC-WS-NRTL, (----) Peng-Robinson EoS.

Since the relative volatility is a function of both the vapour and liquid mole fractions, the lack of scatter in Figure 7-14 would, therefore, signify smooth trends in the experimental data. The PR-MC-WS-NRTL model data is well within the experimental uncertainties for the 273.13 K isotherm, but deviations from the model data are noted to rise slightly with an increase in temperature. The Peng- Robinson EoS is observed to deviate significantly from the experimental data, particularly for the lowest isotherm. The PR-MC-WS-NRTL model is thus the most suited to best describe this system.

Case with globally regressed parameters

The Wong Sandler binary parameter k_{ij} was regressed simultaneously for all the isotherms, generating a value of 0.524. The non-randomness parameter (α_{ij}) was not regressed but fixed at a value of 0.3. This value has been successfully used for nonpolar compounds such as PFCs and numerous other nonpolar chemical species with diverse functional groups. Thus it was deemed sufficient for use in all systems in the study.

The NRTL energy parameters were globally regressed across all isotherms, and the relationship is displayed in Table 7-16. The residual root mean square error (RRMSE) is noted to substantially increase when the isotherms are regressed globally.

Table 7-16: Globally and individually regressed PRWS model parameters for the carbon dioxide (1) +1,1,2,2-tetrafluoroethyl 2,2,3,3-tetrafluoropropyl (2) ether system.

Isotherm [K]	$b_{ij}{}^a$ [K]	$b_{ji}{}^a$ [K]	RRMSE
273.13	3607.431	-284.624	16.013
293.16	6986.500	5663.120	21.601
313.16	-107.156	9904.390	29.280
Global parameters: $k_{ij}{}^b$ = 0.524			
All isotherms	155.761	289.404	36.431

[a] Scalar NRTL model parameters, $\tau_{ij} = {}^{bij}/_{T}$, $\alpha_{ij} = 0.3$.

[b] Scalar WS mixing rule parameter incorporated into the Peng-Robinson EoS.
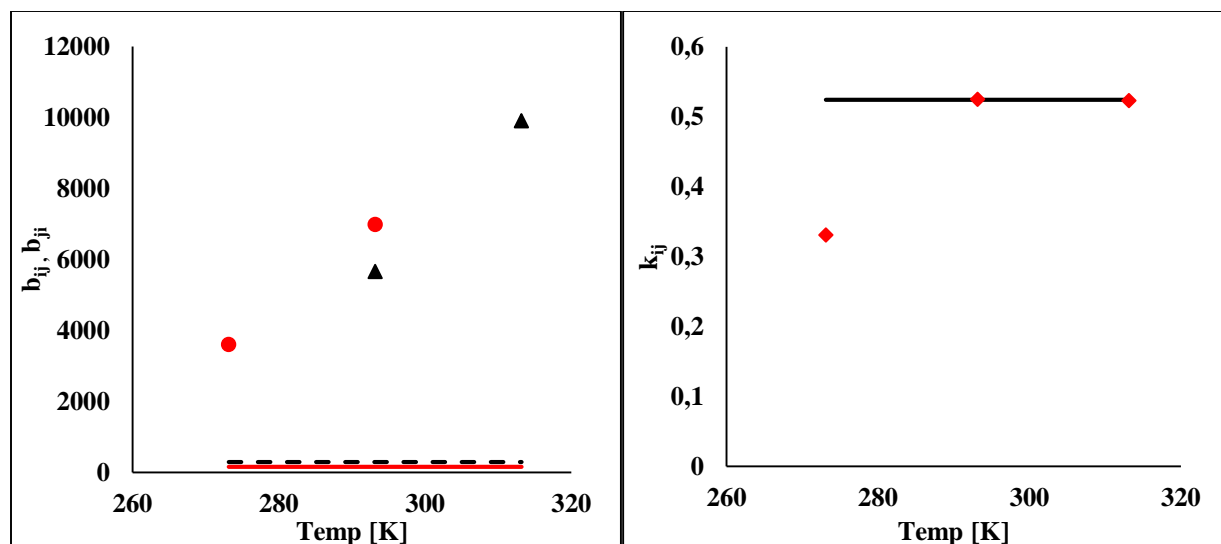
Figure 7-15: Model parameters for the carbon dioxide (1) + 1,1,2,2-tetrafluoroethyl 2,2,3,3-tetrafluoropropyl ether (2) binary system. (**Left**) Parameters for the NRTL model obtained through individual regression, ($\bullet$) b_{ij}, ($\blacktriangle$) b_{ji}, through global regression (—) b_{ij}, (-----).b_{ji} (**Right**) Parameters for the Wong Sandler mixing rules obtained through individual regression ($\blacklozenge$) k_{ij}, through global regression (—) k_{ij}.

Table 7-17: Error analyses for the carbon dioxide (1) +1,1,2,2-tetrafluoroethyl 2,2,3,3-tetrafluoropropyl ether (2) system for the case with global parameters.

Isotherm [K]	273.13	293.16	313.16
$AARD_p$ (%)	1.701	1.540	1.337
$BIAS_p$ (%)	0.092	0.658	-0.532
AAD_p (MPa)	0.024	0.036	0.040
$AARD_{y_1}$ (%)	0.032	0.015	0.108
$BIAS_{y_1}$ (%)	0.032	-0.004	-0.108
AAD_{y_1}	0.092	0.0001	0.001

The data displayed on Table 7-17 depicts relative deviations in pressure which exceed 1% for all three isotherms, while the relative deviations in the vapour phase are all less than 1%. Based on the relative deviation and Bias data, it is evident that individual regression of each isotherm produces better model descriptions of the experimental data but the globally regressed parameters

would also result in satisfactory results when used since all deviations generated where on overall less than 2%.

7.6.2 Carbon dioxide (1) + perfluoroheptane (2)

This binary system was measured at temperatures of (273.14, 293.14 and 313.13) K. The generated phase equilibria data were correlated using the PR-MC-WS-NRTL model and the Peng-Robinson EoS with classical mixing rules. While the Peng –Robinson EoS failed to effectively describe the carbon dioxide (1) + perfluorooctane (2) system which was measured for one isotherm, its use in correlating this particular binary pair was done so as to note the effect of temperature on the model. Both models were noted to represent the lowest isotherm fairly well in both the liquid and the vapour phases. However as the temperature of the binary mixture increased and approached the critical temperature of the volatile component, the Peng-Robinson EoS model began to under estimate the bubble curve from ($x_1 > 0.7$). This deviation became more pronounced as the temperature increased, rendering the model ineffective in describing the binary system, while the PR-MC-WS-NRTL model performed well, describing the data well within the experimental uncertainty in the liquid phase. However, the vapour phase was not as accurately correlated by the model. The experimental and regressed data for the binary system is tabulated in Table 7-18, while the P-xy chart is depicted in Figure 7-16.

Table 7-18: Experimental and regressed VLE data for carbon dioxide (1) + perfluoroheptane (2).

Experimental			PR-MC-WS-NRTL			Expanded Uncertainties	
P[MPa]	x_1	y_1	P[MPa]	y_1	$y_{calc} - y_{exp}$	$U_{(x_1)}$	$U_{(y_1)}$
T = 273.14 K							
3.247	0.944	0.9992	3.264	0.9994	0.0001	0.004	0.0001
3.070	0.892	0.9990	3.111	0.9991	0.0002	0.007	0.0001
2.850	0.818	0.9989	2.882	0.9989	0.0003	0.012	0.0001
2.687	0.765	0.9988	2.702	0.9987	0.0004	0.014	0.0001
2.505	0.709	0.9988	2.508	0.9986	0.0005	0.016	0.0001
2.211	0.621	0.9986	2.198	0.9984	0.0004	0.018	0.0001
1.779	0.503	0.9984	1.780	0.9980	0.0005	0.019	0.0001
1.339	0.377	0.9980	1.331	0.9975	0.0005	0.019	0.0002
1.015	0.292	0.9973	1.023	0.9969	-0.0002	0.019	0.0002
0.755	0.219	0.9965	0.762	0.9960	-0.0001	0.019	0.0003
0.439	0.126	0.9939	0.435	0.9934	0.0001	0.009	0.0004
T = 293.13 K							
5.065	0.933	0.9978	5.138	0.9974	0.0004	0.005	0.0002
4.760	0.883	0.9971	4.828	0.9969	0.0014	0.008	0.0002
4.452	0.833	0.9968	4.511	0.9966	0.0017	0.011	0.0002
3.789	0.720	0.9962	3.781	0.9961	0.0002	0.016	0.0003
3.087	0.605	0.9963	3.089	0.9956	0.0001	0.019	0.0003
2.233	0.451	0.9956	2.235	0.9947	0.0007	0.019	0.0003
1.787	0.365	0.9950	1.779	0.9938	0.0010	0.018	0.0004
1.568	0.321	0.9946	1.551	0.9932	0.0012	0.017	0.0004
1.355	0.283	0.9938	1.354	0.9925	0.0013	0.016	0.0005
0.976	0.206	0.9918	0.732	0.9902	0.0017	0.013	0.0006
0.726	0.157	0.9892	0.968	0.9876	0.0002	0.008	0.0012
0.510	0.112	0.9849	0.514	0.9830	0.0020	0.010	0.0006
T = 313.13 K							
7.285	0.927	0.990	7.434	0.988	0.002	0.005	0.001
6.978	0.898	0.991	7.106	0.989	0.003	0.007	0.001
6.543	0.855	0.991	6.607	0.989	0.002	0.010	0.001
5.958	0.800	0.991	5.993	0.990	0.004	0.013	0.001
4.999	0.697	0.991	4.952	0.990	0.001	0.016	0.001
4.674	0.664	0.991	4.650	0.990	0.002	0.017	0.001
3.763	0.557	0.991	3.739	0.989	0.005	0.019	0.001
2.898	0.446	0.990	2.892	0.988	0.001	0.019	0.001
1.856	0.298	0.987	1.852	0.985	0.001	0.016	0.001
1.132	0.189	0.980	1.136	0.978	0.001	0.007	0.003
0.807	0.134	0.974	0.796	0.970	0.002	0.012	0.002

Expanded uncertainties (U) calculated with k = 2. $U_{(T)}$ = 0.04 K, $U_{(P)}$ = 0.007 MPa, $U_{(x)}$ = 0.019, $U_{(y)}$ = 0.003.
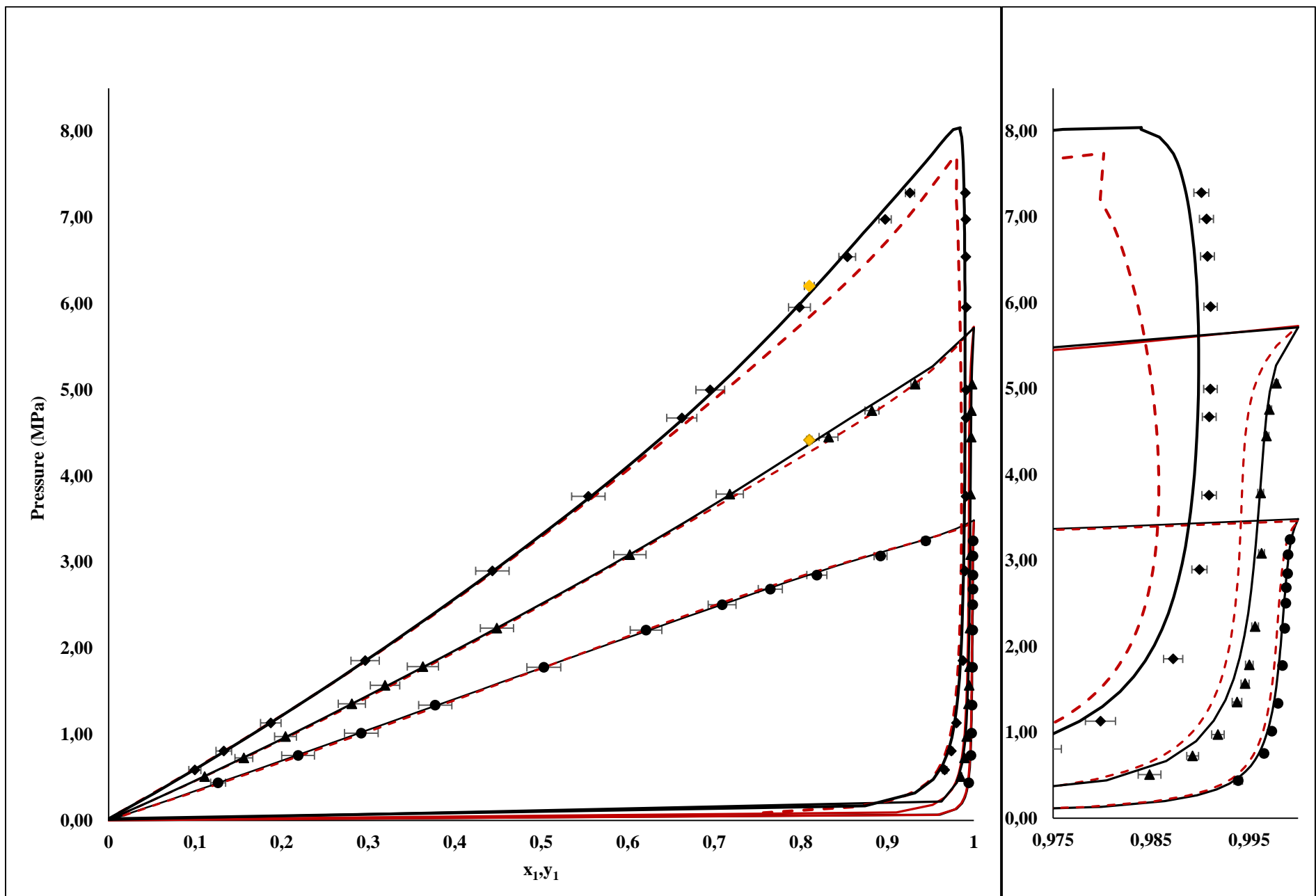
Figure 7-16: P-xy data for the carbon dioxide (1) + perfluoroheptane (2), for three isotherms via the static analytic apparatus. (●) 273.13 K (▲) 293.16 K, (◆) 313.16 K. For two isotherms via the static synthetic apparatus: (◆) 293.16 K. (◆) 313.16 K. (——) PR-MC-WS-NRTL, (----) Peng- Robinson EoS.

The regressed data for the two isotherms which were measured below the carbon dioxide critical temperature was observed to develop a dew-bubble curve with a common tangent (Sengers, 1986), which is termed the "birds beak" of infinite slope. This phenomenon was better developed and more pronounced for the isotherm at 293.16 K, since the isothermal temperature was in close proximity to the carbon dioxide critical temperature. Experimental data were also measured using the static synthetic apparatus, and these matched the data from the static analytical apparatus well within the compositional uncertainty.

The shape of the bubble line from the three isotherms attests to a slightly positive deviation from Raoult's law. This phenomenon is further affirmed by the positive values of the binary interaction parameter (k_{ij}), which was obtained from the use of the Peng-Robinson EoS with classical mixing rules. The parameter reflects the strength of unlike interactions within the mixture without necessarily being an accurate measure of the aforementioned strength. (Sadus, 2012). The solubility of the gas in the perfluorocarbon was enhanced by the fluorine atoms similarly as was discussed for the previous system. However the carbon dioxide – perfluoroheptane interactive forces are less than those of $(CO_2 - CO_2)$ pairs, as indicated by the positive deviation from Raoult's law.

Table 7-19: Error analysis for carbon dioxide (1) +perfluoroheptane (2) binary system for the case with individual regressed parameters.

Model	$AARD_p$ (%)	$BIAS_p$ (%)	AAD_p MPa	$AARD_{y1}$ (%)	$BIAS_{y1}$ (%)	AAD_{y1}	k_{ij}
			T[K] = 273.14				
PR-MC-WS-NRTL	0.690	0.308	0.014	0.027	-0.022	0.0002	0.669
Peng-Robinson	1.123	0.238	0.022	0.073	-0.073	0.0007	0.046
			T[K] = 293.14				
PR-MC-WS-NRTL	0.732	0.278	0.022	0.095	-0.095	0.0009	0.676
Peng-Robinson	0.757	-0.481	0.018	0.246	-0.241	0.002	0.049
			T[K] = 313.13				
PR-MC-WS-NRTL	0.903	0.089	0.042	0.218	-0.221	0.002	0.677
Peng-Robinson	2.026	-1.166	0.097	0.621	-0.622	0.006	0.054

The statistical values, as well as the binary interaction parameters displayed in Table 7-19, were obtained through the individual regression of each isotherm. The AARD, AAD and Bias generated through the PR-MC-WS-NRTL model were all below 1%, signifying a good relationship between the experimental and the regressed data. The Peng–Robinson EoS model however performed adequately for the two lowest isotherms, with Bias and absolute deviations below 2%, but the correlation began to fail as the temperature increased. The highest isotherm was marked with an $AARD_p$ value that exceeded 2%. Thus the PR-MC-WS-NRTL model was deemed the more adequate of the two in describing systems of carbon dioxide with PFCs.

The relative volatility plot for the binary system is shown in Figure 7-17. The discrepancy between the experimental and regressed values was due to the PR-MC-WS-NRTL model's inability to describe the vapour phase to within the compositional uncertainty. The (273.14 and 293.14) K isotherms displayed higher deviations from the model data which were more pronounced near the equimolar region.
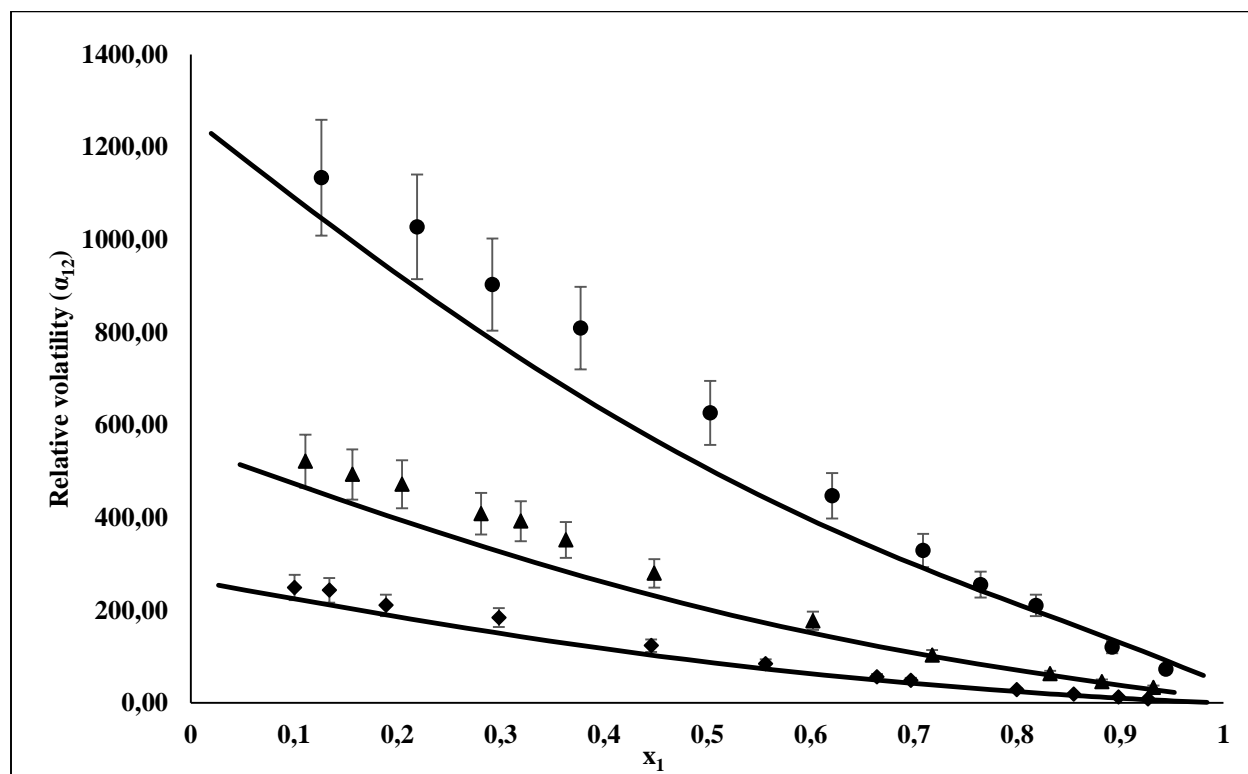
Figure 7-17: Relative volatility (α_{12}) as a function of composition for the carbon dioxide (1) + perfluoroheptane (2) binary system. (●) 273.14 K, (▲) 293.14 K, (◆) 313.13 K. (—) PR-MC-WS-NRTL model.

Globally regressed parameters

All three of the measured isotherms were regressed simultaneously/globally, generating a (k_{ij}) value of 0.675. Global regression was done in order to verify whether a set of parameters could be used across a temperature profile viz., to test for temperature dependence. Table 7-20 displays the NRTL energy parameters generated for each isotherm, alongside parameters generated from simultaneous regression and the RRMSE. The statistical error was noted to be lower for the case with global regression.

Table 7-20: Globally and individually regressed PRWS model parameters for the carbon dioxide (1) +perfluoroheptane system.

Isotherm	$b_{ij}{}^a$ [K]	$b_{ji}{}^a$ [K]	RRMSE
273.14	-1390.611	-1654.793	20.045
293.14	479.544	2048.098	20.807
313.13	485.814	-2330.951	24.273
Global parameters: $k_{ij}{}^b$ = 0.675			
All isotherms	675.850	490.718	18.964

a Scalar NRTL model parameters, $\tau_{ij} = {}^{bij}/_T$, $\alpha_{ij} = 0.3$.

b Scalar WS mixing rule parameter incorporated into the Peng-Robinson EoS.
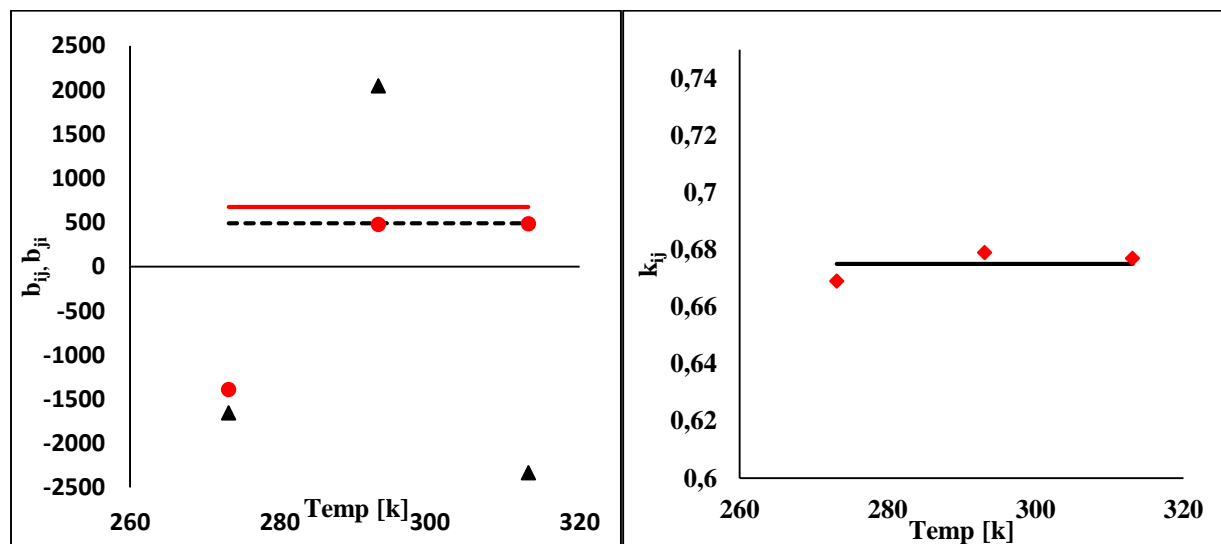
Figure 7-18: Model parameters for the carbon dioxide (1) + perfluoroheptane (2) binary system. (**Left**) Parameters for the NRTL model obtained through individual regression, ($\bullet$) b_{ij},($\blacktriangle$) b_{ji}, through global regression (——) b_{ij}, (-----) b_{ji}. (**Right**) Parameters for the Wong Sandler mixing rules obtained through individual regression ($\blacklozenge$) k_{ij}, through global regression (——) k_{ij}.

The relative deviations and Bias which relate the nature of the fit between the experimental and regressed data were noted to be less than 1%, as displayed in Table 7-21. The statistical data, therefore, affirmed the use of a single set of parameters for phase equilibria data across a temperature profile.

Table 7-21: Error analysis for the carbon dioxide (1) +perfluoroheptane (2) system for the case with global parameters.

Isotherm [K]	273.14	293.14	313.13
$AARD_p$ (%)	0.821	0.758	0.720
$BIAS_p$ (%)	0.406	0.350	0.084
AAD_p (MPa)	0.018	0.023	0.029
$AARD_{y_1}$ (%)	0.026	0.095	0.231
$BIAS_{y_1}$ (%)	-0.020	-0.095	-0.231
AAD_{y_1}	0.0002	0.0009	0.002

7.6.3 Carbon dioxide (1) + perfluorononane (2)

Table 7-22: Experimental and regressed VLE data for carbon dioxide (1) + perfluorononane (2).

Experimental			PR-MC-WS-NRTL			Expanded Uncertainties	
P[MPa]	x_1	y_1	P[MPa]	y_1	$y_{calc} - y_{exp}$	$U_{(x_1)}$	$U_{(y_1)}$
T = 273.15 K							
3.276	0.943	0.99960	3.327	0.99976	0.00016	0.004	0.00003
3.173	0.906	0.99960	3.257	0.99973	0.00012	0.006	0.00003
2.952	0.818	0.99955	2.998	0.99967	0.00012	0.010	0.00003
2.862	0.790	0.99958	2.895	0.99965	0.00007	0.011	0.00003
2.668	0.727	0.99954	2.651	0.99962	0.00008	0.013	0.00003
2.430	0.662	0.99955	2.401	0.99959	0.00004	0.015	0.00003
2.130	0.577	0.99959	2.088	0.99956	-0.00003	0.016	0.00003
1.976	0.536	0.99955	1.943	0.99955	-0.00001	0.017	0.00003
1.804	0.486	0.99953	1.775	0.99952	-0.00001	0.017	0.00003
1.452	0.391	0.99950	1.455	0.99947	-0.00008	0.016	0.00003
1.039	0.276	0.99935	1.070	0.99937	0.00002	0.013	0.00004
T = 293.15K							
4.975	0.901	0.99926	5.230	0.99907	-0.0002	0.006	0.00005
4.714	0.853	0.99928	4.910	0.99904	-0.0002	0.008	0.00005
4.410	0.800	0.99926	4.475	0.99900	-0.0003	0.011	0.00005
3.958	0.727	0.99928	3.885	0.99895	-0.0003	0.013	0.00005
3.370	0.630	0.99922	3.221	0.99887	-0.0003	0.016	0.00005
3.053	0.578	0.99915	2.913	0.99882	-0.0003	0.016	0.00006
2.551	0.493	0.99916	2.463	0.99873	-0.0004	0.017	0.00006
1.741	0.353	0.99908	1.782	0.99850	-0.0006	0.015	0.00006
1.168	0.243	0.99876	1.251	0.99813	-0.0006	0.012	0.00008
0.680	0.146	0.99822	0.775	0.99734	-0.0009	0.008	0.00012
T = 313.15 K							
7.098	0.881	0.9970	7.234	0.9960	-0.0010	0.007	0.0002
6.89	0.863	0.9972	7.007	0.9963	-0.0009	0.008	0.0002
6.432	0.823	0.9973	6.512	0.9968	-0.0005	0.007	0.0002
5.64	0.741	0.9975	5.572	0.9973	-0.0002	0.013	0.0002
4.814	0.656	0.9980	4.722	0.9976	-0.0004	0.015	0.0001
4.044	0.575	0.9979	3.994	0.9977	-0.0002	0.016	0.0001
3.664	0.533	0.9980	3.638	0.9977	-0.0003	0.017	0.0001
3.055	0.459	0.9979	3.044	0.9977	-0.0002	0.017	0.0001
1.919	0.309	0.9973	1.922	0.9974	0.0000	0.014	0.0002
1.353	0.227	0.9967	1.358	0.9968	0.0001	0.012	0.0002
0.746	0.130	0.9951	0.744	0.9950	-0.0001	0.008	0.0003

Expanded uncertainties (U) calculated with k = 2. $U_{(T)}$ = 0.04 K, $U_{(P)}$ = 0.007 MPa, $U_{(x)}$ = 0.017, $U_{(y)}$ = 0.0003.
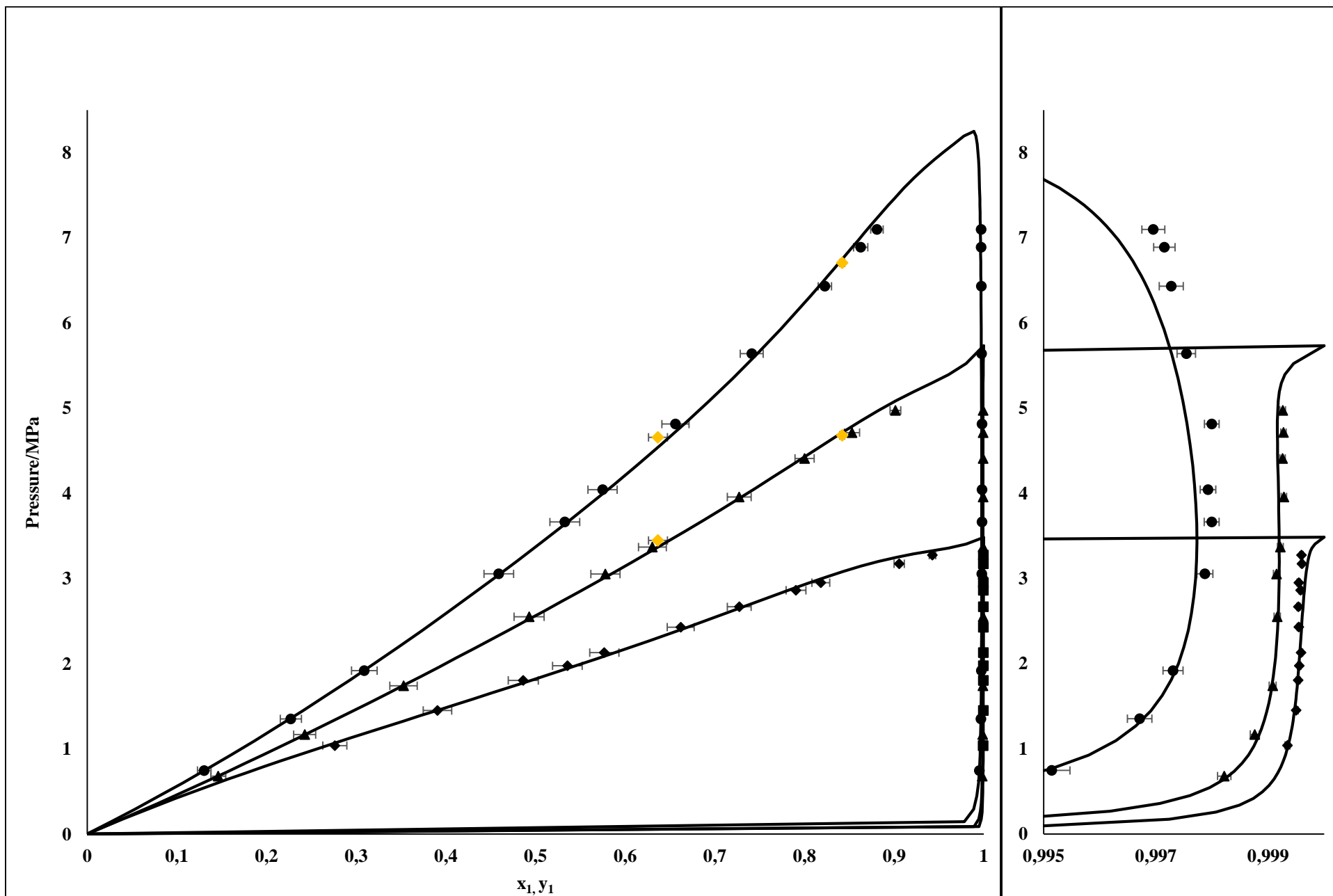
Figure 7-19: P-xy data for the carbon dioxide (1) + perflurononane (2) binary system for three isotherms via the static analytic apparatus. (◆) 273.15 K, (▲) 293.15 K, (●) 313.15 K. For two isotherms via the static synthetic apparatus: (◆) 293.15 K. (◆) 313.15 K. (—) PR-MC-WS-NRTL model.

The carbon dioxide-perfluorononane binary system was correlated using only the PR-MC-WS-NRTL model. This was done in light of the discussion for the perfluorooctane and perfluoroheptane systems, which established that the aforementioned model was sufficient in correlating carbon dioxide-PFC binary data, while the Peng-Robinson EoS was not as proficient. Figure 7-19 depicts the P-xy chart for the system, and the generated phase envelopes were noted to be very similar to those of the carbon dioxide-perfluoroheptane system. This was due to the minor difference in carbon chain length between the PFCs, which meant that the ionisation potentials within the individual molecules of each liquid were similar, resulting in near identical carbon dioxide absorption capabilities. The data measured using the synthetic apparatus was again consistent with the analytic apparatus data, thus affirming the accuracy of the measurements of all three novel binary systems.

The P-xy chart depicts a relatively smooth relation between the experimental and regressed data for all three isotherms. However, Table 7-23 highlights a high $AARD_p$ value of 1.56 for the isotherm measured at 273.15 K, which was in contrast to the low deviations obtained for the other two isotherms. This discrepancy was due to an unforeseen anomaly which was observed during the measurement of data at the temperature stated above. The carbon dioxide-perfluorononane binary mixture was observed to freeze at pressures below 1 MPa at the 273.15 K isotherm, and as such sampling could not be performed at low pressures. Sampling at higher pressures was possible, but the withdrawn samples lacked uniformity in GC peak areas, particularly in the liquid phase, resulting in some scatter in the data. The reason behind the anomaly was not understood as the reported freezing point for pure perfluorononane is 257.15 K as reported by Haszeldine and Smith (1951).

Table 7-23: Error analysis for the carbon dioxide (1) +perfluorononane (2) system generated from the PR-MC-WS-NRTL model for the case with individually regressed parameters.

T[K]	$AARD_P$(%)	$BIAS_P$(%)	AAD_P (MPa)	$AARD_{y1}$(%)	$BIAS_{y1}$(%)	AAD_{y1}	k_{ij}
273.15	1.560	0.268	0.036	0.007	0.005	0.0004	0.741
293.15	0.876	0.078	0.033	0.005	-0.002	0.00006	0.754
313.15	1.004	-0.022	0.054	0.035	-0.033	0.0003	0.763

The plot of relative volatility against composition displayed smooth trends for all three isotherms. However some scatter in the data was noted for the 273.15 K isotherm. As is evident from the plot in Figure 7-20, the scatter was concentrated in the region with high carbon dioxide mole fractions in the liquid phase viz., at relatively high pressure, which is consistent with the data for the 273.15 K isotherm in Figure 7-19, which shows scatter in the vapour phase at high pressure.
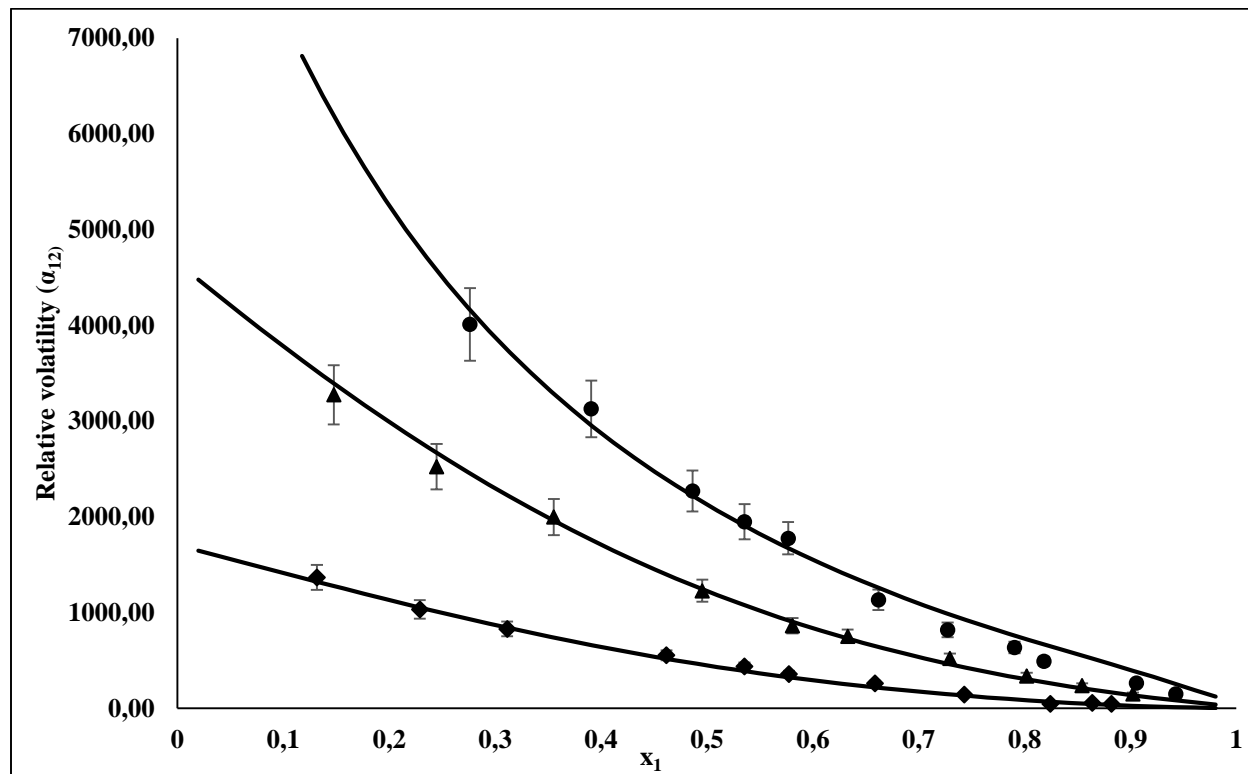
Figure 7-20: Relative volatility (α_{12}) as a function of composition for the carbon dioxide (1) + perfluorononane (2) binary system. (●) 273.15 K, (▲) 293.15 K, (◆) 313.15 K. (—) PR-MC-WS-NRTL model.

Globally regressed parameters

Due to the anomaly experienced at 273.15 K, the data from this isotherm was not utilised in the global regression of the experimental data. The NRTL energy parameters, as well as the RRMSE which were generated through global and individual regression of the isotherms, are displayed in Table 7-24. The RRMSE was very high for the 273.15 K isotherm, indicating a significant discrepancy between model and experimental data. This result deviated from what was expected,

as the RRMSE has been noted to increase with temperature in all the other measured binary systems.

Table 7-24: Globally and individually regressed PRWS model parameters for the carbon dioxide (1) +perflurononane system.

Isotherm T[K]	b_{ij}[a] [K]	b_{ji}[a] [K]	RRMSE
273.15	1629.160	136.694	34.265
293.15	-73.898	-1000	16.308
313.15	-297.750	-839.427	22.603
Global parameters (k_{ij}[b] = 0.759)			
All isotherms	569.672	881.438	18.88

[a] Scalar NRTL model parameters, $\tau_{ij} = {}^{bij}/_{T}$, $\alpha_{ij} = 0.3$.

[b] Scalar WS mixing rule parameter incorporated into the Peng-Robinson EoS.
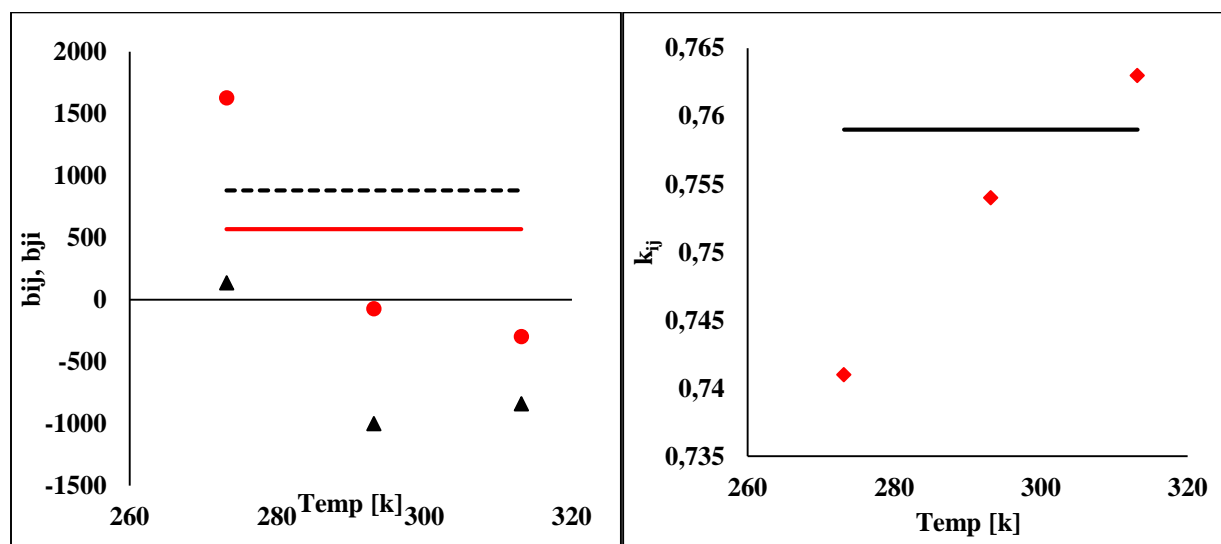
Figure 7-21: Model parameters for the carbon dioxide (1) + perfluorononane (2) binary system. (**Left**) Parameters for the NRTL model obtained through individual regression, (●) b_{ij}, (▲) b_{ji}, through global regression (——) b_{ij}, (-----) b_{ji}. (**Right**) Parameters for the Wong Sandler mixing rules obtained through individual regression (◆) k_{ij}, through global regression (——) k_{ij}.

The deviations and Bias generated through the simultaneous regression of the two isotherms highlighted in Table 7-25 did not substantially exceed 1%. This then meant that the parameters

generated through globally regressing the two isotherms could be sufficiently used across a temperature profile.

Table 7-25: Error analysis for the carbon dioxide (1) +perfluorononane (2) system for the case with global parameters.

Isotherm [K]	$AARD_p$ (%)	$BIAS_p(\%)$	$AAD_p(MPa)$	$AARD_{y_1}(\%)$	$BIAS_{y_1}(\%)$	AAD_{y_1}
293.15	1.073	0.241	0.041	0.005	0.0009	0.0001
313.15	0.840	-0.182	0.043	0.040	-0.038	0.0004

7.7 Comparison of carbon dioxide solubility in solvents

The process of selecting a suitable physical solvent for absorption is still hindered by the lack of established quantitative methods which could be used to make the selection process efficient (Henni et al., 2005). Very few comprehensive screening studies have been conducted due to the time and cost constraints which are inherent to such research, as was mentioned in Chapter 2. Thus an efficient and cheaper way of streamlining potential solvents would be to benchmark them against industrially reputable solvents. In this work, the generated carbon dioxide solubility data were compared to literature sources which measured data for different fluorinated compounds and an industrial solvent, in a bid to identify promising compounds regarding carbon dioxide dissolution.

Fluorinated compounds

A number of carbon dioxide + fluoro-compound binary systems have been measured and published in the literature (Lazzaroni et al., 2005; Dias et al., 2006; Tochigi et al., 2010), and the data therein presented in the form of pressure-composition plots. By virtue of the similarity in experimental methods used in the aforementioned studies and in the work carried out in this study, a direct comparison of the generated experimental data could be conducted. In order to benchmark the carbon dioxide dissolution abilities of the fluorinated compounds, GENOSORB 1753, which is an industrial solvent formulated from a mixture of polyethylene glycol dimethyl ethers was also included in the comparison. Figure 7-22 depicts a P-x chart which consists of binary data for carbon dioxide with the following compounds: perfluoro-hexane (C_6F_{14}), perfluoro-benzene (C_6F_6), perfluoro-toluene (C_7F_8), perfluoro-methylcyclohexane (C_7F_{14}), perfluoro-heptane

(C_7F_{16}), perfluoro-octane (C_8F_{18}), perfluoro-nonane (C_9F_{20}), perfluorodecalin ($C_{10}F_{18}$), 1,1,2,2-Tetrafluoroethyl 2,2,3,3-tetrafluoropropyl ether ($C_5H_4F_8O$) and GENOSORB 1753 [$CH_3(CH_2CH_2O)_nCH_3$], where n is usually between 4 and 10 (Rayer et al., 2012). The chart features data measured at 313.15 K only since this was the common isotherm across all measurements.

.
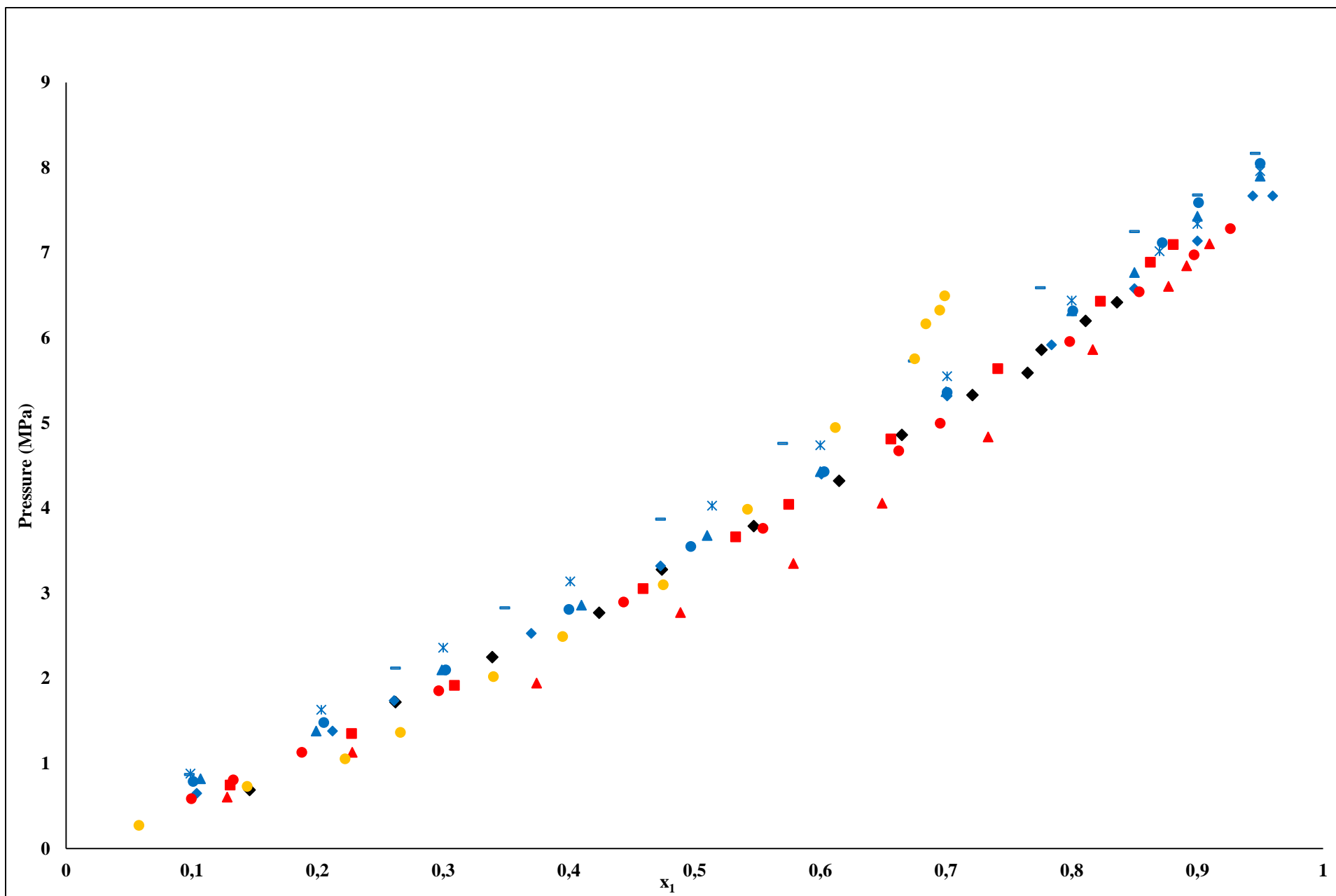
Figure 7-22: P-x plots for CO_2 (1) + fluoro-compound (2) systems at 313.15 K. **(a)** Exp data: (▲) $C_5H_4F_8O$, (●) C_7F_{16} (■) C_9F_{20}, **(b)** Lazzaroni et al. (2005):(◆) C_6F_{14}, **(c)** Dias et al. (2006) : (◆) C_8F_{18}, (▲) C_6F_6, (●) C_7F_8, (*) C_7F_{14} and (—) $C_{10}F_{18}$ **(d)** Rayer et al. (2012) (●) [$CH_3O(CH_2CH_2O)_nCH_3$], n between 4 – 10.

The chart displays a clear disparity in the ability to dissolve carbon dioxide between the perfluorocarbons and the hydrofluoroether. The straight chain PFCs are noted to have a similar affinity for the gas due to the minor differences in carbon chain length from C_6 to C_9. However, the carbon chain length has been noted to be directly proportional to the solubility of carbon dioxide in PFCs, as was highlighted by Heintz et al. (2008), who studied the solubility of carbon dioxide in the higher chain compounds perfluoro-perhydrofluorene ($C_{13}F_{22}$), perfluoro-perhydrophenathrene ($C_{14}F_{24}$) and perfluro-cyclohexylmethyldecalin ($C_{17}F_{30}$) through the use of a Zipper Clave agitated reactor. The cyclic and aromatic compounds displayed the lowest affinity for carbon dioxide, with the latter being the better of the two structural configurations.

The relatively high solubility of carbon dioxide in fluorinated compounds has primarily been attributed to the similarity in the polarisability parameters of the gas and the liquids (Hoefling et al., 1992). However, the hydrofluoroether out performs the PFCs virtue of the ether functional group which acts as an electron donor, thus further enhancing carbon dioxide solubility. The analysis of the data herein, therefore, attests to the need to further study fluorinated compounds which contain an electron donating functional group, as these will most likely out-perform PFCs in applications dealing with carbon dioxide dissolution.

1,1,2,2-tetrafluoroethyl 2,2,3,3-tetrafluoropropyl ether and an industrial solvent.

The most prominent physical absorption process thus far has been SELEXOL™, which is currently licensed to the Dow Chemical Company (Michigan, USA). The process employs a solvent which consists of a mixture of polyethylene glycol dimethyl ethers and is currently installed in over 60 commercial plants worldwide for the treatment of Integrated Gasification Combined Cycle (IGCC) synthesis gases (Rayer et al., 2012).

However, the solubility data found in the literature for carbon dioxide in the SELEXOL solvent is represented in the form of Henry's constants, which were generated at low pressure (Xu, 1991). This then meant that a direct comparison of the SELEXOL solvent with the 1,1,2,2-tetrafluoroethyl 2,2,3,3-tetrafluoropropyl ether in terms of the ability to absorb carbon dioxide could not be effectively attained. Henry's law constants for the hydrofluoroether at high pressures could have been computed using the Krichevsky-Kasarnovsky/Krichevsky – Illinskaya equations. However, both equations are limited by the fact that they can only be utilised in the dilute region, up-to mole fraction ranges with a maximum of 0.03 and 0.2 respectively (Prausnitz et al., 1998). This then

entails that in the narrow mole fraction range, the heavier industrial solvents such as SELEXOL and GENOSORB, with significantly lower vapour pressures would effectively have lower Henry's law constants compared to the hydrofluoroether, which would assert to better solubility. The assessment above is justified by the fact that the GENORSOB solvent exhibited near identical carbon dioxide absorption ability as the hydrofluoroether in the (0.1– 0.2) mole fraction range, as shown in Figure 7-22. However, a result considering such a narrow mole fraction range would be inconclusive. Thus based on this reasoning, Henry's law constants for the hydrofluoroether were not computed. P-x data for the GENOSORB 1753 solvent were used to benchmark the data as shown in Figure 7-22. The industrial solvent displays better absorption capabilities for the gas compared to all the PFCs in the (0 – 0.5) mole fraction range, and similar capability as the hydorfluoroether in the (0 – 0.2) mole fraction range. The hydrofluoroether, however, is shown to significantly out-perform GENOSORB 1753 in the (0.2 – 1) range. Table 7-26 displays Henry's law constants for the SELEXOL and GENOSORB solvents, highlighting the close proximity in carbon dioxide absorption capabilities between the two solvents in the dilute region.

Table 7-26: Henry's law constants (*H*) for carbon dioxide in polyethylene glycol dimethyl ethers at low pressure. Adapted from (Rayer et al., 2012).

	Solvents	
Temperature [K]	**SELEXOL[a]** H_{CO_2} **(MPa)**	**GENOSORB[b]** H_{CO_2} **(MPa)**
298.15	3.52	3.43
313.15	4.67	4.70
333.15	6.55	6.32

[a](Xu, 1991)
[b](Rayer et al., 2012)

The similarity in Henry's law constants for the two solvents asserts to the ability of the GENOSORB 1753 solvent to perform on par with the SELEXOL solvent regarding carbon dioxide absorption in the dilute region. Based on the aforementioned assessment, the hydrofluoroether can also be expected to perform on par if not better than the SELEXOL solvent in-terms of carbon dioxide dissolution capabilities only if a wider mole fraction range is considered.

In retrospect, high absorption capacity alone is not sufficient when considering a solvent for gas cleaning applications. Zawacki et al. (1981) assert that both choices of solvent and process design are imperative in the selection of an acid gas removal system, and further highlights that solvents with high absorption capacity for carbon dioxide may also exhibit a high capacity for hydrocarbons, therefore rendering their use counterintuitive.

Chapter 8

8   Conclusions and Recommendations

8.1   Conclusions

The corner stone of the work carried out in this project was the measurement of high-pressure vapour – liquid equilibrium data using a static analytic apparatus. Thus in concluding the study, a synopsis of every system measured was undertaken, including the test system data, in order to show consistency in technique throughout the measurements, since accurate results are paramount for the design of separation equipment.

The test system carbon dioxide (1) + hexane (2) was measured at 313.12 K. The experimental results from this system compared very well to the reference data from Li et al. (1981), with slight discrepancies occurring in the region with ($x_1 > 0.8$). The test system of carbon dioxide (1) + perfluorooctane (2) at 293.12 K showed substantial discrepancies between the experimental and the reference data of Dias et al. (2006). The data points measured in this work using a static synthetic apparatus matched perfectly with the data from the analytic apparatus within the uncertainty. The experimental data was regressed using the PR-MC-WS-NRTL model and the Peng –Robinson EoS with classical mixing rules respectively, with the former generating a good fit, with relative deviations and bias which were less than 1%, whilst the latter substantially overestimated the bubble pressure curve.

Three novel binary systems were measured, comprising of two perfluorocarbons (C_7F_{16}, C_9F_{20}) and a hydrofluoroether ($C_5H_4F_8O$) in conjunction with carbon dioxide. These measurements were carried out at three isotherms (273.15, 293.15 and 313.15) K for each binary pair. The carbon dioxide (1) + 1,1,2,2-tetrafluoroethyl 2,2,3,3-tetrafluoropropyl ether (2) binary pair was correlated using both the PR-MC-WS-NRTL model and the Peng-Robinson EoS with classical mixing rules, with the more complex model generating considerably better relative deviations, which were below 1%. The interaction of the gas with the hydrofluoroether was particularly interesting as it exhibited negative deviation from Raoult's law, which signified that the gas-hydrofluoroether interaction was stronger than the interaction between the respective pure molecules of the two chemical species.

The systems with the PFCs (C_7F_{16}, C_9F_{20}) displayed similar phase envelopes which exhibited a slightly positive deviation from Raoult's law. The absorption capabilities of the PFCs have been noted to increase with an increase in chain length, as this would result in a similar increase in ionisation potential within the liquid molecules. However, the chain length difference between the main PFCs studied in this work was not substantial enough to warrant any discernible difference in absorption capabilities between the two liquids. The PFCs were both correlated using the PR-MC-WS-NRTL model, generating relative deviations and bias which were less than 1%, with the exception of the lowest isotherm for the carbon dioxide (1) + perfluorononane (2) system, which exhibited deviations in pressure which were in the (1.5 – 2) % range.

A direct comparison of an array of P-x data for carbon dioxide + fluorinated compounds was undertaken to examine the effects of functional groups on the carbon dioxide dissolution capabilities of fluorinated compounds. The comparison was carried out using only data measured at 313.15 K and included the following chemical species: (C_6F_{14}), (C_6F_6), (C_7F_8), (C_7F_{14}), (C_7F_{16}), (C_8F_{18}), (C_9F_{20}), ($C_{10}F_{18}$), ($C_5H_4F_8O$) and the industrial solvent GENOSORB 1753 [$CH_3(CH_2CH_2O)_nCH_3$], were n is in the range (4 – 10). Based on the analysis, it was evident that the hydrofluoroether was a better solvent in terms of carbon dioxide absorption capabilities, even when compared to the industrial solvent.

8.2   Recommendations

As has been stated a number of times in this work, high-pressure VLE measurements can be a daunting and cumbersome task, and as such, the equipment used should be designed in such a manner that it alleviates some if not most of the burden. The main apparatus used in this work suffered from poor mixing which resulted in longer equilibration periods for the binary mixtures. In order to rectify this problem, the equipment should be retrofitted with a mixing mechanism which is similar to that which was used in the work of Nelson et al. (2016). This therefore would require the machining of four new flanges for the equilibrium cell housing. The positioning of the ROLSI™ base plate should also be re-adjusted in order to allow the sampler to be positioned perfectly vertical relative to the cell. This would prevent any bending of the sampler capillary, which could be detrimental to the measurements. The carrier gas lines which are responsible for transporting the samples from the ROLSI™ base plate to the GC should be replaced with new

lines which have the least number of interconnections possible. This would reduce the number of potential leak sources.

The experimental work performed alluded to the fact that fluorinated compounds with an electron donating functional group can have very high absorption capabilities for carbon dioxide. However, in order to fully validate their potential in gas cleaning applications, the selectivity of such fluoro compounds for other gases in a flue gas stream should be studied in conjunction with a comprehensive process selection and design study.

References

1. AKUTSU, T., YAMAJI, Y., YAMAGUCHI, H., WATANABE, M., SMITH, R. L. & INOMATA, H. 2007. Interfacial tension between water and high pressure CO 2 in the presence of hydrocarbon surfactants. *Fluid phase equilibria,* 257**,** 163-168.

2. ALMEIDA, G., AZNAR, M. & TELLES, A. 1991. Uma nova forma de dependência com a temperatura do termo atrativo de equações de estado cúbicas. *RBE, Rev. Bras. Eng., Cad. Eng. Quim,* 8**,** 95.

3. AMEEN, J. & FURBUSH, S. A. 1971. *Acid gas removal from gas mixtures*. USA patent application. Jul 27, 1971.

4. ANDROULAKIS, I., KALOSPIROS, N. & TASSIOS, D. 1989. Thermophysical properties of pure polar and nonpolar compounds with a modified VdW-711 equation of state. *Fluid Phase Equilibria,* 45**,** 135-163.

5. ANNAMALAI, K., PURI, I. K. & JOG, M. A. 2010. *Advanced Thermodynamics Engineering*, Taylor & Francis.

6. BANKS, R. E., SMART, B. E. & TATLOW, J. C. 1994. *Organofluorine Chemistry: Principles and Commercial Applications*, Springer US.

7. BARTON, A. 1983. CRC Handbook on Solubility Parameters and Other Cohesion Phenomena. CRC Press, Boca Raton, Florida.

8. BELTRÁN, J. G. & SERVIO, P. 2008. Equilibrium studies for the system methane+ carbon dioxide+ neohexane+ water. *Journal of Chemical & Engineering Data,* 53**,** 1745-1749.

9. BENGESAI, P. 2016. *High Pressure Vapour-Liquid Equilibrium Measurements For R116 and Ethane with Perfluorohexane and Perfluorooctane* Master of Science in Engineering, University of Kwazulu Natal.

10. BENGESAI, P. N., NELSON, W. M., NAIDOO, P. & RAMJUGERNATH, D. 2016. Phase Equilibria for Perfluoroethane+(n-Perfluorohexane or n-Perfluorooctane) Binary Systems: Measurement and Modeling. *Journal of Chemical & Engineering Data,* 61**,** 3363-3370.

11. BUCKLIN, R. & SCHENDEL, R. 1984. Comparison of fluor solvent and selexol processes. *Energy Prog.;(United States),* 4.

12. BURKE, J. 1984. Solubility parameters: theory and application. *Book and Paper Group*.

13. BURR, B. & LYDDON, L. A comparison of physical solvents for acid gas removal. 87th Annual Gas Processors Association Convention, Grapevine, TX, March, 2008. 2-5.

14. CAGNIARD DE LA TOUR, C. 1822. Exposé de quelques resultats obtenus par l'action combinée de la chaleur et de la compression sur certaines liquides, tels que l'eau, l'éther sulfurique et l'essence de pétrole rectifié [Report on some results obtained by the combined action of heat and pressure on certain liquids, such as water, alcohol, sulfuric ether and petroleum distillate]. *Ann. Chim. et Phys.*

15. CALDERONE, M., RODIER, E., LETOURNEAU, J.-J. & FAGES, J. 2007. Solidification of Precirol® by the expansion of a supercritical fluid saturated melt: from the thermodynamic balance towards the crystallization aspect. *The Journal of Supercritical Fluids,* 42**,** 189-199.

16. CARRUTH, G. F. & KOBAYASHI, R. 1973. Vapor pressure of normal paraffins ethane through n-decane from their triple points to about 10 mm mercury. *Journal of Chemical and Engineering Data,* 18**,** 115-126.

17. CHRISTOV, M. & DOHRN, R. 2002. High-pressure fluid phase equilibria: experimental methods and systems investigated (1994–1999). *Fluid Phase Equilibria,* 202**,** 153-218.

18. COQUELET, C., CHAPOY, A. & RICHON, D. 2004. Development of a new alpha function for the Peng–Robinson equation of state: comparative study of alpha function models for pure gases (natural gas components) and water-gas systems. *International Journal of Thermophysics,* 25**,** 133-158.

19. COQUELET, C. & RICHON, D. 2009. Experimental determination of phase diagram and modeling: Application to refrigerant mixtures. *International journal of refrigeration,* 32**,** 1604-1614.

20. DIAS, A., CAÇO, A., COUTINHO, J., SANTOS, L., PINEIRO, M., VEGA, L., GOMES, M. C. & MARRUCHO, I. 2004. Thermodynamic properties of perfluoro-n-octane. *Fluid phase equilibria,* 225**,** 39-47.

21. DIAS, A. M., CARRIER, H., DARIDON, J. L., PAMIES, J. C., VEGA, L. F., COUTINHO, J. A. & MARRUCHO, I. M. 2006. Vapor-liquid equilibrium of carbon dioxide-perfluoroalkane mixtures: experimental data and SAFT modeling. *Industrial & Engineering Chemistry Research,* 45**,** 2341-2350.

22. DIAS, A. M., GONCALVES, C. M., CACO, A. I., SANTOS, L. M., PIÑEIRO, M. M., VEGA, L. F., COUTINHO, J. A. & MARRUCHO, I. M. 2005. Densities and vapor pressures of highly fluorinated compounds. *Journal of Chemical & Engineering Data,* 50**,** 1328-1333.

23. DOCTOR, R., MOLBURG, J. C., THIMMAPURAM, P., BERRY, G., LIVENGOOD, C. D. & JOHNSON, R. 1993. Gasification combined cycle: carbon dioxide recovery, transport, and disposal. *Energy Conversion and Management,* 34**,** 1113-1120.

24. DOHRN, R., BERTAKIS, E., BEHREND, O., VOUTSAS, E. & TASSIOS, D. 2007. Melting point depression by using supercritical CO 2 for a novel melt dispersion micronization process. *Journal of Molecular Liquids,* 131**,** 53-59.

25. DOHRN, R. & BRUNNER, G. 1995. High-pressure fluid-phase equilibria: experimental methods and systems investigated (1988–1993). *Fluid Phase Equilibria,* 106**,** 213-282.

26. DOHRN, R., FONSECA, J. M. & PEPER, S. 2012. Experimental methods for phase equilibria at high pressures. *Annual Review of Chemical and Biomolecular Engineering,* 3**,** 343-367.

27. DRESSELHAUS, M. & THOMAS, I. 2001. Alternative energy technologies. *Nature,* 414**,** 332-337.

28. DUCHEYNE, P., HEALY, K., HUTMACHER, D. E., GRAINGER, D. W. & KIRKPATRICK, C. J. 2015. *Comprehensive Biomaterials*, Elsevier Science.

29. EDENHOFER, O. & SOKONA, Y. 2011. IPCC special report on renewable energy sources and climate change mitigation. https://www.ipcc.ch/pdf/special-reports/srren/SRREN_FD_SPM_final.pdf.

30. FIGUEROA, J. D., FOUT, T., PLASYNSKI, S., MCILVRIED, H. & SRIVASTAVA, R. D. 2008. Advances in CO 2 capture technology—the US Department of Energy's Carbon Sequestration Program. *International Journal of Greenhouse Gas Control,* 2**,** 9-20.

31. FONSECA, J. M., DOHRN, R. & PEPER, S. 2011. High-pressure fluid-phase equilibria: experimental methods and systems investigated (2005–2008). *Fluid Phase Equilibria,* 300**,** 1-69.

32. FORNARI, R. E., ALESSI, P. & KIKIC, I. 1990. High pressure fluid phase equilibria: experimental methods and systems investigated (1978–1987). *Fluid Phase Equilibria,* 57**,** 1-33.

33. GANDE, E. 2016. *HIGH PRESSURE VAPOUR-LIQUID EQUILIBRIUM MEASUREMENT FOR PERFLUORINATED CHEMICALS USING A STATIC ANALYTICAL APPARATUS* MSc in Chemical Engineering University of Kwazulu Natal.

34. GASEM, K., GAO, W., PAN, Z. & ROBINSON, R. 2001. A modified temperature dependence for the Peng–Robinson equation of state. *Fluid phase equilibria,* 181**,** 113-125.

35. GIBBONS, R. M. & LAUGHTON, A. P. 1984. An equation of state for polar and non-polar substances and mixtures. *Journal of the Chemical Society, Faraday Transactions 2: Molecular and Chemical Physics,* 80**,** 1019-1038.

36. GIL, L., OTÍN, S. F., EMBID, J. M., GALLARDO, M. A., BLANCO, S., ARTAL, M. & VELASCO, I. 2008. Experimental setup to measure critical properties of pure and binary mixtures and their

densities at different pressures and temperatures: Determination of the precision and uncertainty in the results. *The Journal of Supercritical Fluids,* 44**,** 123-138.

37. GMEHLING, J. Ã. & KOLBE, B. Ã. 2012. *Chemical Thermodynamics for Process Simulation*, Wiley.

38. GOOD, D., FRANCISCO, J., JAIN, A. & WUEBBLES, D. 1998. Lifetimes and global warming potentials for dimethyl ether and for fluorinated ethers: CH3OCF3 (E143a), CHF2OCHF2 (E134), CHF2OCF3 (E125). *Journal of Geophysical Research: Atmospheres,* 103**,** 28181-28186.

39. GUI, X., TANG, Z. & FEI, W. 2011. Solubility of CO2 in alcohols, glycols, ethers, and ketones at high pressures from (288.15 to 318.15) K. *Journal of Chemical & Engineering Data,* 56**,** 2420-2429.

40. GUILBOT, P., VALTZ, A., LEGENDRE, H. & RICHON, D. 2000. Rapid on-line sampler-injector: a reliable tool for HT-HP sampling and on-line GC analysis. *Analusis,* 28**,** 426-431.

41. GWINNER, B., ROIZARD, D., LAPICQUE, F., FAVRE, E., CADOURS, R., BOUCOT, P. & CARRETTE, P.-L. 2006. CO2 capture in flue gas: semiempirical approach to select a potential physical solvent. *Industrial & Engineering Chemistry Research,* 45**,** 5044-5049.

42. HAGHTALAB, A., KAMALI, M., MAZLOUMI, S. & MAHMOODI, P. 2010. A new three-parameter cubic equation of state for calculation physical properties and vapor–liquid equilibria. *Fluid Phase Equilibria,* 293**,** 209-218.

43. HANSEN, C. M. 1967. The three-dimensional solubility parameter-key to paint component affinities: solvents, plasticizers, polymers, and resins. II. Dyes, emulsifiers, mutual solubility and compatibility, and pigments. III. Independent cal-culation of the parameter components. *Journal of Paint Technology,* 39**,** 505-510.

44. HANSON, J. R. 2001. *Functional Group Chemistry*, Royal Society of Chemistry.

45. HARMENS, A. & KNAPP, H. 1980. Three-parameter cubic equation of state for normal substances. *Industrial & Engineering Chemistry Fundamentals,* 19**,** 291-294.

46. HASZELDINE, R. & SMITH, F. 1951. 129. Organic fluorides. Part VI. The chemical and physical properties of certain fluorocarbons. *Journal of the Chemical Society (Resumed)***,** 603-608.

47. HEINTZ, Y. J. 2012. *Carbon dioxide capture from fuel gas streams under elevated pressures and temperatures using novel physical solvents.* University of Pittsburgh.

48. HEINTZ, Y. J., SEHABIAGUE, L., MORSI, B. I., JONES, K. L. & PENNLINE, H. W. 2008. Novel physical solvents for selective CO2 capture from fuel gas streams at elevated pressures and temperatures. *Energy & Fuels,* 22**,** 3824-3837.

49. HENNI, A., TONTIWACHWUTHIKUL, P. & CHAKMA, A. 2005. Solubilities of carbon dioxide in polyethylene glycol ethers. *The Canadian Journal of Chemical Engineering,* 83**,** 358-361.

50. HEYEN, G. Liquid and vapor properties from a cubic equation of state. Proc. 2nd Int. Conf. Phase Equilibrium Fluid Properties Chem., Berlin, 1980. DECHEMA Frankfurt/Main, 9-13.

51. HIGMAN, C. & VAN DER BURGT, M. 2003. *Gasification*, Elsevier Science.

52. HOEFLING, T., STOFESKY, D., REID, M., BECKMAN, E. & ENICK, R. M. 1992. The incorporation of a fluorinated ether functionality into a polymer or surfactant to enhance C02-solubility. *The Journal of Supercritical Fluids,* 5**,** 237-241.

53. HOUSSIN-AGBOMSON, D., COQUELET, C., RICHON, D. & ARPENTINIER, P. 2010. Equipment using a "static-analytic" method for solubility measurements in potentially hazardous binary mixtures under cryogenic temperatures. *Cryogenics,* 50**,** 248-256.

54. HURON, M.-J. & VIDAL, J. 1979. New mixing rules in simple equations of state for representing vapour-liquid equilibria of strongly non-ideal mixtures. *Fluid Phase Equilibria,* 3**,** 255-271.

55. KNAPP, H. 1982. *Vapor-liquid equilibria for mixtures of low-boiling substances*, Dechema.

56. KOHL, A. L. & NIELSEN, R. 1997. *Gas purification*, Gulf Professional Publishing.

57. KONTOGEORGIS, G. M. & FOLAS, G. K. 2009. *Thermodynamic Models for Industrial Applications: From Classical and Advanced Mixing Rules to Association Theories*, Wiley.

58. KOZMA, I. Z., KROK, P. & RIEDLE, E. 2005. Direct measurement of the group-velocity mismatch and derivation of the refractive-index dispersion for a variety of solvents in the ultraviolet. *JOSA B,* 22**,** 1479-1485.

59. KUTSHER, S. & SMITH, A. 1968. *Process for hydrogen sulfide removal from gas mixtures containing h2s and co2*. USA patent application.

60. LAY, E. N. 2009. Measurement and Correlation of Bubble Point Pressure in (CO2+ C6H6),(CO2+ CH3C6H5),(CO2+ C6H14), and (CO2+ C7H16) at Temperatures from (293.15 to 313.15) K. *Journal of Chemical & Engineering Data,* 55**,** 223-227.

61. LAZAROU, Y. G. & PAPAGIANNAKOPOULOS, P. 1999. Theoretical investigation of the thermochemistry of hydrofluoroethers. *Chemical Physics Letters,* 301**,** 19-28.

62. LAZZARONI, M. J., BUSH, D., BROWN, J. S. & ECKERT, C. A. 2005. High-pressure vapor– liquid equilbria of some carbon dioxide+ organic binary systems. *Journal of Chemical & Engineering Data,* 50**,** 60-65.

63. LI, Y.-H., DILLARD, K. H. & ROBINSON JR, R. L. 1981. Vapor-liquid phase equilibrium for carbon dioxide-n-hexane at 40, 80, and 120. degree. C. *Journal of Chemical and Engineering Data,* 26**,** 53-55.

64. LIU, D. & TOMASKO, D. L. 2007. Carbon dioxide sorption and dilation of poly (lactide-co-glycolide). *The Journal of Supercritical Fluids,* 39**,** 416-425.

65. LÓPEZ, J. A., TREJOS, V. M. & CARDONA, C. A. 2006. Objective functions analysis in the minimization of binary VLE data for asymmetric mixtures at high pressures. *Fluid phase equilibria,* 248**,** 147-157.

66. MACIEJEWSKI, A. 1990. The application of perfluoroalkanes as solvents in spectral, photophysical and photochemical studies. *Journal of Photochemistry and Photobiology A: Chemistry,* 51**,** 87-131.

67. MARTIN, A., KANT, M., KLEIN, H., JACKSTELL, R. & BELLER, M. 2007. Investigations on thermodynamic properties of hydroaminomethylation reaction mixtures at high pressures. *The Journal of Supercritical Fluids,* 42**,** 325-329.

68. MATHIAS, P. M. 1983. A versatile phase equilibrium equation of state. *Industrial & Engineering Chemistry Process Design and Development,* 22**,** 385-391.

69. MATHIAS, P. M. & COPEMAN, T. W. 1983. Extension of the Peng-Robinson equation of state to complex mixtures: evaluation of the various forms of the local composition concept. *Fluid Phase Equilibria,* 13**,** 91-108.

70. MELHEM, G. A., SAINI, R. & GOODWIN, B. M. 1989. A modified Peng-Robinson equation of state. *Fluid Phase Equilibria,* 47**,** 189-237.

71. MILLER, M. B., LUEBKE, D. R. & ENICK, R. M. 2010. CO2-philic oligomers as novel solvents for CO2 absorption. *Energy & Fuels,* 24**,** 6214-6219.

72. MURATA, J., YAMASHITA, S., AKIYAMA, M., KATAYAMA, S., HIAKI, T. & SEKIYA, A. 2002. Vapor pressures of hydrofluoroethers. *Journal of Chemical & Engineering Data,* 47**,** 911-915.

73. MUSTAFAEV, M., NAZIEV, Y. M. & KAGRAMANOV, M. 1995. The density of some perfluorocarbons in a wide range of state parameters. *Teplofizika Vysokikh Temperatur,* 33**,** 359-366.

74. NAIDOO, P. 2004. *High pressure vapour liquid equilibrium studies.* Doctor of philisophy (PhD), University of Kwazulu Natal.

75. NAIDOO, P., RAMJUGERNATH, D. & RAAL, J. D. 2008. A new high-pressure vapour–liquid equilibrium apparatus. *Fluid Phase Equilibria,* 269**,** 104-112.

76. NANDI, P., MOODLEY, S. & RAMJUGERNATH, D. 2013. Isothermal vapor–liquid equilibrium of R170+n-perfluorooctane at 308–338K: Measurement, equation of state modelling, and molecular simulation. *Fluid Phase Equilibria,* 344**,** 84-91.

77. NARASIGADU. 2011. *Design of a Static Micro-Cell for Phase Equilibrium Measurements : Measurements and Modelling* Doctor of Philosophy in Engineering, University of KwaZulu Nata.

78. NELSON, W. 2012. *SEPARATION OF TRICHLOROSILANE: MEASUREMENT, MODELLING AND SIMULATION.* Doctor of Philisophy, University of Kwazulu Natal.

79. NELSON, W. 2017. Measured solubility data for mixtures of ethylene and cyclohexane at pressures up to 8 MPa using a variable-volume sapphire cell. *J. Chem. Eng. Data,* In review.

80. NELSON, W. M., TEBBAL, Z., NAIDOO, P., NEGADI, L. & RAMJUGERNATH, D. 2016. High-pressure phase equilibria data for mixtures involving ethene and perfluoro-n-octane from 293 to 353K. *Fluid Phase Equilibria,* 408**,** 33-37.

81. OLAJIRE, A. A. 2010. CO 2 capture and separation technologies for end-of-pipe applications– a review. *Energy,* 35**,** 2610-2628.

82. OLIVER, G. D., BLUMKIN, S. & CUNNINGHAM, C. 1951. Some Physical Properties of Hexadecafluoroheptane1a, 1b. *Journal of the American Chemical Society,* 73**,** 5722-5725.

83. OLIVER, G. D. & GRISARD, J. 1951. Some Thermodynamic Properties of Hexadecafluoroheptane1. *Journal of the American Chemical Society,* 73**,** 1688-1690.

84. ORBEY, H. & SANDLER, S. I. 1998. *Modeling vapor-liquid equilibria: cubic equations of state and their mixing rules*, Cambridge University Press.

85. PENG, D.-Y. & ROBINSON, D. B. 1976. A new two-constant equation of state. *Industrial & Engineering Chemistry Fundamentals,* 15**,** 59-64.

86. PENNLINE, H. W., LUEBKE, D. R., JONES, K. L., MYERS, C. R., MORSI, B. I., HEINTZ, Y. J. & ILCONICH, J. B. 2008. Progress in carbon dioxide capture and separation research for gasification-based power generation point sources. *Fuel Processing Technology,* 89**,** 897-907.

87. PRAUSNITZ, J. M., LICHTENTHALER, R. N. & DE AZEVEDO, E. G. 1998. *Molecular thermodynamics of fluid-phase equilibria*, Pearson Education.

88. PRIVAT, R. & JAUBERT, J.-N. 2012. *Thermodynamic Models for the Prediction of Petroleum-Fluid Phase Behaviour*, INTECH Open Access Publisher.

89. RAAL, J. D. & MÜHLBAUER, A. 1997. *Phase Equilibria: Measurement & Computation*, Taylor & Francis.

90. RAINWATER, J. C. 2001. An asymptotic expression for the critical-region "bird's beak" isotherm and adjacent isotherms on the vapor–liquid phase diagram of a simple binary mixture. *Fluid phase equilibria,* 183**,** 41-51.

91. RAVEENDRAN, P. & WALLEN, S. L. 2002. Cooperative CH---O Hydrogen Bonding in CO2-Lewis Base Complexes: Implications for Solvation in Supercritical CO2. *Journal of the American Chemical Society,* 124**,** 12590-12599.

92. RAYER, A. V., HENNI, A. & TONTIWACHWUTHIKUL, P. 2012. High pressure physical solubility of carbon dioxide (CO2) in mixed polyethylene glycol dimethyl ethers (Genosorb 1753). *The Canadian Journal of Chemical Engineering,* 90**,** 576-583.

93. RENON, H. & PRAUSNITZ, J. 1969. Estimation of parameters for the NRTL equation for excess Gibbs energies of strongly nonideal liquid mixtures. *Industrial & Engineering Chemistry Process Design and Development,* 8**,** 413-419.

94. RENON, H. & PRAUSNITZ, J. M. 1968. Local compositions in thermodynamic excess functions for liquid mixtures. *AIChE Journal,* 14**,** 135-144.

95. RIESS, J. G. 2001. Oxygen Carriers ("Blood Substitutes") Raison d'Etre, Chemistry, and Some Physiology Blut ist ein ganz besondrer Saft 1. *Chemical Reviews,* 101**,** 2797-2920.

96. RIZVI, S. S. H. 2010. *Separation, Extraction and Concentration Processes in the Food, Beverage and Nutraceutical Industries*, Elsevier Science.

97. ROBB, I. D. 2012. *Specialist Surfactants*, Springer Netherlands.

98. SADUS, R. & YOUNG, C. 1985. Phase behaviour of binary n-alkanenitrile and n-alkane, and nitromethane and alkane mixtures. *Fluid phase equilibria,* 22**,** 225-229.

99. SADUS, R. J. 2012. *High Pressure Phase Behaviour of Multicomponent Fluid Mixtures*, Elsevier Science.

100. SADUS, R. J., YOUNG, C. L. & SVEJDA, P. 1988. Application of hard convex body and hard sphere equations of state to the critical properties of binary mixtures. *Fluid phase equilibria,* 39**,** 89-99.

101. SAFFARI, H. & ZAHEDI, A. 2013. A new alpha-function for the Peng-Robinson equation of state: application to natural gas. *Chinese Journal of Chemical Engineering,* 21**,** 1155-1161.

102. SANDLER, S. I. 1994. *Models for thermodynamic and phase equilibria calculations*, Dekker.

103. SCHWARTZENTRUBER, J., RENON, H. & WATANASIRI, S. 1990. K-values for non-ideal systems: An easier way. *Chemical Engineering,* 97**,** 118.

104. SENGERS, J. L. 1986. Dilute mixtures and solutions near critical points. *Fluid Phase Equilibria,* 30**,** 31-39.

105. SHAFIEE, S. & TOPAL, E. 2009. When will fossil fuel reserves be diminished? *Energy policy,* 37**,** 181-189.

106. SIGMA ALDRICH. 2016a. *Perfluorononane* [Online]. [Accessed 09 Dec 2016].

107. SIGMA ALDRICH. 2016b. *Perfluorooctane* [Online]. [Accessed 09 Dec 2016].

108. SIMONS, J. H. 2012. *Fluorine Chemistry*, Elsevier Science.

109. SIMS, R. E., ROGNER, H.-H. & GREGORY, K. 2003. Carbon emission and mitigation cost comparisons between fossil fuel, nuclear and renewable energy resources for electricity generation. *Energy policy,* 31**,** 1315-1326.

110. SINNOTT, R. 2005. *Chemcal Engineering design*, Elsevier Butterworth-Heinemann.

111. SMYTH, C. & ENGEL, E. 1929. Molecular orientation and the partial vapor pressures of binary mixtures. I. Systems composed of normal liquids. *Journal of the American Chemical Society,* 51**,** 2646-2660.

112. SOAVE, G. 1972. Equilibrium constants from a modified Redlich-Kwong equation of state. *Chemical Engineering Science,* 27**,** 1197-1203.

113. SOAVE, G. 1984. Improvement of the van der Waals equation of state. *Chemical engineering science,* 39**,** 357-369.

114. SOAVE, G. 1993. Improving the Treatment of Heavy Hydrocarbons by the SRK EOS. *Fluid Phase Equilibria,* 84**,** 339-342.

115. SOO, C.-B. 2011. *Experimental thermodynamic measurements of biofuel-related associating compounds and modeling using the PC-SAFT equation of state.* École Nationale Supérieure des Mines de Paris.

116. SOO, C.-B., THÉVENEAU, P., COQUELET, C., RAMJUGERNATH, D. & RICHON, D. 2010. Determination of critical properties of pure and multi-component mixtures using a "dynamic–synthetic" apparatus. *The Journal of Supercritical Fluids,* 55**,** 545-553.

117. STOCK, N. L., ELLIS, D. A., DELEEBEECK, L., MUIR, D. C. & MABURY, S. A. 2004. Vapor pressures of the fluorinated telomer alcohols limitations of estimation methods. *Environmental Science & Technology,* 38**,** 1693-1699.

118. STRYJEK, R. & VERA, J. 1986. PRSV: An improved Peng—Robinson equation of state for pure compounds and mixtures. *The Canadian Journal of Chemical Engineering,* 64**,** 323-333.

119. TAYLOR, B. N. 2009. *Guidelines for Evaluating and Expressing the Uncertainty of NIST Measurement Results (rev*, DIANE Publishing.

120. TAYLOR, B. N. & KUYATT, C. E. 1994. *Guidelines for evaluating and expressing the uncertainty of NIST measurement results*, US Department of Commerce, Technology Administration, National Institute of Standards and Technology Gaithersburg, MD.

121. THOMAS, G. & YOUNG, S. 1895. CXII.—The vapour pressures, specific volumes and critical constants of normal hexane. *Journal of the Chemical Society, Transactions,* 67**,** 1071-1084.

122. TOCHIGI, K., NAMAE, T., SUGA, T., MATSUDA, H., KURIHARA, K., DOS RAMOS, M. C. & MCCABE, C. 2010. Measurement and prediction of high-pressure vapor–liquid equilibria for binary mixtures of carbon dioxide+ n-octane, methanol, ethanol, and perfluorohexane. *The Journal of Supercritical Fluids,* 55**,** 682-689.

123. TREBBLE, M. & BISHNOI, P. 1987. Development of a new four-parameter cubic equation of state. *Fluid Phase Equilibria,* 35**,** 1-18.

124. TSHIBANGU, M. M. 2015. *INVESTIGATION OF PERFLUOROCARBONS AS POTENTIAL PHYSICAL SOLVENTS FOR FLUE GAS CLEANING* Doctor of Philosophy University of Kwazulu Natal.

125. TSHIBANGU, M. M., VALTZ, A., NARASIGADU, C., COQUELET, C. & RAMJUGERNATH, D. 2014. Vapor–liquid equilibrium (VLE) data and thermodynamic modeling for binary systems containing perfluorobutane (R610) with carbon monoxide or nitric oxide at (293, 313, and 333) K. *Journal of Chemical & Engineering Data,* 59**,** 346-354.

126. TWU, C. H., BLUCK, D., CUNNINGHAM, J. R. & COON, J. E. 1991. A cubic equation of state with a new alpha function and a new mixing rule. *Fluid Phase Equilibria,* 69**,** 33-50.

127. TWU, C. H., SIM, W. D. & TASSONE, V. 2002. Getting a handle on advanced cubic equations of state. *Chemical Engineering Progress,* 98**,** 58-65.

128. VALTZ, A., COURTIAL, X., JOHANSSON, E., COQUELET, C. & RAMJUGERNATH, D. 2011. Isothermal vapor–liquid equilibrium data for the carbon dioxide (R744)+ decafluorobutane (R610) system at temperatures from 263 to 353K. *Fluid Phase Equilibria,* 304**,** 44-51.

129. VAN NESS, H. C. 2015. *Classical thermodynamics of non-electrolyte solutions*, Elsevier.

130. WAGNER, Z. & WICHTERLE, I. 1987. High-pressure vapour—liquid equilibrium in systems containing carbon dioxide, 1-hexene, and n-hexane. *Fluid Phase Equilibria,* 33**,** 109-123.

131. WANG, J. & OBER, C. K. 1999. Solid state crystalline and liquid crystalline structure of semifluorinated 1-bromoalkane compounds. *Liquid crystals,* 26**,** 637-648.

132. WHITE, C. M., STRAZISAR, B. R., GRANITE, E. J., HOFFMAN, J. S. & PENNLINE, H. W. 2003. Separation and capture of CO2 from large stationary sources and sequestration in geological formations—coalbeds and deep saline aquifers. *Journal of the Air & Waste Management Association,* 53**,** 645-715.

133. WILLIAMS-WYNN, M. D. 2016. *APPLICATIONS OF FLUOROCARBONS FOR SUPERCRITICAL EXTRACTION IN THE PETROLEUM INDUSTRY* Doctor of Philosophy, University of Kwazulu Natal.

134. WILLIAMS-WYNN, M. D., NAIDOO, P. & RAMJUGERNATH, D. 2016. Isothermal vapour-liquid equilibrium data for the binary systems of (CHF 3 or C 2 F 6) and n-heptane. *The Journal of Chemical Thermodynamics,* 102**,** 237-247.

135. WILSON, G. 1964. Vapor-liquid equilibria, correlation by means of a modified Redlich-Kwong equation of state. *Advances in Cryogenic Engineering.* Springer.

136. WONG, D. S. H. & SANDLER, S. I. 1992. A theoretically correct mixing rule for cubic equations of state. *AIChE Journal,* 38**,** 671-680.

137. XU, Y. 1991. *Thermodynamic Investigations: 1, Gases and Vapors in Liquids, 2, Calorimetric Studies*.

138. YARBOROUGH, L. & VOGEL, J. L. A new system for obtaining vapor and liquid sample analyses to facilitate the study of multicomponent mixtures at elevated pressures. Chem. Eng. Symp. Ser, 1967. 1-9.

139. YOUNG, A. F., PESSOA, F. L. & RUIZ AHÓN, V. R. 2016. Comparison of 20 Alpha Functions Applied in the Peng-Robinson EoS for Vapor Pressure Estimation. *Industrial & Engineering Chemistry Research*.

140. YU, J.-M. & LU, B. C.-Y. 1987. A three-parameter cubic equation of state for asymmetric mixture density calculations. *Fluid Phase Equilibria,* 34**,** 1-19.

141. YU, J., WANG, S. & TIAN, Y. 2006. Experimental determination and calculation of thermodynamic properties of CO 2+ octane to high temperatures and high pressures. *Fluid Phase Equilibria,* 246**,** 6-14.

142. ZAMAN, M. & LEE, J. H. 2013. Carbon capture from stationary power generation sources: a review of the current status of the technologies. *Korean Journal of Chemical Engineering,* 30**,** 1497-1526.

143. ZAWACKI, T., DUNCAN, D. & MACRISS, R. 1981. Process optimized for high pressure gas cleanup. *Hydrocarbon Process.;(United States),* 60.

144. ZHANG, H., WU, J. & SHEN, Z. 2011. Radiative forcing and global warming potential of perfluorocarbons and sulfur hexafluoride. *Science China Earth Sciences,* 54**,** 764-772.

Appendix A

A. Temperature and pressure calibration data

A.1 Temperature

Temperature calibrations were performed for the two temperature probes which were used to measure the temperature of the contents of the equilibrium cell. The probes were designated probe 204 and probe 205. The calibration was performed for a temperature range of (258.15 – 438.15) K, using the procedure outlined in Chapter 5. Published herein are the graphs of the first order calibration polynomials and the plots depicting the errors induced by the calibration polynomials.

Table A-1: Calibration polynomials for probes 204 and 205.

Probe 204 (Top)	$y = 0.9993x - 0.8269$ $R^2 = 1.000$
Probe 205 (Bottom)	$y = 0.9984x - 0.7713$ $R^2 = 1.000$
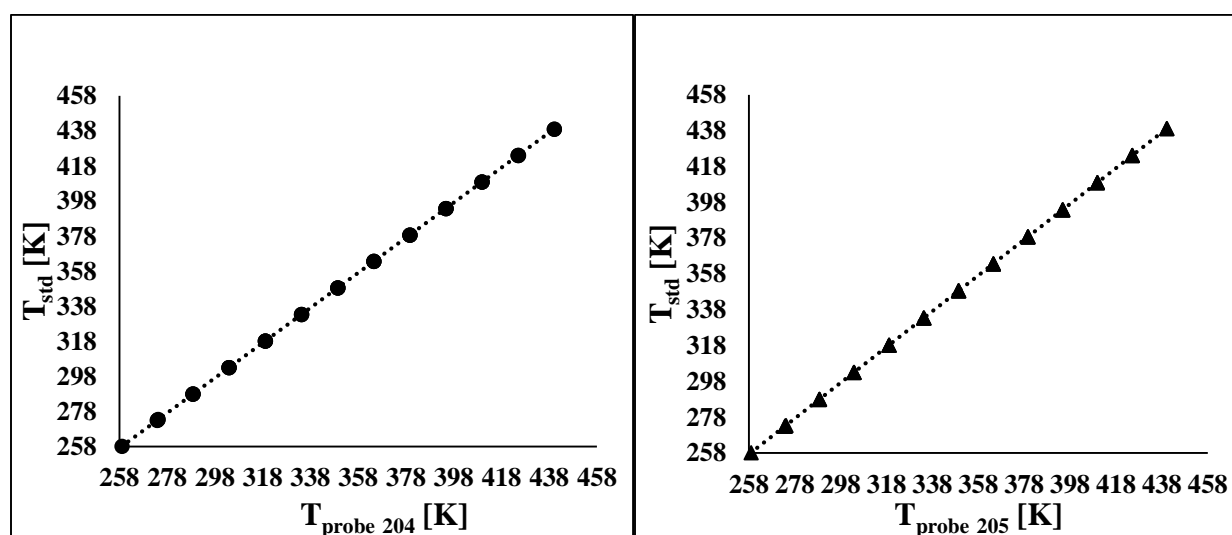
Figure A-1: Calibration charts for the temperature probes. (●) Top, (▲) Bottom.
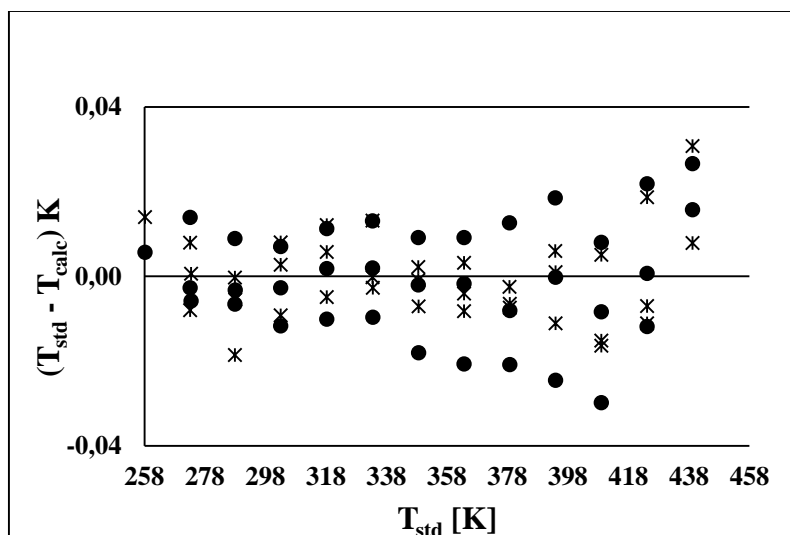
Figure A-2: Errors induced by the calibration polynomials for the temperature probes. (●) Top, (*) Bottom.

A.2 Pressure

The pressure calibration was conducted for a (0 – 25) MPa pressure transducer over a pressure range of (0 – 12) MPa. The calibration data was regressed using a first order polynomial, generating residuals which were less than 0.002 MPa.

Table A-2: Pressure calibration polynomial.

Pressure transducer	$y = 1.000x - 0.010$ $R^2 = 1.000$
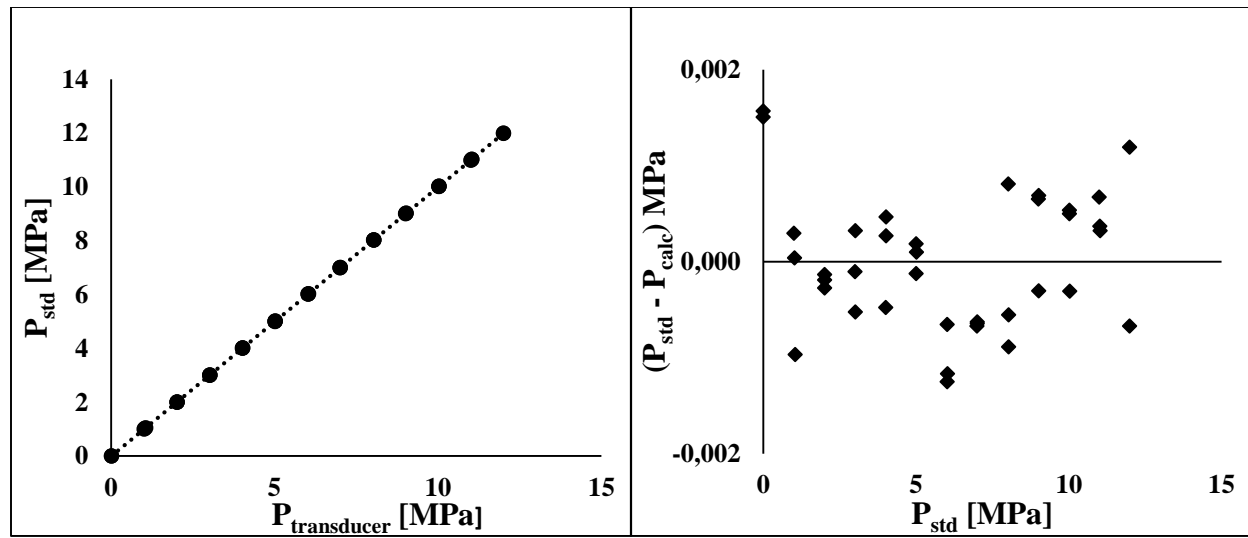
Figure A-3: Pressure calibration plots. (**Left**) Linear calibration (**Right**) Errors induced by the calibration polynomial.

Appendix B

B. Gas chromatography TCD calibration data

For the TCD calibration polynomial of a component to be effective, the samples of the respective components should ideally have peak areas which are within the calibration range. If the peak areas generated from sample analysis reside below or above the calibration range, then extrapolation of the calibration polynomial would be required. However, this may result in excessive errors when the number of moles of the samples is evaluated from the generated calibration polynomial in-conjunction with the sample peak areas. In this work, the samples obtained did not all adhere to the calibration limits thus tests were performed to verify that the extrapolation of the pure component calibration could be undertaken without incurring excessive errors. This was achieved through generating calibration polynomials for the pure components in conjunction with those for the mixtures of pure components with other suitable substances. The aforementioned procedure was discussed in Chapter 5 and 7.

Published in this Appendix is the TCD calibration data of the pure component carbon dioxide and that of the carbon dioxide + Helium mixture, including the calculation of the error incurred when the pure component calibration is extrapolated to the smaller peak area region. Only carbon dioxide data was used to demonstrate the calculation of the deviation between the two calibration polynomials since the procedure used was identical to that which was used for the other components.

Table B-1: Pure carbon dioxide TCD calibration data (250 μL syringe).

Experimental Moles	Peak area	Calculated moles	Δ moles	Δ moles$/Exp\ moles$
9.97E-06	17 781 506.60	1.01E-05	1.21E-07	0.012
9.97E-06	17 664 427.20	1.00E-05	5.57E-08	0.006
9.97E-06	17 553 040.10	9.96E-06	-6.73E-09	-0.001
9.96E-06	17 482 070.00	9.92E-06	-3.97E-08	-0.004
9.96E-06	17 511 592.20	9.94E-06	-2.19E-08	-0.002
7.97E-06	14 038 610.30	8.00E-06	2.86E-08	0.004
7.97E-06	13 985 274.00	7.97E-06	-1.42E-09	0.000
7.97E-06	13 949 282.90	7.95E-06	-2.11E-08	-0.003
7.96E-06	13 887 534.40	7.91E-06	-4.21E-08	-0.005
7.96E-06	13 919 068.50	7.93E-06	-2.45E-08	-0.003
5.97E-06	10 355 883.20	5.94E-06	-2.90E-08	-0.005
5.97E-06	10 229 648.80	5.87E-06	-9.87E-08	-0.017
5.97E-06	10 388 002.40	5.96E-06	-1.03E-08	-0.002
5.97E-06	10 276 437.40	5.90E-06	-7.24E-08	-0.012
5.97E-06	10 369 068.80	5.95E-06	-2.08E-08	-0.003
3.98E-06	6 918 834.80	4.03E-06	4.60E-08	0.012
3.98E-06	6 852 927.20	3.99E-06	6.97E-09	0.002
3.98E-06	6 973 497.30	4.06E-06	7.43E-08	0.019
3.98E-06	6 941 330.20	4.04E-06	5.59E-08	0.014

Calibration polynomial - $[\mathbf{y = 5.58E - 13x + 1.69E - 07}]$

$\mathbf{R^2 = 0.9994}$

Carbon dioxide was mixed with Helium gas, generating a mixture with a carbon dioxide mole fraction of 0.35. This then allowed the direct injection of smaller amounts of carbon dioxide into the GC, which could not be achieved using the available gas syringes. Helium was also the carrier gas for the GC. Thus no peaks of the gas were generated as it eluted the TCD, and so the moles and peak areas tabulated in Table B-2 are for only carbon dioxide.

Table B-2: Carbon dioxide + helium mixture calibration data (250μL syringe).

Experimental Moles	Peak area	Calculated moles	Δ moles	Δ moles/$Exp\ moles$
3.47E-06	5 904 986.20	3.46E-06	-1.41E-08	-0.004
3.47E-06	5 932 067.30	3.47E-06	1.88E-09	0.001
3.47E-06	5 912 779.50	3.46E-06	-9.18E-09	-0.003
2.77E-06	4 743 901.40	2.78E-06	9.65E-09	0.003
2.77E-06	4 742 316.40	2.78E-06	8.73E-09	0.003
2.77E-06	4 763 703.30	2.79E-06	2.11E-08	0.008
2.08E-06	3 509 649.50	2.07E-06	-1.19E-08	-0.006
2.08E-06	3 502 050.00	2.06E-06	-1.66E-08	-0.008
2.08E-06	3 550 789.80	2.09E-06	1.17E-08	0.006
1.39E-06	2 336 462.30	1.39E-06	1.92E-09	0.001
1.39E-06	2 324 955.80	1.38E-06	-4.82E-09	-0.003
1.39E-06	2 335 806.60	1.39E-06	1.61E-09	0.001

Calibration polynomial - $[\mathbf{y = 5.79E - 13x + 3.64E - 08}]$

$\mathbf{R^2 = 0.9997}$

Both calibration polynomials could be used interchangeably, depending on the carbon dioxide peak areas of the samples. However as was stated in Chapter 7, only the pure component calibration was utilised in this work. This was achieved through taking into account the deviation incurred by the pure component calibration when it was extrapolated to the lower peak areas and using the aforementioned error in calculating the standard compositional uncertainty. This was however done for only the points which were not bound by the calibration range. The deviation of the mixture calibration from that of the pure component was evaluated as follows:

    I.   Multiplying the peak areas from the samples obtained through the direct injection of the mixture by the gradients of both calibration polynomials, thus generating the number of moles of the samples. (The intercept is not used due to the assumed presence of dead volume within the syringe)

II.   Evaluating the relative deviation between the moles calculated from the two calibration polynomials.

The calculation of the deviation mentioned above is tabulated in Table B-3.

Table B-3: Calculation of the deviation between the pure component and mixture calibration polynomials.

Peak area	Peak area $\times$ (5.58E-13)	Peak area $\times$ (5.79E-13)	$\left\|(n_1 - n_2)/n_1\right\|$
	n_1	n_2	
5 904 986.20	3.29E-06	3.42E-06	0.04
5 932 067.30	3.31E-06	3.43E-06	0.04
5 912 779.50	3.30E-06	3.42E-06	0.04
4 743 901.40	2.65E-06	2.75E-06	0.04
4 742 316.40	2.64E-06	2.75E-06	0.04
4 763 703.30	2.66E-06	2.76E-06	0.04
3 509 649.50	1.96E-06	2.03E-06	0.04
3 502 050.00	1.95E-06	2.03E-06	0.04
3 550 789.80	1.98E-06	2.06E-06	0.04
2 336 462.30	1.30E-06	1.35E-06	0.04
2 324 955.80	1.30E-06	1.35E-06	0.04
2 335 806.60	1.30E-06	1.35E-06	0.04

The deviations calculated in Tables B-1 and B-3 were used in the evaluation of the standard uncertainty of the calibration polynomials ($u_{corr}(n_i)$), which is a component in the calculation of the overall combined expanded uncertainty in molar composition.

Appendix C

C. Estimation of experimental uncertainty

For a measured variable to be considered complete, it should be accompanied by its uncertainty, which is defined as the range in which the true value of the measurand has the highest probability of residing. In this work, uncertainties for temperature, pressure and composition were computed as per the instructions published by Soo et al. (2010) and Nelson (2012), which are specific for HPVLE measurements and these were in turn generated through the guidelines formulated by the international committee of weights and measures (CIPM). These guidelines were adopted by the National Institute of Standards and Technology (NIST) in order to foster an international agreement on the expression of uncertainty in measurement (Taylor and Kuyatt, 1994; Taylor, 2009).

The CIPM approach recognised that the uncertainty/ (standard uncertainty) of the measurand had to consist of all non-negligible possible components of uncertainty. These components were then grouped into two broad categories, namely Type A and B, based on the method used to compute their values (Taylor and Kuyatt, 1994).

The following equation then correlates the standard combined uncertainty

$$u_c(\theta) = \pm \sqrt{\sum_i u_c(\theta)^2} \qquad (C\text{-}1)$$

Where $u_c(\theta)$ is defined as the standard uncertainty in (θ).

The evaluation of equation (C-1) can be carried out through designating the uncertainty components as Type A, resulting in a statistical evaluation which is conducted through the equation:

$$u_i(\theta) = \frac{\sigma}{\sqrt{N_{rp}}} \qquad (C\text{-}2)$$

Where N_{rp} is the number of repeated data points and σ is the standard deviation. When the combined standard uncertainty components are classified as Type B, they will be considered to have an equal likelihood of residing anywhere within the distribution and are evaluated as follows:

$$u_i(\theta) = \frac{b}{\sqrt{3}} \qquad \text{(C-3)}$$

In this work, the value of b is set to the maximum error in the calibration polynomial. For all the measurements carried out in this work, the measurand is believed to lie within an interval having a confidence level of approximately 95%. Thus the combined expanded standard uncertainty is calculated with a coverage factor (K) of 2 as follows

$$U_c(\theta) = Ku_c(\theta) \qquad \text{(C-4)}$$

C.1 Temperature and pressure

The following correlation gives the combined standard uncertainty in temperature:

$$u_c(T) = \pm\sqrt{u_{rep}(T)^2 + u_{calib}(T)^2} \qquad \text{(C-5)}$$

where the components of the combined standard uncertainty are represented by the standard uncertainty in repeatability and the calibration respectively. The former is calculated through equation C-2 while the latter is classified as Type B and is evaluated by the following correlation:

$$u_{calib}(T) = \pm\sqrt{u_{corr}(T)^2 + u_{std}(T)^2} \qquad \text{(C-6)}$$

Where $u_{corr}(T)$ is the standard uncertainty due to the calibration polynomial and $u_{std}(T)$ is the standard uncertainty of the standard temperature probe. Both uncertainties are classified as Type B.

The standard uncertainty in pressure is also evaluated in a similar manner as shown in the following correlation:

$$u_c(P) = \pm\sqrt{u_{corr}(P)^2 + u_{std}(P)^2 + u_{atm}(P)^2 + u_{rep}(P)^2} \qquad (C\text{-}7)$$

Where the standard uncertainties in (i) calibration polynomial, (ii) standard pressure transducer, (iii) barometer and (iv) repeatability are represented by $u_{corr}(P)$, $u_{std}(P)$, $u_{atm}(P)$ and $u_{rep}(P)$ respectively. All the uncertainty components are classified as Type B, with the exception of the standard uncertainty in repeatability.

C.2 Uncertainties in composition

In this work, two sets of apparatus were employed, and the compositional uncertainty were calculated differently for each apparatus as highlighted in the following sections. A detailed discussion of the procedures used in computing compositional uncertainty was published in the works of Soo et al. (2010) and Nelson (2012), thus for a comprehensive study, the reader is directed to the works above.

Static analytic apparatus

The standard uncertainty in composition for the data measured on this particular equipment is dependent on the uncertainty in repeatability of the measurements and the uncertainty resulting from the TCD calibration as follows:

$$u_c(x_i) = \pm\sqrt{u_{rep}(x_i)^2 + u_{calib}(x_i)^2} \qquad (C\text{-}8)$$

When using the direct injection method for TCD calibration, as was done in this work, $u_{calib}(x_i)$ is determined from the standard uncertainty in the number of moles of both components in the mixture and the respective mole fractions $\left(x_i = \dfrac{n_i}{n_i+n_j}\right)$, as follows:

$$u_{calib}(x_i) = \sqrt{\left(\frac{n_j}{(n_i + n_j)}\, u(n_i)\right)^2 + \left(\frac{n_i}{(n_i + n_j)}\, u(n_j)\right)^2} \qquad (C\text{-}9)$$

Where the standard uncertainty in number of moles for the gaseous component is computed through the use of standard uncertainties in the compositional calibration polynomial and the

standard uncertainties in the number of moles of gas injected into the GC during TCD calibration as follows:

$$u(n_i) = \sqrt{u_{corr}(n_i)^2 + u_{ig}(n_i)^2} \qquad \text{(C-10)}$$

The standard uncertainty in the number of moles for the liquid component is also evaluated in a similar manner:

$$u(n_j) = \sqrt{u_{corr}(n_j)^2 + u_{id}(n_j)^2} \qquad \text{(C-11)}$$

The standard uncertainty in the number of moles of injected gas ($u_{ig}(n_i)$) and liquid ($u_{id}(n_j)$) are evaluated through the law of propagation of error as shown in equations (C-12) and (C-13):

$$u_{ig}(n_i) = \sqrt{\frac{u(P)^2}{P} + \frac{u(V_g)^2}{V} + \frac{u(T)^2}{T}} \qquad \text{(C-12)}$$

$$u_{id}(n_j) = \sqrt{\frac{u(P)^2}{P} + \frac{u(V_l)^2}{V}} \qquad \text{(C-13)}$$

Where the standard uncertainties in pressure, volume and temperature are evaluated as follows

$\mathbf{u(P)}$ – Treating the uncertainty in the Mensor CPC 3000 baramoter (0.025%) as Type B.

$\mathbf{u(V)}$ – Assuming the human error which is inherent in the operation of the GC syringes is 2% and including the aforementioned error in the evaluation of the Type B standard uncertainty.

$\mathbf{u(T)}$ – The maximum possible temperature fluctuation that could occur due to the handling of the syringe was assumed to be 2 K and the standard uncertainty was then evaluated as Type B.

The other component necessary for the calculation of the standard uncertainty in the number of moles for both components is the standard uncertainty due to the calibration polynomials which is evaluated as follows:

$$u_{corr}(n_i) = n_i \frac{\left(\left|\frac{n_{i,}\text{True} - n_{i,}\text{Calc}}{n_{i,}\text{True}}\right|\right)_{max}}{\sqrt{3}} \qquad \text{(C-15)}$$

Static synthetic apparatus with a variable volume cell

The standard uncertainty in composition for this particular apparatus is dependent on the standard uncertainty of the Ohaus mass balance, the masses of the respective components and their mole fractions as follows:

$$u_c(x_i) = x_i x_j \sqrt{\frac{u(m_1)^2}{m_i} + \frac{u(m_1)^2}{m_j}} \tag{C-16}$$

where $u(m_1)$ is the standard uncertainty of the mass balance which is treated as Type B.

C.3 Sample calculation for the static analytic apparatus

In order to demonstrate the actual calculation of the compositional uncertainty in this work, data from the carbon dioxide (1) + perfluorononane (2) binary system, measured at 273.15 K is employed. This system was chosen because it exhibited the lowest compositional uncertainty, particularly in the vapour phase. Table C-1 displays the data for points measured in the liquid and vapour phase at 1.8 MPa respectively. The peak areas for both the gas and the PFC which are tabulated in Table C-1 had already been subjected to their calibration polynomials, thus generating the moles and mole fractions.

Table C-1: Sample data for the carbon dioxide (1) + perfluorononane (2) system measured at an average temperature and pressure of 273.15 K and 1.8 MPa**.**

			Liquid samples			
Peak area (CO_2)	Peak area (C_9F_{20})	$CO_2(n_1)$	$C_9F_{20}(n_2)$	x_1	x_2
2 773 613.10	11 501 183.10	1.55E-06	1.59E-06	0.493	0.507
2 545 201.60	11 002 864.40	1.42E-06	1.52E-06	0.482	0.518
2 524 065.90	10 787 257.70	1.41E-06	1.49E-06	0.485	0.515
2 515 206.60	10 514 704.10	1.40E-06	1.46E-06	0.491	0.509
2 439 815.70	10 428 292.60	1.36E-06	1.44E-06	0.485	0.515
2 490 420.00	10 792 697.30	1.39E-06	1.49E-06	0.482	0.518
$\overline{n_1}$ = 1.42E-06		$\overline{n_2}$ = 1.50E-06		$\overline{x_1}$ = 0.4864	$\overline{x_2}$ = 0.514

			Vapour samples			
Peak area (CO_2)	Peak area (C_9F_{20})	$CO_2(n_1)$	$C_9F_{20}(n_2)$	y_1	y_2
11 096 634.20	19 398.90	6.19E-06	2.69E-09	0.99957	0.0004
11 060 705.60	20 984.00	6.17E-06	2.90E-09	0.99953	0.0005
11 059 456.70	20 614.20	6.17E-06	2.85E-09	0.99954	0.0005
11 041 577.70	20 658.20	6.16E-06	2.86E-09	0.99954	0.0005
11 030 977.00	22 112.50	6.15E-06	3.06E-09	0.99950	0.0005
11 002 345.40	21 819.80	6.14E-06	3.02E-09	0.99951	0.0005
10 995 708.20	20 778.80	6.13E-06	2.88E-09	0.99953	0.0005
10 987 512.60	19 090.00	6.13E-06	2.64E-09	0.99957	0.0004
$\overline{n_1}$ = 6.16E-06		$\overline{n_2}$ = 2.86E-09		$\overline{y_1}$ = 0.99953	$\overline{y_2}$ = 0.0005

The combined expanded uncertainty in the vapour phase was used for the demonstration since this phase had the lowest compositional uncertainty. The data utilised in the sample calculation is obtained from Table C-1 and Appendix B.

For carbon dioxide in the vapour phase the standard uncertainty in the number of moles is evaluated through equation (C-12) as follows:

$$u_{1g}(n_1) = \bar{n}_1 \sqrt{\left(0.00014/1.0132\right)^2 + \left(0.012V/V\right)^2 + \left(0.017/298.83\right)^2}$$

$$u_{1g}(n_1) = 0.012 n_i$$

$$= 0.012 \times 6.16\text{E-}06$$
$$= 7.39\text{E-}08$$

The value of $u_{corr}(n_1)$ used is dependent on whether the carbon dioxide peak areas were perfectly bound by the pure component calibration polynomial or not. In this case, the peak areas of carbon dioxide are within the range, thus $u_{corr}(n_1)$ is dependent on the maximum error induced by the pure component calibration polynomial as follows:

$$u_{corr}(n_1) = \frac{(6.16\text{E} - 06)\,(0.02)}{\sqrt{3}}$$

$$= 7.11\text{E-}08$$

Therefore equation (C-10) reduces to,

$$u(n_1) = \sqrt{(7.11\text{E} - 08^2) \times (7.39\text{E} - 08^2)}$$

$$= 1.02589\text{E-}07$$

For the second component, which is perfluorononane, the generated calibration peak areas were below the calibration range, thus extrapolation of the calibration polynomial was required. This then meant that the value of $u_{corr}(n_2)$ used was generated through the use of the deviation of the pure perfluorononane calibration polynomial from that of the perfluorononane + hexane mixture. The deviation was then used to compute the standard uncertainty in the number of moles of perfluorononane as follows:

$$u_{corr}(n_2) = \frac{(2.86\text{E} - 09)(0.018)}{\sqrt{3}}$$

$$= 2.97\text{E-}11$$

$$u_{1d}(n_2) = (2.86\text{E} - 09)\sqrt{\left(0.012V/V\right)^2 + \left(0.00014/1.0132\right)^2}$$

$$= 3.43\text{E-}11$$

$$u(n_2) = \sqrt{(3.43\text{E} - 11^2) + (2.97\text{E} - 11^2)}$$

$$= 4.54\text{E-}11$$

The standard uncertainty for the calibration of the GC thermal detector is then calculated through the combination of the standard uncertainties of the molar composition of both components through the use of equation (C-9) as follows:

$$u_{\text{calib}}(y_1) = \sqrt{\left(\frac{\overline{y_2}}{\overline{n_1} + \overline{n_2}} . u(n_1)\right)^2 + \left(\frac{\overline{y_1}}{\overline{n_1} + \overline{n_2}} . u(n_2)\right)^2}$$

$$= \sqrt{\left(\frac{0.0005}{6.16\text{E} - 06 + 2.86\text{E} - 09} . 1.03E - 07\right)^2 + \left(\frac{0.99953}{6.16\text{E} - 06 + 2.86\text{E} - 09} . 2.86E - 09\right)^2}$$

$$= 1.11\text{E-}05$$

The combined expanded uncertainty for the vapour composition ($U_{(y_1)}$) also takes into account the repeatability of the samples in the vapour phase which is calculated as follows:

$$u_{rep}(y_1) = \frac{2.11E - 08}{\sqrt{8}}$$

$$= 7.45\text{E-}09$$

$$U_{(y_1)} = 2 \times \sqrt{U_{\text{calib}}{y_1}^2 + U_{\text{rep}}{y_1}^2}$$

$$= \sqrt{1.11\text{E} - 05^2 + 7.45\text{E} - 09^2}$$

$$= \underline{\mathbf{0.00002}}$$

The final uncertainty takes into account the coverage factor (K = 2)

The low values for the expanded uncertainty in the vapour phase can thus be attributed to the excessively larger amounts of carbon dioxide present in the phase when compared to the amounts of perfluorononane. This disparity (in moles) can be easily observed in Table C-1, in the vapour phase section. The uncertainties for all the data points measured for this system were computed through the use of an excel spread sheet and are tabulated in Table 7-21.